MOLYBDENUM CHLORIDE INCORPORATED SOL-GEL MATERIALS FOR OXYGEN SENSING ABOVE ROOM TEMPERATURE

By

D J Osborn III

A DISSERTATION

Submitted to
Michigan State University
in partial fulfillment of the requirements
for the degree of

Chemistry − Doctor of Philosophy

2014

ABSTRACT

MOLYBDENUM CHLORIDE INCORPORATED SOL-GEL MATERIALS FOR OXYGEN SENSING ABOVE ROOM TEMPERATURE

By

D J Osborn III

Maximizing the efficiency of the combustion process requires the ability to sense oxygen levels over a broad range of concentrations with fast response times under rapidly varying conditions of pressure and temperature to maintain the correct fuel/oxygen ratio in real-time. Quenching of the luminescence from organometallic compounds by oxygen has been used to develop a number of fiber-based sensors. A major drawback of these organometallic indicators for combustion applications is that the chromophores degrade with time, have a limited operational temperature range, typically room temperature ±25°C, and lack long-term reliability. This work investigates luminescent molybdenum clusters based on Mo_6Cl_{12} were as replacements for organometallic indicators. A study of the high temperature stability of Mo_6Cl_{12} in air revealed irreversible changes in the optical absorption spectrum at T >250°C and a loss of the red luminescence characteristic of the pristine clusters. Thermal aging experiments run in air and under nitrogen point to oxidation of the clusters as the cause of the change in optical properties. X-ray powder diffraction measurements on samples annealed at 300°C under controlled conditions are consistent with oxidation of Mo_6Cl_{12} to form MoO_3. Optical and thermal aging experiments show that $K_2Mo_6Cl_{14}•1H_2O$, the alkali metal salt of Mo_6Cl_{12}, has higher thermal stability and remains luminescent after long-term aging in air at 280°C. Methods were developed for

depositing $K_2Mo_6Cl_{14}$•$1H_2O$–incorporated sol–gel films on planar and optical fiber substrates by dip coating and spray coating. The mechanical properties of the films depended on the film thickness; thin films were stable, but cracks often formed in the thicker films needed for sensors. This problem was addressed using two strategies: altering the components of the sol–gel solutions used to embed the clusters and by devising a composite approach to sensing layers where a slurry of fully cured sol–gel particles containing $K_2Mo_6Cl_{14}$•$1H_2O$ in a sol–gel "binder" were deposited on substrates. The optical properties of a large number of fiber sensors were tested up to 102°C, with the best results obtained using the $K_2Mo_6Cl_{14}$•$1H_2O$/sol–gel composite sensing film. Fiber **M** demonstrated quenching of 4–6× between <0.001% and 21.1% (v/v) oxygen at 23, 42, 60, 81 and 102°C respectively. The sensor switches abruptly between two well defined levels with a response time of less than 10 s. Quenching of the cluster luminescence by oxygen obeys a two-site Stern–Volmer relationship based on measurements of fiber **121** at 42, 73, and 102°C, with sensitivity decreasing as temperature increases. The cycle-cycle variations for six cycles between nitrogen and oxygen at 58°C for fiber **45** corresponds to an uncertainty of ±1% to ±15% in oxygen concentration over the entire measurement range from 21.1% (v/v) to 2.1% (v/v) oxygen respectively. The long-term performance data from cycling fiber **70** between <0.001% (v/v) and 21.1% (v/v) oxygen for 14 hours was stable over the entire period and variations in sensor signal were found to be synchronous with the temperature fluctuations in the flow through cell. The magnitude of the sensor signal up to 102°C is ~3-nW for ~300 μW of incident excitation power. For the current 15-cm long fiber sensor, the autofluorescence (0.011 nW) is 40× smaller than the signal (~ 0.4 nW) in 20% (v/v) oxygen.

ACKNOWLEDGEMENTS

I would like to express my sincere gratitude to God. He continues to grant me courage and strength when I am weak. Like an anchor, He holds fast while I swing in various directions. If I learn nothing else from this experience, I am satisfied with having learned of the value of a relationship with God. The people He has put in my life have been patient as I struggle, guided me when I ask for help, and been compassionate when I try to do it my way and fail. I believe all people in my life have taught me something valuable, but the following people have had an incredible impact on my life: Momma- and Poppa-O, my brother Jason, my sister Nikki, my brother Kerry, Harvey Hoffman, Anne Howarth, Liz Hoogstra, Scott Achenbach, Mark and Jodie Breithart, Ken Fillwock, Fred Jernigan, Tim Pryer, Gary Underwood, Dennis Pulver, Mark Jean, Geoff Mowry, Dennis Southey, Mike Kowalske, John Levin, Karl and Sylvia Rundquist, Jamie Dunn and her family, John Kerr, Don Walters, Karl Mankie, Dale Brown, Don and Susan Kuchnicki, Mike and Mary Grimm, Larry and Paige McCormick, Leslea Burnett, Mike and Marte Drummheller, Pete and Corina Klein, Andrea Scannell, Mark Fales, Jim McClintock, Howard Anderson, Dick Divelbiss, Aaron Keefe, Matt Helm, Michael Wiltz, Jeb Burns, John Taylor, Tom Curtis, Chris Patton, Bill Truluck, Kevin Olsen, Mike Clark, Mike Mullins, Brian Archiply, Doug Schrems, Howie Dickeson, Chris Elms, Tom Hutt, Willy Murphy, Chef Jeff, Brian Burns, AJ O'Neil, Ben Burroughs, Bob Sheldon, Dave Giltner, Dave Morton, Derek Chandler, Dick Manikowski, Don Wellman, Greg Stack, Gideon Pfeffer, Jim Flemming, John Freeman, Mac Plachta, Matthew Kowalewski, Paul Flaviani, Rick Tripp, Rob McClean, Robi Mitra, Eddy Armbruster, Mike Barnes, Paola Piantoni, Payem and Sabrina, Byron and Elena Reyes, Brandon Gohsman, Mark Milutin, Scott King, and Pam Baker.

I thank Maria Alexandra Peralta-Sanchez for her unwavering love and support. She is a truly remarkable woman and I am blessed to have her in my life.

I thank Dr. Greg Baker and Dr. Gary Blanchard for the things they taught me outside the scope of their job and the time they spent just being friends when needed. Their sense of humor lifted my spirits and their actions showed me that humility, love, and tolerance lead to profound happiness. I also want to express my appreciation for all the help that Dr. Ruby Ghosh gave while working together on the sensor project. I thank my committee members, Dr. Babak Borhan, Dr. Jim McCusker, and Dr. Jetze Tepe for their support and understanding.

I thank the Baker group members – Fadi, Leslie, Feng, Xuwei, Bao, Ying, Qin, Ping, Sampa, Erin, Tom, Burpol, Gina, and Jon. I am especially grateful for the workout sessions with Jon in the evenings and the heart-to-heart talks with Erin in the morning before everyone arrived in the lab. I also want to thank the Blanchard group members for listening to my presentations and providing suggestions, help, and camaraderie. I would also like to thank Dr. Philip Squatritto, Dr. Dillip Mohanty, Dr. James Gano, Dr. Tim Mueser, Dr. Robert Flowers, Dr. Mark Mason, and Steve Moder for teaching me many of the lab skills I used here at MSU.

Finally, I would like to say thank you for the financial support provided by the Department of Energy (NETL grant DE-FC26-02NT41582), the Michigan State University Department of Chemistry, and Michigan State University Graduate School for a dissertation completion fellowship.

TABLE OF CONTENTS

LIST OF TABLES

LIST OF FIGURES

KEY TO ABBREVIATIONS

A	Absorbance, A.U.
ε	Molar extinction coefficient, L/mol·cm
b	Cuvette pathlength, cm
c	Concentration, mol/L
τ_0	Lifetime in the absence of quencher
ϕ	Quantum yield
K_{sv}	Stern-Volmer constant
I_0	Intensity in the absence of quencher
I	Intensity in the presence of quencher
λ	Wavelength, nm
θ	Angle, degrees
k_q	Quenching constant,
P	Pressure, atm
V	Volume, L
n	Number of moles, mol
R	Universal gas constant, 8.2057 x 10^{-2} L atm / mol·K
T	Temperature, K
psi	Pounds per square inch
sccm	Standard cubic centimeter
cps	Counts per second
PMT	Photomultiplier tube
TFP-tMOS	(3,3,3-trifluoropropyl)trimethoxysilane
PtMOS	*n*-trimethoxy(propyl)silane
OtMOS	trimethoxy(octyl)silane
TEOS	Tetraethylorthosilicate
TMOS	Tetramethylorthosilicate
FJ	Faread Jamalifard
MM	Maveric Method
mp	Mortar and Pestle
wlb	Wig-L-Bug

Chapter 1 – Introduction

There are many industrial applications that require gas sensors able to withstand high temperatures and chemically harsh environments. Examples include heat treating, metal processing and casting, glass, ceramic, pulp and paper, automotive, aerospace, utility and power, chemical and petrochemical, and food processing.[1] Efficient use of fossil and renewable fuels in combustion, coal gasification, and in industrial processing requires sensors to monitor the levels of gaseous oxygen at high temperatures. In combustion processes, real-time monitoring of oxygen levels provides the data necessary to calculate the fuel:oxygen ratio and maximize combustion efficiency. Improved efficiency is accomplished by altering the fuel:oxygen ratio to maximize the heat extracted from the fuel and minimize the emission of unwanted byproducts (pollutants). The goal of this research is to alter the design of our previous room temperature oxygen sensor[2] so that it can be used to monitor oxygen partial pressure at high temperatures. The performance of the resulting sensor will then be tested over a broad temperature range for its ability to measure different concentrations of oxygen rapidly and to provide reliable performance at high temperatures for extended periods of time.

1.1 CURRENT OXYGEN SENSOR TECHNOLOGIES

There are four major methods for determining oxygen concentration[3]; Winkler titration,[4] electroanalytical,[5] pressure-based, and optical-based. Optical-based methods are further subdivided into direct and indirect methods.[3] For high temperature applications such as

combustion, the electrochemical cell is the prevailing choice[3] and currently there has been only one optical fiber sensor capable of measuring oxygen at combustion temperatures.[6] There are advantages and disadvantages to each type of sensing platform and a brief overview is given in the following two sections.

1.1.1 Electrochemical

There are several electrochemical cells used for measuring oxygen at high temperatures, but the yttria-stabilized zirconia (YSZ) cell dominates the market. While these ceramic sensors withstand high temperatures, are relatively inexpensive to fabricate, accurate, and small, they suffer from a number of limitations. First, they do not operate below 300°C and therefore the oxygen/fuel ratio is not optimized until the sensor heats up. Second, they have slow response times, limiting their use in maximizing the efficiency of combustion. Third, they are susceptible to electrical interference. Fourth, they consume oxygen and can lead to erroneous results. Lastly, they have a limited operating lifespan – typically on the order of two years.

1.1.2 Optical

Fiber optic oxygen probes are well-suited for development as micro-sensors for oxygen levels in power plant exhaust. Advantages of fiber sensors include the ability to probe otherwise inaccessible locations via miniaturization into small flexible probes and immunity from electrical interference. Single sensors can be placed in an array rake in the exhaust duct downstream of a combustion chamber to provide spatially localized information. The response time of fiber

sensors can be less than one second which would allow for real time control and balancing of the individual combustor operation, improve efficiency, and lower emissions.

Optical fibers are typically prepared from fused silica that is doped with an inorganic oxide such as GeO_2 to define the high index core of the fiber. Most fibers are clad with low refractive index polymeric materials that help confine the light to the fiber and protect the fiber from damage. Being organic polymers, these claddings are not compatible with high temperatures and degrade well below 500°C. In high temperature fibers, the organic cladding is replaced by an inorganic material. Such fibers are available commercially with stated use temperatures of 750°C,[7] and there is precedent for their use in oxygen detection at 500°C.[8] The fiber cladding is gold (melting point ~1000°C) which, because of its chemical inertness and thermal stability, makes it well suited to high temperature sensing in aggressive environments.

The principal goal of this project was to expand the range of operation of a room temperature fiber optic oxygen sensor to the high temperatures encountered in combustion exhausts. The primary materials challenges were the design and synthesis of a suitable matrix for sensing under high temperature conditions, and the characterization of the optical response of clusters at high temperatures.

1.2 LUMINESCENT OXYGEN PROBES

1.2.1 Organic oxygen probes

Perylenes, substituted perylenes, pyrene, substituted pyrenes, and many other polycyclic aromatic hydrocarbons have been used as oxygen probes,[9-11] but lack the chemical and thermal stability required for long-term high-temperature oxygen sensing.

1.2.2 Organometallic oxygen probes

Oxygen quenching of the fluorescence from organometallic compounds has been used to develop a number of fiber sensors. Ruthenium,[12-20] platinum,[12-20] palladium,[12-20] rhenium,[21-26] osmium,[14, 21, 27-31] iridium,[3, 19, 21, 27, 32-48] and copper[6, 8] transition metal complexes have been used as luminescent probes for oxygen measurements. Aa major drawback of these indicators for any industrial application is that the chromophores degrade with time, i. e. lack long term stability and reliability. Also, organometallic-based sensors have a limited operating temperature range, typically room temperature ±25°C.

1.2.3 Oxygen sensing via Mo_6Cl_{12} clusters

The use of Mo_6Cl_{12} clusters offers particular advantages for the construction of practical fiber optic devices. Synthesis of the clusters is accomplished using inexpensive starting materials and their synthesis is relatively straight forward. The long lifetime of the cluster excited state (>100 μs) and the large Stokes-shift of the emission (>300 nm) allows the use of a simple light emitting diode (LED) for excitation and a Si photodiode for detection, both of which are essential for fabrication of the sensor in volume. Other advantages of the metal halide clusters are that they

can withstand repeated thermal and O_2 cycling and show no signs of photochemical decomposition. Finally, the red luminescence emitted from the excited state of the Mo cluster is quenched efficiently only by ground state $^3O_2$. Since the ground state of all other gases typically present in power plant exhausts such as hydrogen, hydrocarbons, carbon monoxide, nitrogen oxides, and sulfur oxides do not have a triplet ground state, no cross-sensitivity with these species is expected.

The photophysics and physical properties of Mo_6Cl_{12} are well suited for oxygen sensing schemes.[49] The extended cluster array (**Figure 1.1**) has a quasi-perovskite structure, composed of an octahedral core of molybdenum atoms with eight face bridging chlorides and four axial chlorides, which are shared among neighboring cluster subunits.[50]

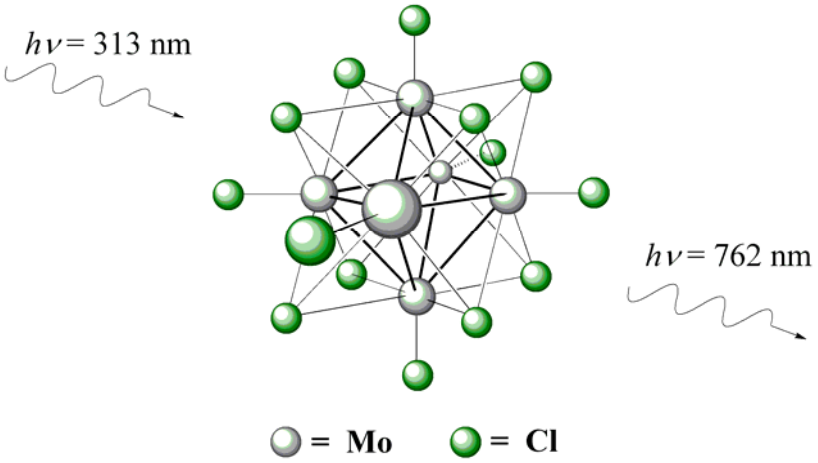

Figure 1.1. The Mo_6Cl_{12} cluster, the basis for an optical oxygen sensor.

The emissive excited state is localized in the metallic core of the cluster with little ligand character[51]. From a sensor perspective, this cluster is an ideal oxygen probe because its luminescence is largely unaffected by the manner in which it is confined, whether that be encapsulation in a sol–gel matrix or immersion in liquids. When dissolved in solution the clusters exist in the form $[Mo_6Cl_8]Cl_4L_2$ where L is either a solvent molecule or another ligand. Since Mo_6Cl_{12} is synthesized at 450°C,[50] the molybdenum clusters are intrinsically stable at high temperatures and should be ideal luminescent probes for high temperature oxygen sensing. There are a number of chemical variations on the basic Mo_6Cl_{12} cluster. In each derivative, the Mo_6Cl_8 core of the cluster core is conserved while the remaining chlorine atoms can be exchanged with other ligands to alter the solubility of the cluster and potentially the chemical compatibility of the cluster with the matrix. Being able to dissolve the clusters in a wide range of polar solvents provides flexibility in the preparation of clusters immobilized in matrices. As noted earlier, the photophysics of the cluster is largely insensitive to the nature of the ligands attached to the cluster, and thus changing the ligands to achieve improved solubility or some other property has few ramifications for the optical properties of the cluster.

From an oxygen sensing perspective, the use of these Mo_6Cl_{12} clusters is unique. First, when excited with UV light, the clusters emit with high efficiency in the red, with the emission quenched by oxygen. Second, the Stokes shift is several hundred nm (**Figure 1.2**), enabling the use of a fiber probe based on a simple optical design. The clusters are soluble in a wide range of solvents, and their optical properties are insensitive to solvent molecules. Finally the clusters

themselves are synthesized at high temperatures, and thus they are thermally robust. These properties suggest that high temperature oxygen sensors could be realized by immobilizing the clusters in a suitable matrix at the tip of a fiber optic probe. There are three components that make up the fiber optic probe; the fiber, the molybdenum clusters, and the support. All three must be stable in the thermally and chemically aggressive environment of the exhaust from a power plant.

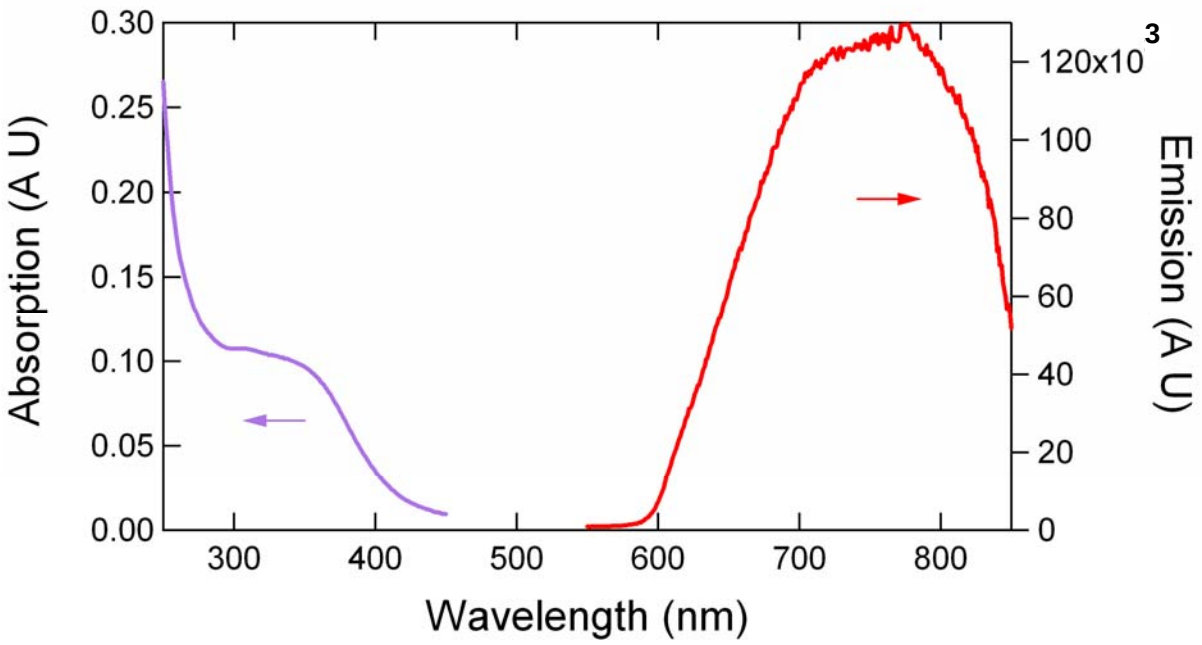

Figure 1.2. Absorption and emission spectra of Mo_6Cl_{12} in acetonitrile showing the large Stokes shift that allows for simple LED excitation and photodiode detection. The data was obtained by the author in collaboration with R. N. Ghosh.

1.3 MATRICES

1.3.1 Polymer matrices

Previously, we developed a room temperature fiber optic oxygen sensor that utilizes the luminescence from hexanuclear metal halide clusters such as Mo_6Cl_{12}[2] (see **Figure 1.1**) to detect oxygen in the 0.1% (v/v) to 20% (v/v) range. Though the organic polymers used to

fabricate the device limited its operation to temperatures <200°C, we proposed to extend our previous results to 600°C by replacing its organic components with inorganic materials that have superior thermal stability.

There are several key design features in our first generation fiber optic oxygen sensor. First, the Mo_6Cl_{12} was immobilized at the end of a fiber in a thin film of poly[1-trimethylsilyl-1-propyne] (PTMSP) a synthetic polymer that has the highest gas permeability coefficient of any known polymer.[52] The measured permeability for a 100 μm film implies an oxygen diffusion constant of 10^{-4} cm^2/s or a diffusion time of 1 s. Second, when the hexanuclear Mo halide clusters are embedded in the polymer, there is no discernable shift in the absorption or emission bands, since the photophysics of interest is due to electronic transitions confined to the $[Mo_6Cl_8]^{4+}$ cluster core.[53] Thus, the performance of the sensor is unaffected by extraneous solvents or gasses that may be in the vicinity of the fiber tip.

Plotted in **Figure 1.3** is output signal from the sensor in nW as a function of oxygen concentration from 0–20% (v/v) oxygen, with nitrogen as the balance gas. Note from the error bars on the measured points, within our 6 Hz measurement bandwidth the standard deviation is less than 2% of the signal. The data demonstrate that the sensor can clearly resolve changes of 0.1% (v/v) oxygen concentration in the 0–1% (v/v) range, changes of 0.5% (v/v) oxygen concentration in the 1–4% (v/v) range, changes of 1% (v/v) oxygen concentration in the 4–10%

(v/v) range, and changes of 2% (v/v) oxygen concentration in the 10–20% (v/v) range. It was also demonstrated that the quenching of the cluster luminescence shown in **Figure 1.2**, obeys the Stern–Volmer equation[2] as expected from theory.

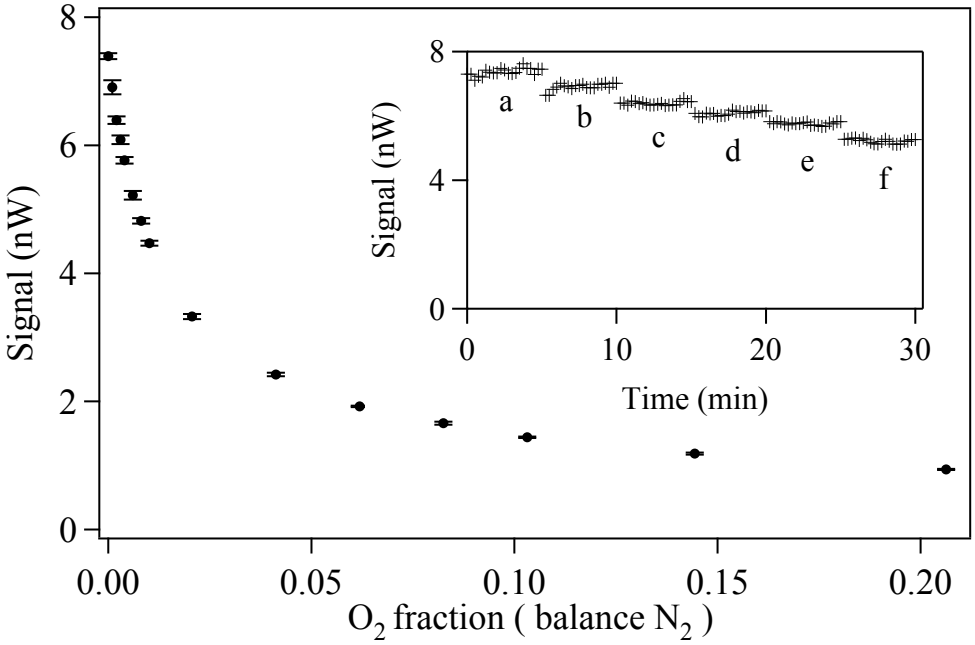

Figure 1.3. Output signal from the reflection mode oxygen fiber sensor using PTMSP as the porous matrix.[2] Inset: signal as a function of time for a) 0% (v/v), b) 0.10% (v/v), c) 0.20% (v/v), d) 0.30% (v/v), e) 0.40% (v/v) and f) 0.61% (v/v) O_2, balance gas is N_2.

From the inset to **Figure 1.3** we deduce that an upper bound to the sensor switching time is 30 s. This is not the intrinsic response time of the sensor, which we estimate to be 1 s. The sensitivity and time response of our oxygen sensor is thus well suited for both emission control and individual burner balancing in power plant environments. The simple sensor design translated into a simple construction process. Attaching the sensing layer to the end of the fiber optic involved cleaning the tip in a uv/ozone generator to remove residual organic compounds and

ensure good wetting of the surface. Subsequent dip-coating of the end of the fiber with a tetrahydrofuran solution of PTMSP and the clusters formed a bead of polymer and clusters at the tip of the probe.

1.3.2 Sol–gel matrices

In the previous optical fiber sensor,[2] Mo clusters were immobilized in poly[1-trimethylsilyl-1-propyne] (PTMSP). For sensing O_2 in combustion processes, the principal challenges are to maintain a high permeability and to overcome the intrinsically poor thermal stability of synthetic polymers, which generally degrade to volatile products below 400°C.

A high temperature matrix for immobilizing molybdenum clusters must satisfy several physical properties. First, the matrix needs to have a high gas permeability to enable reasonable response times for the sensor. Second, the matrix must be compatible with the molybdenum clusters in terms of the synthesis of the composite, show no optical interference with the matrix or the cluster, and be chemically inert toward the molybdenum clusters embedded in the matrix. Matrix stability at high temperatures is critical. Soot and other carbonaceous species may potentially foul the sensor, and a practical sensor requires a method for removing accumulated carbon. Either operating the sensor at temperatures >400°C or infrequent heating to higher temperatures in air may be required to clear the carbon from the sensor. Inorganic materials such as SiO_2 are logical replacements for PTMSP as the matrix, since they have excellent thermal stability and can be synthesized as thin films that adhere well to glass fibers.[54-56] In addition,

the high gas permeability of PTMSP, a property derived from the large free volume of the polymer, can be duplicated through controlled syntheses of SiO_2. Porous SiO_2 is generally synthesized by a sol–gel process.[54-57] As shown in **Figure 1.4**, the condensation of tetraethyl orthosilicate and similar organometallic compounds at room temperature leads to a disordered 3-dimensional network of Si-O-Si bonds with embedded solvent and unreacted alkoxy groups. Their removal with solvent or by heating the sample to >500°C to decompose the organic compounds (calcination), yields a highly porous matrix.

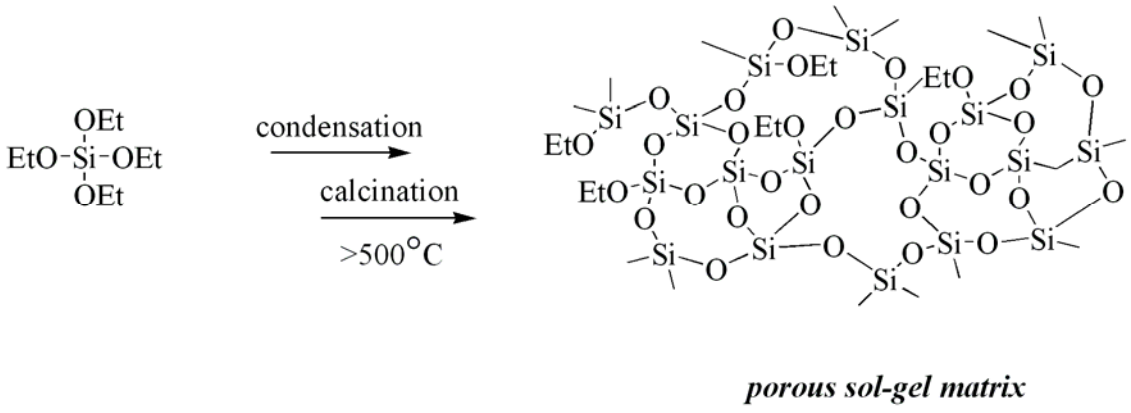

Figure 1.4. Condensation of triethyl orthosilicate to give a porous sol–gel matrix. Calcination in air removes residual organic fragments.

Further control over the porosity and pore size of SiO_2 is through the use of templating schemes for the preparation of mesoporous silicas.[57-59] MCM-41 is the most noted member of this family of materials and was the first to be prepared.[60, 61] The templating approach, shown in **Figure 1.5**, is based on the premise that organic molecules, and especially surfactants that self assemble into comparatively large domains, can be used as a temporary scaffold for the construction of a silica shell around the template. The scaffold can then be removed via solvent

extraction or by calcining the intermediate product to remove the organic template. Thus, the resulting pore structure in the template-free oxide reflects the size and geometry of the initial scaffold. A variety of organic molecules can be used as templates, and the porosity of the mesoporous silicas can be controlled by the choice of the templating molecule. Typically, these structures are sufficiently robust to be calcined at >500°C in air.[62]

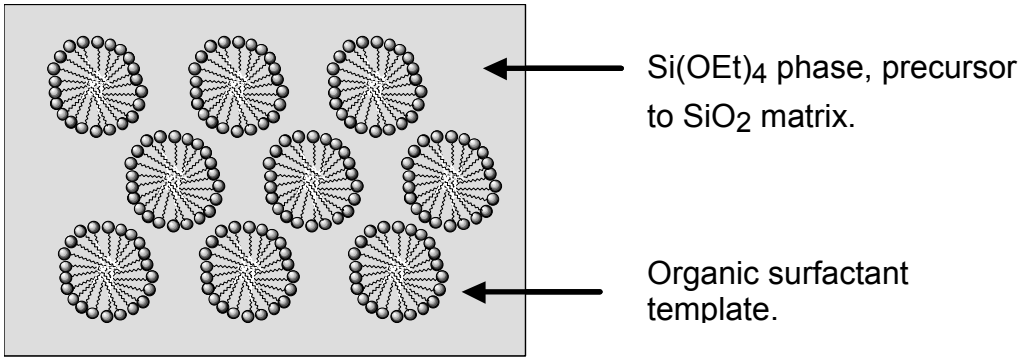

Figure 1.5. Template approach to mesoporous silica.

1.3.3 Immobilization of molybdenum clusters.

A wide variety of molecules for catalysts and sensing have been immobilized in SiO_2 matrices. Two general approaches have been used. In the first, the molecule is a spectator during the sol–gel synthesis and is trapped in the sol–gel film. Relatively large molecules have been entrained in sol–gel matrices and due to their large size relative to the pores, they cannot leach from the matrix.[58] Clusters embedded in matrices with relatively small pore sizes may show diffusion dependent responses to O_2 and could be susceptible to fouling. A simple solution to this problem is to use the templating route to obtain mesoporous silicas with large pore sizes.

A second scheme is to prepare a porous matrix first, then use solvent to infuse the matrix with the desired molecule. Calcining to remove organic species immobilizes the molecule within the matrix. The infusion scheme is attractive since it places clusters only in sites that are accessed easily by gasses, and the number of clusters loaded into the matrix can be changed relatively easily. In addition, the post-synthesis introduction of clusters into the matrix enables rapid screening of clusters with different structures. Post-synthesis loading of the matrix requires that the pore size of the silica be large enough to allow incorporation of clusters. In cases where the porosity of the matrix is too low for efficient introduction of the cluster, or the permeability is less than desired, we will again use the templating scheme to build in the desired pore size

1.3.4 Integrating optical fibers with sol–gel matrices.

Having well-defined routes to porous matrices and methods for immobilizing clusters in the matrix, the remaining materials challenge is to attach sol–gel matrices containing molybdenum clusters at the tip of the optical fiber. Unlike the PTMSP matrix, where the hydrophobic polymer was a mismatch for the hydrophilic fiber optic tip, the deposition of sol–gel films on glass and silica substrates is fairly straightforward. There are many examples of immobilizing sensing molecules on a fiber via the sol–gel technique.[63] Most of these sensors are based on an evanescent wave geometry,[64, 65] where the cladding of the fiber is replaced by a sol–gel matrix and the sensing is based on an evanescent wave in the fiber sampling the surface-bound sol–gel matrix. Attaching the matrix to the tip of a fiber (reflection mode design) is less common because of the smaller active region available for detection of the analyte. However, the same chemistry is used for both cases and it typically involves the reaction of surface bound silanol

groups with the tetraethyl orthosilicate or a similar compound. Two important steps in adding a sol–gel film to a glass substrate are proper preparation of the fiber surface to remove organic contaminants that might lead to non-wetting of the surface, and the preparation of surfaces that are terminated with silanol groups. The latter step is usually accomplished by treatment with HF.

1.3.5 Matrices for immobilizing clusters.

The previous sections broadly outlined approaches to porous oxide matrices suitable for immobilizing Mo_6Cl_{12} clusters. Initially, our focus will be the preparation of thin films on planar quartz substrates using a sol–gel process. Working with planar surfaces allows for the development of proper reaction conditions for preparing and characterizing films with encapsulated clusters, and once generic conditions have been established for flat surfaces, they can be transferred to optical fibers. The transition to fibers should be relatively easy since the surface chemistry is essentially identical for both cases. The initial matrices will be based on the controlled hydrolysis of tetraethylorthosilicate, since the preparation of such films is well known, and the porosity of the films can be manipulated through choice of the reaction conditions. The polarity of this system matches nicely with the solubility of Mo_6Cl_{12} clusters, allowing for relatively easy incorporation of the clusters into the sol–gel film. Planar substrates will serve as our synthetic test bed, since they allow facile testing of the film's adhesion to substrates. In addition, characterization of the concentration and distribution of clusters on flat substrates is relatively easy using optical microscopy.

Films on planar substrates are also convenient for studying potential sintering (densification) processes. During sintering, the high surface area of sol–gel matrices declines as nanopores coalesce to give micropores. Although BET isotherms show that the sintered sol–gel materials retain a high surface area and presumably a correspondingly high permeability, sintering may make some clusters inaccessible to oxygen and contribute to poor sensor sensitivity. Simple experiments can test for deleterious densification and provide estimates for sensor lifetimes. Thin sol–gel films containing Mo_6Cl_{12} will be deposited on fused silica substrates and then annealed in a furnace at ~500°C. After desired annealing times, the samples will be removed from the furnace and their luminescence characterized in an argon atmosphere at room temperature. Tracking changes in luminescence as a function of annealing conditions will enable early detection of and solutions to sintering problems.

If sintering does degrade the luminescent properties of the films, this problem can be overcome by incorporating fumed silica in sol–gel films. Fumed silica is a relatively dense form of SiO_2 that is formed by a flame hydrolysis process. The primary fumed silica particles are small (nm) with surfaces terminated in silanol groups (SiOH). Fumed silica is used widely as low cost filler for polymers and to modify the viscosity of oils and other liquids. When used as a component in sol–gel process, the fumed silica rigidifies the matrix and minimizes densification at high temperatures. Porous silica matrices are likely to have limited stability above 600°C. New matrix materials, such as zeolites, will be evaluated to extend the sensor to temperatures >600°C. Once the conditions for the preparation of stable Mo_6Cl_{12}-containg matrices are established, we will switch to deposition of the matrices on fiber optic tips. The deposition

technique is quite simple. The fiber tips will be cleaned with a UV/ozone cleaner followed by an acid etching step to ensure a silanol terminated surface. Dip coating the fiber into the sol gel solution, curing, and heating to remove residual organic fragments will yield the porous matrix.

1.3.6 Optical characterization of matrices.

The luminescent properties of Mo_6Cl_{12} at high temperatures are critical information that must be acquired early in the research program. There are no data on the luminescence of Mo_6Cl_{12} or related clusters at high temperatures, but the insensitivity of the core to changes in solvent,[66] and extrapolations from lower temperature data both suggest that the luminescence seen at room temperature is retained at high temperatures. The temperature dependence of the cluster luminescence has been investigated from room temperature to liquid helium temperature.[51, 67] Based on the room temperature fiber optic sensor,[2] it was estimated that the reduction in the signal intensity at 600°C would be a factor of ten at most. This would result in a 1 nW signal, a level easily detectable within our signal to noise ratio.

The initial measurements will use bulk samples of Mo_6Cl_{12} powder, which will later be validated by measurements on Mo_6Cl_{12} containing sol–gel films on planar substrates. Careful measurements of the luminescence as a function of temperature are needed to provide a baseline that will allow us to discern intrinsic temperature dependent changes in luminescence from those caused by the immobilization process. The luminescence of thin films on planar substrates can be characterized in an argon atmosphere, in the absence of quenchers, and in air. Construction of

a heated sample chamber will allow us to extend the room temperature measurements of the clusters in solid form and cluster/sol–gel composites to temperatures as high as 600°C. Measurements of the line shape and total integrated signal intensity will reveal if there are any adverse effects on the cluster photophysics due to time/temperature/gas cycling. These are important parameters for designing a stable and reliable fiber sensor.

1.3.7 Optical fiber parameters.

As noted earlier, appropriate fibers are available for high temperature use. Remillard[6] and co-workers at Ford demonstrated a fiber optic probe for automotive exhaust applications. Their sensor uses a copper-exchanged zeolite indicator to measure the equivalence ratio for gas mixtures containing strong reductants at 500°C. Gold coated silica optical fiber that can withstand continuous operation at 700°C and are not attacked by most acid, bases or solvents are available commercially.[7] These fibers meet the required optical specifications for fiber sensor operation including ultra-violet and visible transmission and a large numerical aperture.

The reflection mode fiber sensors will be fabricated by dip coating the cluster/sol–gel composite on the cleaved end of a multimode mode fiber. The large core diameter (~500 μm) and high numerical aperture (~0.3) will allow for efficient excitation and collection of the luminescence from the clusters immobilized at the back face of the fiber. Initial use of polymer clad fiber[68] for measurements from room temperature to 50°C will allow us to verify our previous results[2]

using a polymer based immobilization scheme. High temperature fiber sensors can then be fabricated on gold coated fibers[7] that can withstand temperatures up to 700°C.

1.3.8 Fiber sensor characterization.

Fiber sensor performance will be evaluated using a setup similar to the one in **Figure 1.6**.

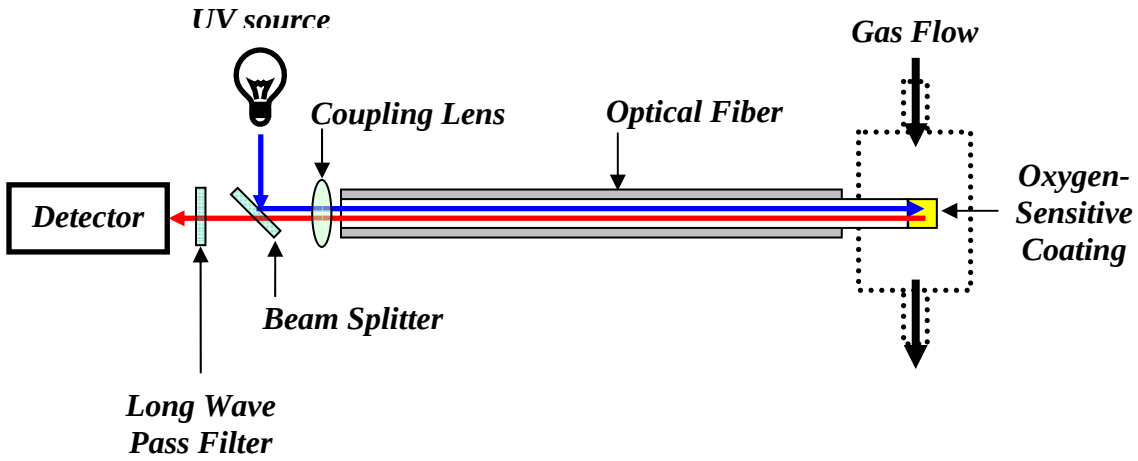

Figure 1.6. Schematic of the reflection mode fiber sensor. Adapted from a figure prepared by R. N. Ghosh.

The broad absorption band of the clusters, which extends from 300 nm to 400 nm, allows for the use of a number of compact UV excitation sources. These include small Hg lamps, which have a peak emission at 313 nm, and near UV solid state light emitting diodes.[69] The tradeoffs between the various sources are total emitting power, coupling efficiency into the fiber, source lifetime and cost. The large Stokes shift of the clusters (>300 nm) will allow us to use simple filtering techniques to separate the excitation and emission. Due to the long lifetime (>100 μs) and large Stokes shift of the cluster, the luminescence is easily detectable by integrating over the broad emission band. Based on previous results[2] we anticipate having enough signal to noise

ratio to perform all our measurements in the frequency domain, without the need for time resolved measurements. A Si photodiode will be used as the detector. The simplicity of the optics, use of a compact UV source and Si photodetector are essential for volume fabrication of the sensor.

The advantage of the reflection mode geometry is that the optical excitation and detection system can be located in a well-controlled environment away from the far end of the fiber where the sensing takes place. The small fiber probe size also allows for spatially resolved measurements at the micron scale. The sensor is exposed to a controlled environment with varying oxygen concentrations by enclosing the last few centimeters of the fiber in a flow-though cell.

A heated sample cell can be constructed to extend the fiber sensor test system shown in **Figure 1.6** to higher temperatures to characterize the sensors at high temperature (up to 600°C) in chemically reactive environments. By using a compact sample cell, which is fed by a two-port oscillating shutter, the gas in the sample cell can be exchanged at a rate of at least 1 Hz. In addition, the hardware and software necessary to electronically control the gas composition while recording the sensor output signal will be developed. The gas mixing system will allow for three different species, oxygen, nitrogen and nitrogen oxides.

1.3.9 Issues of field deployment.

As discussed previously the luminescence from the cluster excited state is quenched only by the presence of a gaseous species with a spin triplet ground state. Of all the gases typically found in power plant exhausts, the nitrogen oxides (NO_x) are identified as the single potential source of

cross sensitivity. This potential cross sensitivity to NO_x can be investigated via luminescence spectra of cluster/sol–gel composite films. Potential fouling by carbon residues can also be investigated by comparing the fiber sensor properties before and after immersion in a high temperature fly ash ambient.

1.3.10 Expansion of the scope of the project.

Successful demonstration of the fiber sensor would allow us to determine how accurately the average oxygen concentration across the flow duct can be determined from a single sensor on the wall, i. e. address the "sampling" problem. Potential device configurations include a sensor array rake inside the flow duct or an array on the wall. Dynamic information on oxygen concentrations in the exhaust stream will allow better real-time control and balancing of individual combustor operation.

1.3.11 Summary of work.

In Chapter 2, the synthesis and characterization of molybdenum clusters that are stable and quenched efficiently at high temperatures is described. In Chapter 3, the development of a cluster-incorporated sol-gel matrixes and coating methods used to fabricate optical-fiber sensors are discussed. In Chapter 4, several optical fiber sensors are fabricated and charaterized in terms of mechanical stability, sensitivity, and repeatability at temperatures ranging from room temperature to >100°C. Taken collectively, the work described in this dissertation details a sustained and successful effort in the creation of a high-temperature oxygen sensor, with its primary limitations being related to the stability of the cluster at temperatures in excess of 250°C.

REFERENCES

REFERENCES

[1] S. Akbar, P. Dutta, C. H. Lee, *International Journal of Applied Ceramic Technology* **2006**, *3*, 302.

[2] R. N. Ghosh, G. L. Baker, C. Ruud, D. G. Nocera, *Applied Physics Letters* **1999**, *75*, 2885.

[3] X. D. Wang, O. S. Wolfbeis, *Chemical Society Reviews* **2014**, *43*, 3666.

[4] L. W. Winkler, *Berichte der Deutschen Chemischen Gesellschaft B* **1888**, *21*, 2843.

[5] K. Kinoshita, *Electrochemical Oxygen Technology*, Wiley-Interscience, **1992**.

[6] J. T. Remillard, J. R. Jones, B. D. Poindexter, C. K. Narula, W. H. Weber, *Applied Optics* **1999**, *38*, 5306.

[7] Fiberguide, in *Fiberguide Specification sheet for Superguide G ultraviolet-visible fiber with gold jacket*, Fiberguide Industries, Stirling, NJ.

[8] J. T. Remillard, B. D. Poindexter, W. H. Weber, *Applied Optics* **1997**, *36*, 3699.

[9] O. S. Wolfbeis, in *Optical Fiber Sensors, Vol. IV* (Eds.: B. Culshaw, J. Dakin), Artech House Publishers, Boston-London, **1997**, 53.

[10] Y. Amao, *Microchimica Acta* **2003**, *143*, 1.

[11] M. Quaranta, S. M. Borisov, I. Klimant, *Bioanalytical Reviews* **2012**, *4*, 115.

[12] A. Juris, V. Balzani, F. Barigelletti, S. Campagna, P. Belser, A. Vonzelewsky, *Coordination Chemistry Reviews* **1988**, *84*, 85.

[13] V. Balzani, F. Barigelletti, L. Decola, *Topics in Current Chemistry* **1990**, *158*, 31.

[14] J. N. Demas, B. A. DeGraff, *Coordination Chemistry Reviews* **2001**, *211*, 317.

[15] K. A. Hartzell, K. L. Danowski, P. Pantano, *Applied Spectroscopy Reviews* **2008**, *43*, 1.

[16] O. S. Wolfbels, *Analytical Chemistry* **2008**, *80*, 4269.

[17] X. D. Wang, H. X. Chen, Y. Zhao, X. Chen, X. R. Wang, *Trac-Trends in Analytical Chemistry* **2010**, *29*, 319.

[18] H. Lam, G. Rao, J. Loureiro, L. Tolosa, *Talanta* **2011**, *84*, 65.

[19] A. Ruggi, F. W. B. van Leeuwen, A. H. Velders, *Coordination Chemistry Reviews* **2011**, *255*, 2542.

[20] Y. Feng, J. H. Cheng, L. Zhou, X. G. Zhou, H. F. Xiang, *Analyst* **2012**, *137*, 4885.

[21] J. N. Demas, B. A. DeGraff, *Journal of Chemical Education* **1997**, *74*, 690.

[22] K. A. Kneas, W. Y. Xu, J. N. Demas, B. A. DeGraff, A. P. Zipp, *Journal of Fluorescence* **1998**, *8*, 295.

[23] C. A. Bignozzi, V. Ferri, M. Scoponi, *Macromolecular Chemistry and Physics* **2003**, *204*, 1851.

[24] L. Huynh, Z. U. Wang, J. Yang, V. Stoeva, A. Lough, I. Manners, M. A. Winnik, *Chemistry of Materials* **2005**, *17*, 4765.

[25] C. E. Wang, *Journal of Luminescence* **2014**, *145*, 531.

[26] G. Y. Xu, M. Lu, C. Huang, Y. Q. Wang, S. P. Ge, *Spectrochimica Acta Part a-Molecular and Biomolecular Spectroscopy* **2014**, *123*, 369.

[27] B. Carlson, B. E. Eichinger, W. Kaminsky, G. D. Phelan, *Sensors and Actuators B-Chemical* **2010**, *145*, 278.

[28] S. B. Bambot, G. Rao, M. Romauld, G. M. Carter, J. Sipior, E. Terpetchnig, J. R. Lakowicz, *Biosensors & Bioelectronics* **1995**, *10*, 643.

[29] W. Y. Xu, K. A. Kneas, J. N. Demas, B. A. DeGraff, *Analytical Chemistry* **1996**, *68*, 2605.

[30] K. F. Mongey, J. G. Vos, B. D. MacCraith, C. M. McDonagh, C. Coates, J. J. McGarvey, *Journal of Materials Chemistry* **1997**, *7*, 1473.

[31] E. J. McLaurin, A. B. Greytak, M. G. Bawendi, D. G. Nocera, *Journal of the American Chemical Society* **2009**, *131*, 12994.

[32] B. B. H. Leavens, C. O. Trindle, M. Sabat, Z. Altun, J. N. Demas, B. A. DeGraff, *Journal of Fluorescence* **2012**, *22*, 163.

[33] J. Estella, D. Wencel, J. P. Moore, M. Sourdaine, C. McDonagh, *Analytica Chimica Acta* **2010**, *666*, 83.

[34] L. H. Fischer, S. M. Borisov, M. Schaeferling, I. Klimant, O. S. Wolfbeis, *Analyst* **2010**, *135*, 1224.

[35] Y. H. Guo, Q. B. Mei, F. Yan, L. X. Wang, J. N. Weng, B. Zhang, W. Huang, *Acta Physico-Chimica Sinica* **2012**, *28*, 739.

[36] M. L. Ho, Y. A. Chen, T. C. Chen, P. J. Chang, Y. P. Yu, K. Y. Cheng, C. H. Shih, G. H. Lee, H. S. Sheu, *Dalton Transactions* **2012**, *41*, 2592.

[37] M. L. Ho, J. C. Wang, T. Y. Wang, C. Y. Lin, J. F. Zhu, Y. A. Chen, T. C. Chen, *Sensors and Actuators B-Chemical* **2014**, *190*, 479.

[38] K. Koren, S. M. Borisov, R. Saf, I. Klimant, *European Journal of Inorganic Chemistry* **2011**, 1531.

[39] Y. Xiong, Z. B. Ye, J. Xu, Y. Q. Zhu, C. Chen, Y. F. Guan, *Analyst* **2013**, *138*, 1819.

[40] G. DiMarco, M. Lanza, M. Pieruccini, S. Campagna, *Advanced Materials* **1996**, *8*, 576.

[41] G. Di Marco, M. Lanza, A. Mamo, I. Stefio, C. Di Pietro, G. Romeo, S. Campagna, *Analytical Chemistry* **1998**, *70*, 5019.

[42] Y. Amao, Y. Ishikawa, I. Okura, *Analytica Chimica Acta* **2001**, *445*, 177.

[43] M. C. DeRosa, P. J. Mosher, G. P. A. Yap, K. S. Focsaneanu, R. J. Crutchley, C. E. B. Evans, *Inorganic Chemistry* **2003**, *42*, 4864.

[44] M. C. DeRosa, D. J. Hodgson, G. D. Enright, B. Dawson, C. E. B. Evans, R. J. Crutchley, *Journal of the American Chemical Society* **2004**, *126*, 7619.

[45] M. E. Kose, R. J. Crutchley, M. C. DeRosa, N. Ananthakrishnan, J. R. Reynolds, K. S. Schanze, *Langmuir* **2005**, *21*, 8255.

[46] F. Lafolet, S. Welter, Z. Popovic, L. De Cola, *Journal of Materials Chemistry* **2005**, *15*, 2820.

[47] S. M. Borisov, I. Klimant, *Analytical Chemistry* **2007**, *79*, 7501.

[48] S. M. Borisov, I. Klimant, *Microchimica Acta* **2009**, *164*, 7.

[49] N. Prokopuk, D. F. Shriver, in *Advances in Inorganic Chemistry, Vol. 46*, **1999**, 1.

[50] H. Schaefer, H. G. v. Schnering, J. Tillack, F. Kuhnen, H. Worle, H. Z. Baumann, *Zeitschrift fur Anorganische und Allgemeine Chemie* **1967**, *353*, 281.

[51] T. C. Zietlow, M. D. Hopkins, H. B. Gray, *Journal of Solid State Chemistry* **1985**, *57*, 112.

[52] T. Masuda, E. Isobe, T. Higashimura, K. Takada, *Journal of the American Chemical Society* **1983**, *105*, 7473.

[53] J. A. Jackson, M. D. Newsham, C. Worsham, D. G. Nocera, *Chemistry of Materials* **1996**, *8*, 558.

[54] C. J. Brinker, G. W. Scherer, *Sol–gel science: the physics and chemistry of sol–gel processing*, 1st ed., Academic Press, Inc., San Diego, **1990**.

[55] C. A. Browne, D. H. Tarrant, M. S. Olteanu, J. W. Mullens, E. L. Chronister, *Analytical Chemistry* **1996**, *68*, 2289.

[56] S. A. Grant, J. H. Satcher, K. Bettencourt, *Sensors and Actuators B-Chemical* **2000**, *69*, 132.

[57] T. J. Barton, L. M. Bull, W. G. Klemperer, D. A. Loy, B. McEnaney, M. Misono, P. A. Monson, G. Pez, G. W. Scherer, J. C. Vartuli, O. M. Yaghi, *Chemistry of Materials* **1999**, *11*, 2633.

[58] K. Moller, T. Bein, *Chemistry of Materials* **1998**, *10*, 2950.

[59] A. Stein, B. J. Melde, R. C. Schroden, *Advanced Materials* **2000**, *12*, 1403.

[60] J. S. Beck, J. C. Vartuli, W. J. Roth, M. E. Leonowicz, C. T. Kresge, K. D. Schmitt, C. T. W. Chu, D. H. Olson, E. W. Sheppard, S. B. McCullen, J. B. Higgins, J. L. Schlenker, *Journal of the American Chemical Society* **1992**, *114*, 10834.

[61] C. T. Kresge, M. E. Leonowicz, W. J. Roth, J. C. Vartuli, J. S. Beck, *Nature* **1992**, *359*, 710.

[62] Z. H. Luan, E. M. Maes, P. A. W. van der Heide, D. Y. Zhao, R. S. Czernuszewicz, L. Kevan, *Chemistry of Materials* **1999**, *11*, 3680.

[63] D. A. Nivens, Y. K. Zhang, S. M. Angel, *Analytica Chimica Acta* **1998**, *376*, 235.

[64] A. Abdelghani, J. M. Chovelon, N. Jaffrezic-Renault, M. Lacroix, H. Gagnaire, C. Veillas, B. Berkova, M. Chomat, V. Matejec, *Sensors and Actuators B-Chemical* **1997**, *44*, 495.

[65] H. P. Kao, N. Yang, J. S. Schoeniger, *Journal of the Optical Society of America a-Optics Image Science and Vision* **1998**, *15*, 2163.

[66] M. D. Newsham, Michigan State University (East Lansing), **1988**.

[67] Y. Saito, H. Tanaka, Y. Sasaki, T. Azumi, *Journal of Physical Chemistry* **1985**, *89*, 4413.

[68] 3M, in *Specification sheet for FT-1.5-UMT fiber*, 3M Specialty Optical Fibers.

[69] Nichia, in *Specification sheet for Violet Laser Diode*, Nichia Corporation, Tokyo, Japan.

Chapter 2 – Hexanuclear molybdenum clusters for high temperature oxygen sensing

2.1 INTRODUCTION

Quenching of the fluorescence from organometallic compounds by oxygen has been used to develop a number of fiber-based sensors. A major drawback of these organometallic indicators for energy plant applications is that the chromophores degrade with time, have a limited operational temperature range, typically room temperature ±25°C, and lack long-term reliability. Previously, we developed a room temperature fiber optic oxygen sensor that utilizes the luminescence from hexanuclear metal halide clusters such as Mo_6Cl_{12}, **Figure 2.1**, to detect oxygen in the 0.1% (v/v) to 20% (v/v) range.[1] The organic polymers used to fabricate this device limited its operation to room temperature, but the cluster is known to be stable to at least 300°C in air.

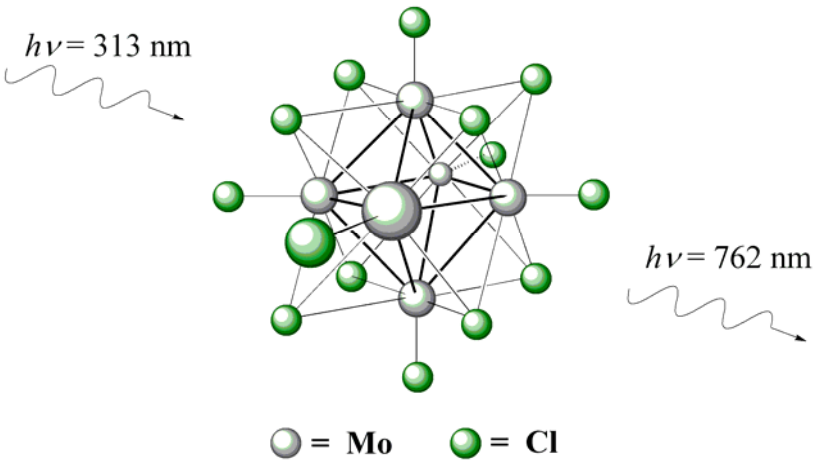

Figure 2.1. The Mo_6Cl_{12} cluster, the basis for an optical oxygen sensor.

A schematic of the reflection mode fiber sensor is shown in **Figure 2.2**. The molybdenum clusters are immobilized in an oxygen permeable matrix at the end of a silica fiber. An ultraviolet optical source, coupled into the other end of the fiber, is used to excite the clusters. The reflected luminescence signal is collected from the end of the fiber where the excitation light enters. This geometry allows for the "active" end of the fiber sensor to be immersed in a harsh environment, while the excitation and collection optics are located in a more benign environment.

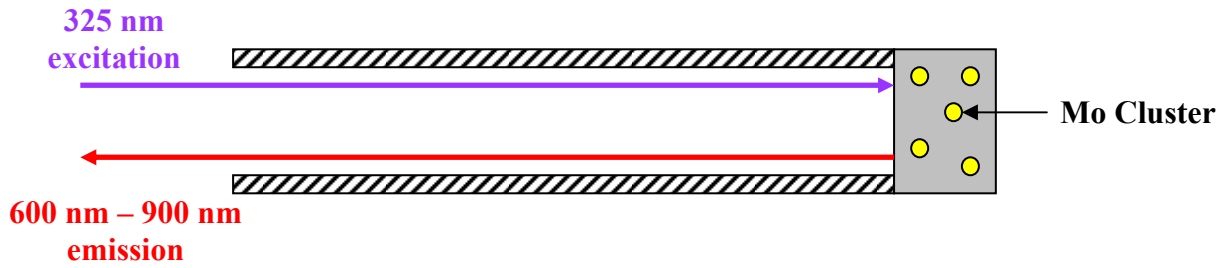

Figure 2.2. Schematic of the reflection mode fiber sensor. Figure courtesy of R. N. Ghosh.

The use of Mo_6Cl_{12} clusters offers particular advantages for the construction of practical fiber optic devices. The clusters are inexpensive and their synthesis is straightforward. The long lifetime of the cluster excited state (>100 μs) and the large emission Stokes shift (>400 nm) allows the use of simple light emitting diode (LED) excitation and Si photodiode detection, both of which are essential for commercial fabrication of the sensor. Other advantages of the metal halide clusters are that they can withstand repeated cycling and show no signs of decomposition for temperatures up to 250°C. Finally, the red luminescence emitted from the excited state of

the Mo cluster is quenched efficiently and selectively by ground state $^3O_2$. Since the ground state of all other gases typically present in power plant exhausts such as hydrogen, hydrocarbons, carbon monoxide, nitrogen oxides, and sulfur oxides do not have a triplet ground state; no cross-sensitivity with these species is expected.

The photophysics and physical properties of Mo_6Cl_{12} and related metal halide compounds[2] are well suited for oxygen sensing schemes. The extended cluster array has a quasiperovskite structure, composed of an octahedral core of molybdenum atoms with eight face-bridging chlorides and four axial chlorides, which are shared among neighboring cluster subunits.[3] The emissive excited state is localized in the metallic core of the cluster with little ligand character.[4] From a sensor perspective, these clusters are ideal luminescent probes because the emission is largely unaffected by the external environment, whether that be encapsulation in a sol–gel matrix or immersion in a gaseous environment. When dissolved in solution the clusters exist in the form $[Mo_6Cl_8]Cl_4L_2$ where $[Mo_6Cl_8]$ is the core of the cluster, Cl_4 are exchangeable chlorides sited in axial positions, and L is either a solvent molecule or another ligand, see **Figure 2.1**. The cluster can withstand repeated cycling, without degradation of the luminescence. The intensity of the luminescence decreases with increasing oxygen concentration, following the Stern–Volmer equation.[5] Under atmospheric conditions we have shown that gaseous oxygen can be detected from 0.1% (v/v) to 20% (v/v),[1] a range which is well suited for power plant applications such as emission control and individual burner balancing.

Shown in **Figure 2.3** are the absorption and emission spectra of the Mo-clusters in acetonitrile. Absorption of UV photons through the broad 300–400 nm absorption band excites the cluster. Emission of red luminescence from the lowest excited state is efficiently quenched by ground state $^3O_2$. Due to the large Stokes shift of >400 nm we are able to separate the excitation and emission signals using simple filtering techniques and then detect across the entire 600–850 nm emission band as the sensor signal using a simple photodiode detector.

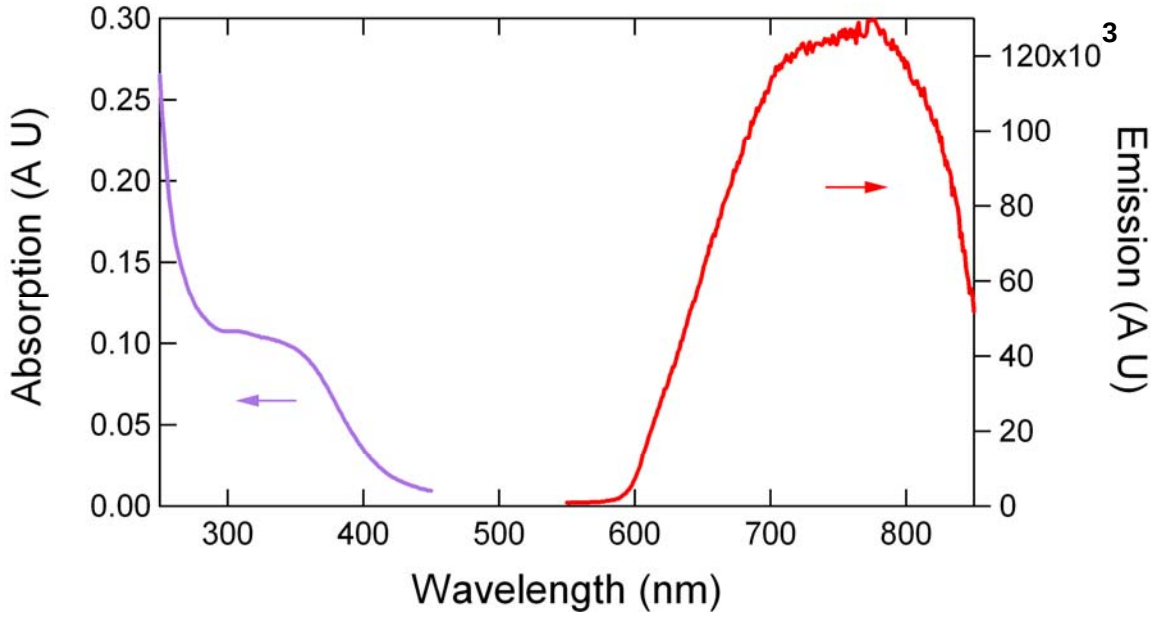

Figure 2.3. Absorption and emission spectra of the Mo_6Cl_{12} acetonitrile complex. The absorption band extends from 300 nm to 400 nm and the emission band extends from 600 nm to 850 nm. The large Stokes shift allows for simple LED excitation and photodiode detection, which are essential for volume fabrication of the sensor. The data was obtained by the author in collaboration with R. N. Ghosh.

Oxygen quenching of the luminescence is demonstrated in **Figure 2.4**. The luminescence spectra are shown in two gas environments: (a) argon (<0.005% (v/v) oxygen) and (b) air (~20% (v/v) oxygen). A factor of 5.5 decrease in emission intensity is seen at the emission maximum on going from the argon atmosphere to the air atmosphere.

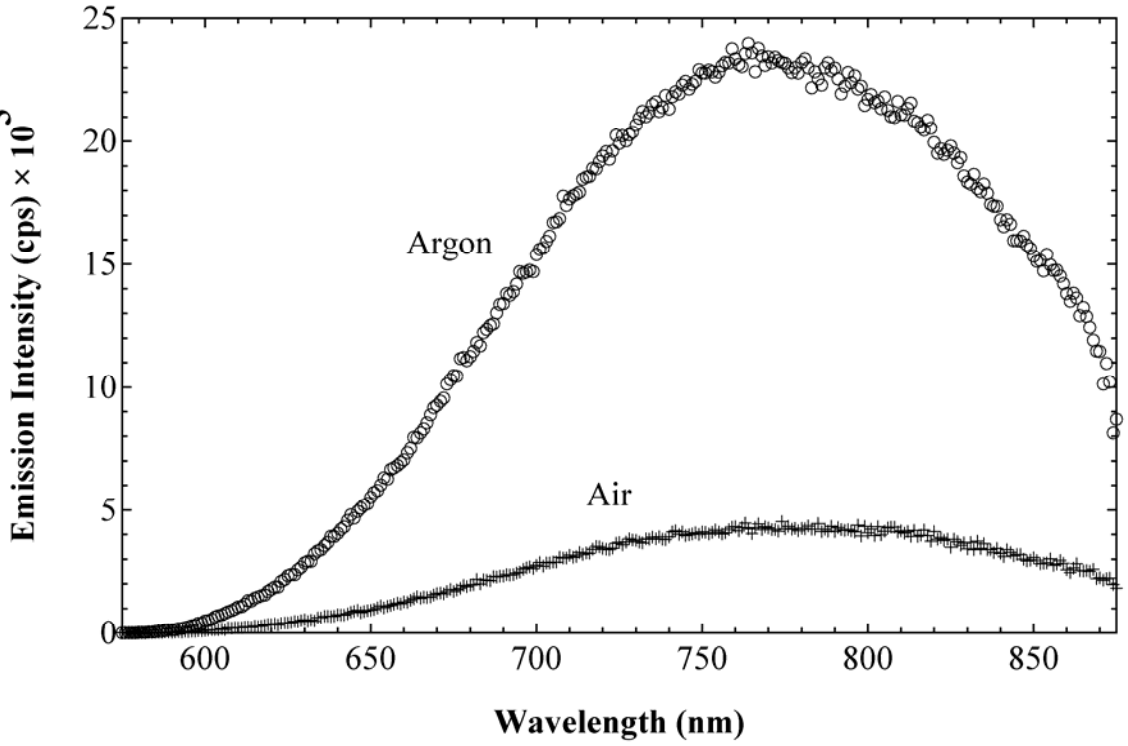

Figure 2.4. Luminescence spectra from the Mo-clusters demonstrating quenching by oxygen: (a) argon environment and (b) laboratory air (~20% (v/v) oxygen).[1]

A requirement of optical sensors based on luminescence quenching is that the luminescent probe has a strong emission that is efficiently quenched by oxygen, and that the oxygen has ready access to the luminescent probe. For a high-temperature sensor, these characteristics must hold over the entire temperature range of interest. A preliminary study of the high temperature stability of the Mo_6Cl_{12} clusters in oxygenated environments revealed irreversible changes in the optical absorption spectrum at >250°C and a loss of the red luminescence that is characteristic of pristine clusters. Thermal aging experiments run in air and under nitrogen point to oxidation of the clusters as the cause of the change in optical properties. X-ray powder diffraction

measurements on samples annealed at 300°C under controlled conditions are consistent with oxidation of Mo_6Cl_{12} to form MoO_3 as the principal degradation product. Two open axial coordination sites on the Mo_6Cl_{12} cluster lead to the polymerization of clusters through shared chlorine bridges. These open sites also are the likely source of the oxidative instability of Mo_6Cl_{12}. The known $M_2Mo_6Cl_{14}$ salts, where M is an alkali metal cation such as Na^+, K^+, or Cs^+ should be more thermally robust since there is a full complement of chloride ligands and no open sites for cluster aggregation or oxidation, i.e. chlorides must be lost from the cluster for the cluster to undergo degradation. The potassium salt of Mo_6Cl_{12} ($K_2Mo_6Cl_{14}$•$1H_2O$) was synthesized it was found that the alkali salts of Mo_6Cl_{12} are more stable that the parent compound. Optical and thermal aging experiments show that the alkali metal salts of Mo_6Cl_{12} have higher thermal stabilities and remain luminescent after long-term aging at 280°C.

2.2 EXPERIMENTAL

2.2.1 Materials

Ethanol (Koptec, anhydrous, USP), 2-propanol (Mallinckrodt, AR (ACS)), methanol (VWR), dichloromethane (Mallinckrodt, AR (ACS)), chloroform (Mallinckrodt, AR (ACS)), toluene (Mallinckrodt, AR (ACS)), and hexanes (Mallinckrodt, AR (ACS)), hydrochloric acid (Columbus Chemical Industries, electronics grade) were used as received. Acetonitrile (Spectrum Chemical Company, HPLC grade and EMD Chemicals, OmniSolv) were dried

overnight using activated molecular sieves (Spectrum Chemical, 1/16" pellets, type 4 Å) and then distilled from CaH_2 (Spectrum Chemical, anhydrous, desiccant, 40–20 mesh) prior to use. Ethanol (95%) was prepared by addition of Milli-Q water to absolute ethanol. The water used was either reverse osmosis (in-house) or deionized using a Millipore purification system (Milli-Q, 18 MΩcm). $MoCl_2$ was obtained from Cerac (lot 172938-A-1) or City Chemical (lots 40C65, 40M21, and 30L114). Anhydrous $MoCl_5$ (Strem, 99.6%, lot B035113), Bi powder (Strem, 99.9%, lot B7709023), potassium chloride crystals (Spectrum Chemical, Reagent A.C.S., lot QE7300) or (Columbus Chemical Industries, ACS grade, crystals), phenolphthalein (Spectrum Chemical, powder, Reagent A.C.S., lot LM0200), sodium hydroxide pellets (Mallinckrodt, AR (ACS), lot C41P01), potassium hydroxide pellets (Jade Scientific, ACS Reagent), concentrated sulfuric acid (Fisher Scientific, Reagent grade and (Columbus Chemical Industries, ACS/Reagent grade), hydrofluoric acid (JT Baker, technical grade, 47.0-52.0%, lot J22906), glacial acetic acid (Fisher Scientific certified ACS Plus, lot 993730), H_2O_2 (Fisher, 30%), 8-hydroxyquinoline (Sigma-Aldrich, 99+%), and tetrabutylammonium chloride (Fluka, purum, ≥97% (Cl), lot 1327989) were used as received. Amberlite IRA-67 ion-exchange resin (Aldrich, batch 07009AE) was mixed with 1 M hydrochloric acid, poured into a column, and then filtered to remove the hydrochloric acid. Holmium(III) oxide, Ho_2O_3, (Aldrich, 99.999%) was used as received. Potassium dichromate, $K_2Cr_2O_7$, (Mallinckrodt, Analytical Reagent (AR), lot KTCA) was recrystallized 2× using reverse osmosis water. Medium-fast filter paper (Whatman, 150 mm diameter circles, #1 qualitative) or (Whatman, 185 mm diameter circles, #1 qualitative), borosilicate microfiber filters (Micro Filtration Systems, GD120 grade, 47 mm diameter), 350-

mL fritted funnel (Pyrex, ASTM 10-15 M), 350-mL fritted funnel (Kimax, 80 C), 350-mL fritted funnel (ACE Glass, POR A, ASTM 145-175), 60-mL fritted funnel (ChemGlass, medium porosity), cellulose extraction thimble (Whatman Inc., 33 mm × 94 mm, single thickness), and syringe filters (Whatman Inc., 4 μm pore size) were used as received. All glassware used for spectroscopic measurements was cleaned by soaking in concentrated hydrochloric acid, scrubbed with water and Alconox soap, rinsed with reverse osmosis water, and then oven dried prior to use.

2.2.2 Synthesis of bis(hydroxonium)tetradecachlorohexamolybdate hexahydrate, $(H_3O)_2Mo_6Cl_{14}•6H_2O$ – Method A.[6]

$MoCl_2$ was received as a yellowish-green powder with small dark-blue specks and was purified by conversion to the Mo_6Cl_{12} hydrochloride salt, $(H_3O)_2Mo_6Cl_{14}•6H_2O$. A representative procedure is described. $MoCl_2$ (2 g, 2 mmol) and a Teflon coated magnetic stir bar were added to a 1-L Erlenmeyer flask. With stirring, the solids were dissolved in 800 mL of boiling 6 M HCl. The resulting bright-yellow solution was then filtered through medium-fast filter paper to remove insoluble white and metallic particles. The filtered solution was heated on a hot plate and the volume reduced to 200 mL. The hot plate was turned off and the solution was left on the hot plate to slowly cool to room temperature. A small amount of seed crystals were added and yellow crystals formed overnight. After cooling the solution in an ice bath for 5 hours, the resulting yellow crystals of the hydrochloride salt were collected by gravity filtration through Whatman medium-fast filter paper. The crystals were then placed onto several pieces of filter

paper and allowed to dry under ambient conditions for two days to give 586 mg (24.1% yield) of long yellow needles. A second crop of crystals was obtained by heating to concentrate the mother liquor to 100 mL, filtration, and a further reduction in volume to 50 mL. Cooling, seeding the solution as described above, and storing the solution in a freezer overnight yielded long yellow needles. Drying the needles on filter paper yielded 256 mg (10.5% yield) of the Mo_6Cl_{12} hydrochloride salt. The products were characterized using X-ray powder diffraction, UV-Visible spectroscopy, fluorescence spectroscopy, and energy dispersive X-ray spectroscopy.

2.2.3 Synthesis of bis(hydroxonium)tetradecachlorohexamolybdate hexahydrate, $(H_3O)_2Mo_6Cl_{14}\cdot 6H_2O$ – Method B.[7]

All starting materials were handled in a dry box under a dinitrogen atmosphere. A tube furnace with a positionable thermocouple was used in conjunction with a temperature controller in order to maintain and ramp temperatures. Syntheses were performed in dual-chamber borosilicate glass ampoules (**Figure 2.5**). The ampoule and inlet adapter were oven-dried at 130°C overnight and cooled in the dry box antechamber. Reactants were thoroughly mixed and added to the end reaction chamber via a long-stem funnel that minimized contamination of the constriction surfaces. The ampoule was evacuated on a Schlenk line and flame-sealed between the Cajon® fitting and receiving chamber. The molybdenum content of products were determined gravimetrically as $MoO_2(C_9H_6ON)_2$ (C_9H_6ON = 8-hydroxyquinolinate).[8]

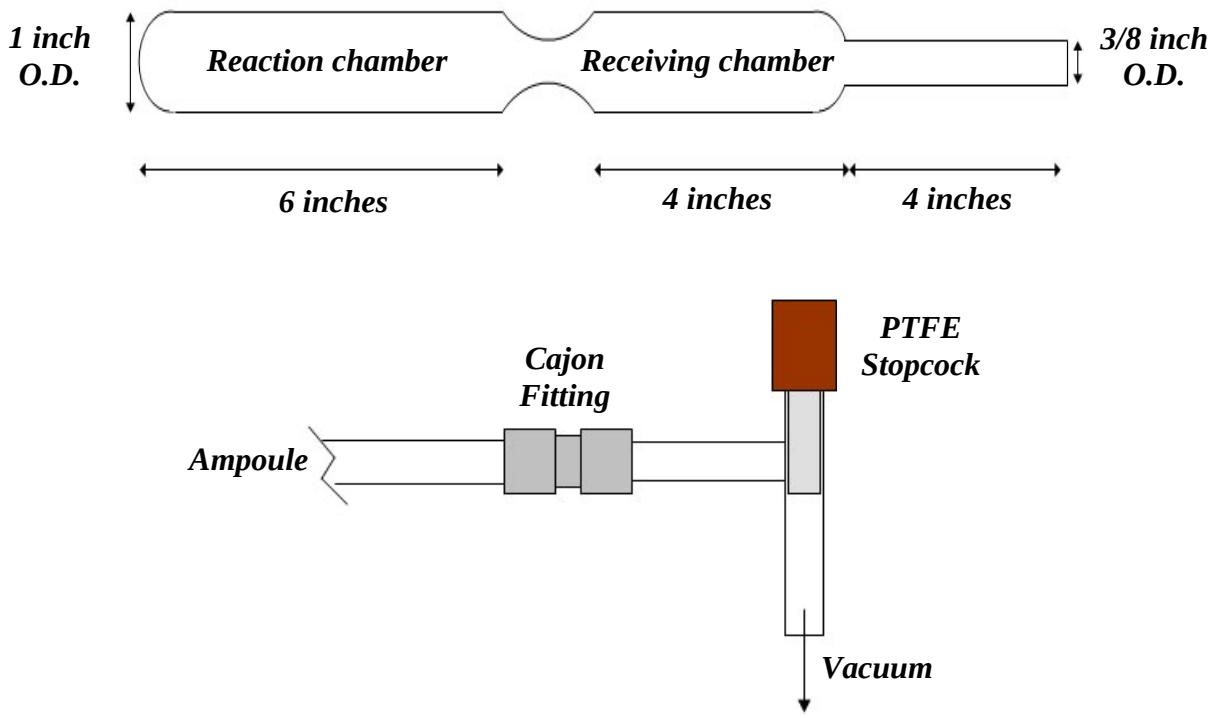

Figure 2.5. Schematic of reaction assembly used to synthesize $(H_3O)_2Mo_6Cl_{14}•6H_2O$.

Table 2.1. Heating parameters for synthesis of $(H_3O)_2Mo_6Cl_{14}•6H_2O$.

Procedural Step	Duration
Heat to 20–230°C	2 hrs.
Heat to 230–350°C	2 hrs.
Heat at 350°C in tube furnace.	72 hrs.
Rotate every 2 hours to mix reagents.	12 hrs.
Rotate every 2 hours to mix reagents.	5 hrs.
Pull receiving chamber out of furnace and sublime $BiCl_3$.	5 hrs
Push receiving chamber back into furnace, melt $BiCl_3$, and tilt to recombine with reagents.	2 hrs.
Pull receiving chamber out of furnace and sublime $BiCl_3$.	5 hrs.
Cool from 350°C–20°C	12 hrs.
Homogenize by shaking	30 min.
Heat to 20–350°C	3 hrs.
Tilt furnace to 15° from horizontal, pull out receiving chamber, and heat at 350°C	24 hrs.
Cool to 20°C	5 hrs.

It was found that the above parameters improved the yield from 77% to 88%. Up to 4× the amount of reagents in the same size ampoule achieved yields ≥77%. The initial yield of crude Mo_6Cl_{12} based on $MoCl_5$ is always high. Three recrystallized samples were sent to Schwarzkopf Microanalytical and they found 750 ppb Bi for a sample that was only recrystallized once, and ≤100 ppb Bi in the remaining samples that had been recrystallized three times. The x-ray powder diffraction pattern of material that was recrystallized three times matched literature.[9] It was found that the recrystallization parameters using 2.00 g of crude product, 25 mL concentrated HCl, and a Bunsen burner worked well as long as the crude product was not exposed to air for more than one day. If the crude product was exposed to air for more than one day, the product did not dissolve well and required multiple extractions with boiling concentrated HCl to dissolve all of the product. The yield for $(H_3O)_2Mo_6Cl_{14}•6H_2O$ based on $MoCl_5$ was 85.1% (average of three trials). Chloromolybdic acid was soluble in acetonitrile, methanol, and ethanol, but it formed a white insoluble precipitate when mixed with water. In air, the solid gradually changed to a pale yellow solid with loss of HCl.

2.2.4 Synthesis of hexamolybdenum dodecachloride, Mo_6Cl_{12}.

Recrystallized samples of chloromolybdic acid (~0.809 g) were heated in vacuo using the method of Dorman and McCarley[10] by slowly (2.5 hours) raising the temperature to 350°C and heating for 24 hours. The resulting material was always olive-green, not yellow, using this method. X-ray powder diffraction of the olive-green material gave the characteristic amorphous pattern consistent with approximately anhydrous Mo_6Cl_{12}. Yellow, anhydrous, Mo_6Cl_{12} was

obtained by heating the solid in vacuo at 150°C for 2 hours and then increasing the temperature to 210°C and heating overnight under vacuo — a method described by Mussell.[11] The anhydrous Mo_6Cl_{12} changed from olive-green to a pale yellow after six days of exposure to air under ambient conditions. The change in color is characteristic of water absorption by the sample. The yield for conversion to anhydrous Mo_6Cl_{12} was 91.8% (average of three trials). Molybdenum content was determined by gravimetric determination. *Anal. Calc.* for $Mo_6Cl_{12}•2H_2O$: Mo, 55.50%. Found: Mo, 55.46% (average of two trials).

2.2.5 Preparation of the acetonitrile complex of Mo_6Cl_{12}. ($Mo_6Cl_{12}•2CH_3CN$)

The Mo_6Cl_{12} hydrochloride salt was heated under vacuum at 210°C for 12 hours to yield Mo_6Cl_{12} and the resulting yellow powder was loaded into the thimble of a pre-dried Soxhlet extraction apparatus. Dry acetonitrile (250 mL) was added to the extractor and the receiving flask was heated to start the extraction process. After 3 days, the yellow solution was removed and concentrated to 10 mL. The products were characterized using UV-Visible and fluorescence spectroscopy. $Mo_6Cl_{12}•2CH_3CN$ was also directly prepared from $MoCl_2$ from City Chemical (lot 40C65, 40M21, and 30L114) using the same procedure.

2.2.6 Synthesis of bis(potassium)tetradecachlorohexamolybdate monohydrate, $K_2Mo_6Cl_{14}•1H_2O$. (FJ-17, MM-5, MM-7, MM-8, MM-9)

With heating, dry Mo_6Cl_{12} (City Chemical, 1.0546 g, 1.055 mmol) was dissolved in 500 mL of 6 M HCl in a 1-L Erlenmeyer flask. The hot solution was filtered (Whatman, medium speed) and then the volume was reduced to 250 mL by boiling. A saturated solution of KCl in 6 M HCl (200 mL) was added to hot solution, and then the volume was further reduced to 150 mL by boiling. After cooling slowly to room temperature and an additional 24 hours at room temperature, yellow needle-like crystals of $K_2Mo_6Cl_{14}•1H_2O$ were collected by filtration. Drying under ambient conditions for three days yielded 1.0132 g (82.2% yield) of $K_2Mo_6Cl_{14}•1H_2O$ as bright yellow crystals. The products were characterized using X-ray powder diffraction, UV-Visible spectroscopy, fluorescence spectroscopy, and energy dispersive X-ray spectroscopy, and thermogravimetric analysis.

2.2.7 Synthesis of anhydrous bis(potassium)tetradecachlorohexamolybdate, $K_2Mo_6Cl_{14}$.

A Pyrex® drying tube was fabricated that consisted of a 45.7 cm long × 1.9 cm I.D. Pyrex® glass tube. On one end a glass cap was clamped to the tube with a rubber o-ring to seal the joint. The other end was clamped to a PTFE inlet adapter with a rubber o-ring in between. The tube was connected to another double inlet adapter using a Cajon® fitting. The double inlet adapter allowed the drying tube to be removed for weighing. The double inlet adapter was attached to the vacuum manifold via red rubber tubing. A piece of oven dried glass wool was placed into

the tube between the sample and the vacuum connection to insure that no sample was lost when applying vacuum. The entire assembly, including the tube, cap, o-rings, inlet adapter (not the double inlet adapter), and the glass wool were weighed. A sample of $K_2Mo_6Cl_{14}•1H_2O$ (60.37 g, 0.05249 mol) was placed into the drying tube and the end cap was clamped on. The assembly was then reweighed, placed into a tube furnace, attached to the double inlet adapter, and vacuum slowly applied. After reaching full vacuum, the furnace temperature was raised to 100°C. The sample was dried to constant mass over a period of 3 days and yielded 59.83 g of $K_2Mo_6Cl_{14}$ (anhydrous).

2.2.8 Synthesis of bis(tetrabutylammonium)tetradecachlorohexamolybdate, $(^nBuN)_2Mo_6Cl_{14}$.

Tetrabutylammonium chloride (21.4 g, 77.0 mmol) was dissolved in an Erlenmeyer flask with 100 mL of absolute ethanol. $(H_3O)_2Mo_6Cl_{14}•6H_2O$ (7.8 g, 6.42 mmol) was placed into an Erlenmeyer flask and dissolved in 100 mL absolute ethanol while stirring on a hot plate/stirrer at boiling point. After dissolving the $(H_3O)_2Mo_6Cl_{14}•6H_2O$, the tetrabutylammonium chloride solution was added and a powdery yellow precipitate immediately formed. The precipitate was dissolved by heating and then the solution was allowed to slowly cool to room temperature overnight. The yellow powdery solid product was collected by filtration and weighed after drying to give 9.78 g (97.8% yield). The yellow powder was then recrystallized from dichloromethane to give beautiful orange plate-like (some cubes) crystals which had a mass of 4.46 g (45.6% recovery). Two more crops were obtained by reduction in volume to give 3.13 g

(32.0% recovery) and 0.683 g (6.98% recovery). The crops were combined once X-ray powder diffraction confirmed that they were the same.

2.2.9 Thermogravimetric analysis.

Isothermal aging of clusters were run in air using a Perkin Elmer TGA-7 system, which consists of a computer, TGA-7 low temperature furnace and balance module, and a TAC7/DX controller. The flow-rate of balance and sample gas was 45 and 40 mL/min respectively. The pan, stirrup and hanger wire were made of platinum metal that was connected to a gold balance wire using a quartz hook. Samples were first equilibrated at 115°C for 1 hour to remove residual water, and then heated to 280°C at a rate of 10° per minute. The gas type and flow were adjusted to either house nitrogen or air with a separate gas flow regulation system that was attached.

2.2.10 X-ray powder diffraction.

The X-ray diffraction (XRD) powder patterns of products were taken at room temperature on a Rigaku-Denki RW400F2 (Rotoflex) diffractometer equipped with monochromatized Cu Kα (λ = 1.540598 Å) rotating anode operating at 45 kV and 100 mA with a 2°/min scan rate. Samples were prepared by using a spatula to evenly distribute a small amount of powdered sample on double-sided tape mounted on a microscope slide. After pressing gently to ensure that the sample adhered to the tape, the microscope slide was gently tapped on its side to dislodge any loose powder. A potassium chloride standard was prepared and analysed periodically between

samples to determine the consistency of measurements taken at different times. The diffraction peaks also served as reference points for calibration of 2θ along the x-axis.

2.2.11 Single-crystal x-ray diffraction.

Intensity data were collected on single-crystals of $(H_3O)_2Mo_6Cl_{14}•6H_2O$ and $K_2Mo_6Cl_{14}•1H_2O$ at room temperature with a Siemens Platform SMART[12] CCD X-ray diffractometer. Crystals of suitable size were mounted on glass fibers. Both data sets (Mo Kα radiation, λ = 0.71073 Å) were acquired up to 66.5° in 2θ, covering either a full sphere or a hemisphere of reciprocal space.

2.2.12 Elemental analysis.

Several samples were sent to Schwarzkopf Microanalytical to determine chemical composition. Additionally, the chemical composition of Mo_6Cl_{12}, $(H_3O)_2Mo_6Cl_{14}•6H_2O$, and $K_2Mo_6Cl_{14}•1H_2O$ were determined by energy dispersive X-ray spectroscopy (EDS) using a JEOL JSM-6400 scanning electron microscope (SEM) equipped with a NORAN Inc. EDS detector. The analysis was conducted at accelerating voltage 20 kV and collection time of 120 s. The results of the elemental analysis for several crystals of each compound were averaged. The ratios were consistent with the formulas of Mo_6Cl_{12}, $(H_3O)_2Mo_6Cl_{14}•6H_2O$, and $K_2Mo_6Cl_{14}•1H_2O$.

2.2.13 Absorption spectroscopy.

Absorption spectra were measured using a Perkin-Elmer Lambda 40 series double beam UV-Visible spectrometer. Data analysis was performed using the UV Win lab (version 2.80.03) software package supplied with the instrument and plotted using Microsoft Excel. Solutions were placed into a 1 cm pathlength quartz cuvette with a separate cell containing only solvent as a reference. Wavelength and absorbance were calibrated using methods described by Perkampus.[13] For routine calibration of the wavelength scale, Ho_2O_3 (350 mg, 0.93 mmol) was dissolved in 10 mL of concentrated HCl. For routine calibration of the absorbance scale, a 0.005 M H_2SO_4 solution was prepared by adding 0.28 mL of concentrated H_2SO_4 to a 1-L volumetric flask and then diluting to the mark with Milli-Q water. Solution A (for the range 0.2 $\leq$ Absorbance $\leq$ 0.7) was prepared by adding $K_2Cr_2O_7$ (50.2 mg, 0.171 mmol) to a 1-L volumetric flask and diluting to the mark with 0.005 M H_2SO_4. Solution B (for the range 0.4 $\leq$ $A \leq 1.4$) was prepared by adding $K_2Cr_2O_7$ (100.5 mg, 0.342 mmol) to a 1-L volumetric flask and diluting to the mark with 0.005 M H_2SO_4.

Samples were prepared by weighing 2–3 mg of Mo_6Cl_{12} in a small sample vial. The compound was then dissolved in a small amount of dry acetonitrile and transferred to a 10-mL volumetric flask. The volumetric flask was filled to the mark, stoppered, and shaken to ensure a homogenous solution. Typical concentrations were c.a. 1.7×10^{-4} M.

2.2.14 Fluorescence spectroscopy.

The fluorescence measurements were performed using a Fluorolog-3 instrument from Instruments S.A., Inc. The system includes a single Czerny-Turner excitation monochromator with a 1200 g/mm ruled grating blazed at 330 nm and a single Czerny–Turner emission monochromator with a 1200 g/mm holographic grating blazed at 630 nm. The excitation optics consist of a 450W ozone free Xe lamp (Oriel 6266), followed by a 270 nm – 380 nm bandpass filter (Oriel 1124). A Si photodiode is used to monitor the lamp signal continuously. The detection optics consist of a 603.2 nm long wave pass filter (CVI, Inc.) followed by a multi-alkali photomultiplier tube (Hamamatsu R928) with photon counting electronics. Data processing was performed using the Datamax (version 2.2) software package supplied with the instrument. Spectra were obtained by exciting at 313 nm and scanning the emission monochromator from 550 nm to 850 nm. Newport 1815-C Power meter with and 818 UV Silicon detector was used to monitor the Xe lamp intensity at the 313-nm excitation wavelength, before and after the emission measurements. After an initial warm up time of half an hour, the lamp was found to have output power stable to within ±5% for a period of several hours. These power measurements allow quantitative comparison of spectra obtained on different days by accounting for long term reduction of the Xe lamp output due to aging.

Measurements of cluster fluorescence in solution were performed by placing the solution in a quartz cuvette sealed with an airtight septum. Spectra were measured in laboratory air and high purity nitrogen (AGA, Inc, 99.999% (v/v)). Prior to obtaining spectra, all gases were bubbled through the solution for 10 to 15 minutes at a rate of ~10 mL/min. via a syringe needle inserted through the septum. For the measurements of the potassium salts in HCl a glass pipette was used

to transfer gases through the solution. Two types of spectra are presented. The "uncorrected spectra" are the raw data from the photomultiplier tube, without correcting for the spectral response function of either the PMT or the emission grating. Therefore the "uncorrected spectra" do not show the true emission lineshape. The "corrected spectra" include corrections for the spectral response of the PMT and the emission grating, and represents a profile that is close to the true emission lineshape. The "uncorrected spectra" will show a peak in the 670 nm – 680 nm range, and a constant background offset of 500 cps – 1000 cps that is associated with the PMT dark current. The "corrected spectra" have a broad peak in the 720 nm – 760 nm range, without any background offset. A comparison of the corrected and uncorrected data is presented in **Figure 2.6**.

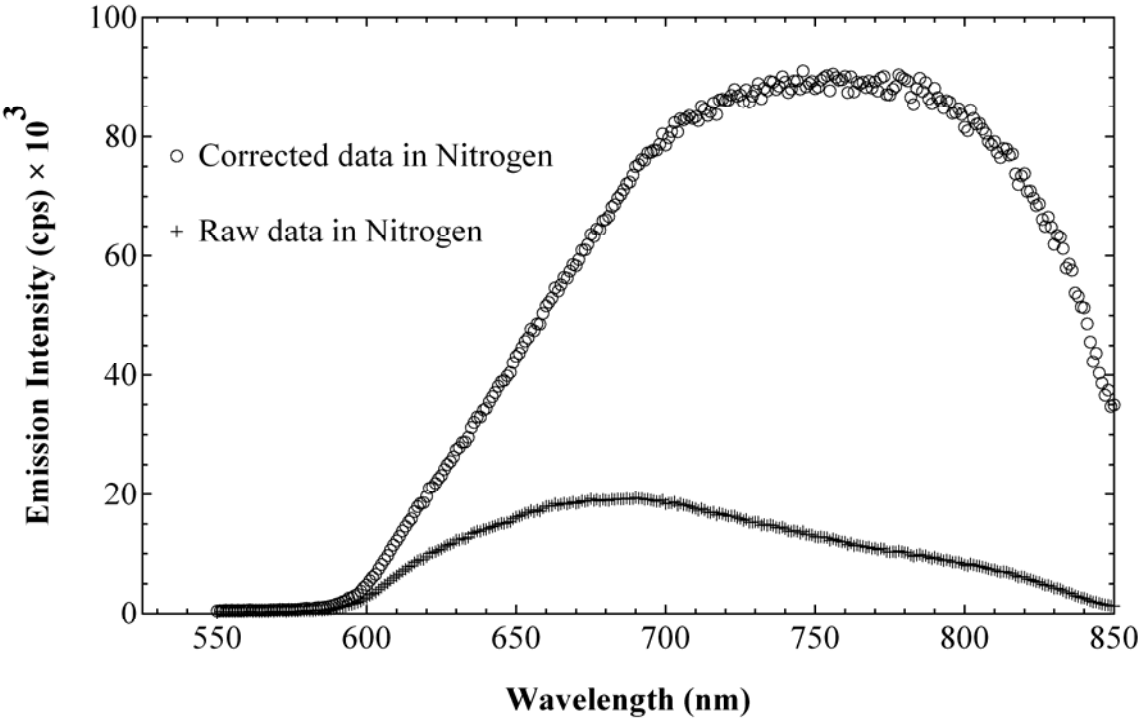

Figure 2.6. Comparison of corrected and uncorrected emission spectra for $K_2Mo_6Cl_{14}$. The data was obtained by the author in collaboration with R. N. Ghosh.

2.2.15 Optical microscopy of clusters.

Optical microscopy images were acquired using a Nikon Optiphot2-Pol microscope equipped with a Sony Hyper HAD CCD-IRIS/RGB color video camera (model DXC-151A). The camera was connected to a PC using a Sony camera adapter (model CMA-D2). The images were viewed using a Sony Trinitron color video monitor and captured using Hauppage Computer Works Win/TV software (version 2.4.17052). Images were collected at angles of 0° and 90° to characterize the birefringence of the samples and as a qualitative measure of their degree of crystallinity. A programmable hot stage (Mettler FP82) designed for the microscope was used to heat samples while collecting images at elevated temperatures. The images were collected every 10°C and analyzed for mean luminosity using Adobe® Photoshop®, which provides a measure of the light emission from the sample over the entire visible spectrum. The mean luminosity was then plotted as a function of temperature and each sample contained approximately 4 mg of cluster.

2.3 RESULTS AND DISCUSSION

2.3.1 Synthesis, purification, and characterization of Mo_6Cl_{12}

Mo_6Cl_{12} can be synthesized directly from $MoCl_5$ and aluminum at 450°C[10] or obtained from several commercial sources. As-received $MoCl_2$ from Cerac, Inc. and City Chemical, LLC was purified by dissolution in 6 M HCl to form the hydrochloride salt $(H_3O)_2Mo_6Cl_{14}•6H_2O$, followed by concentration of the solution and cooling to precipitate the purified clusters as a canary yellow solid. Details of the process appear in the Experimental section. Proof of

structure was obtained by comparing the X-ray powder diffraction (XPD) pattern (**Figure 2.7**) of a collection of crystals with that of authentic samples. As shown in the Figure inset, $(H_3O)_2Mo_6Cl_{14}•6H_2O$ crystallizes as an octahedral core of 6 Mo atoms with 8 chlorides bound to each face of the octahedron. The remaining 6 chlorides are located at chemically labile axial positions, which allows for a limited number of substitution reactions. Heating the hydrochloride salt to >200°C drives off 2 equivalents of HCl, converting the cluster to Mo_6Cl_{12}. The XPD (red line in **Figure 2.7**) shows that the product is amorphous.

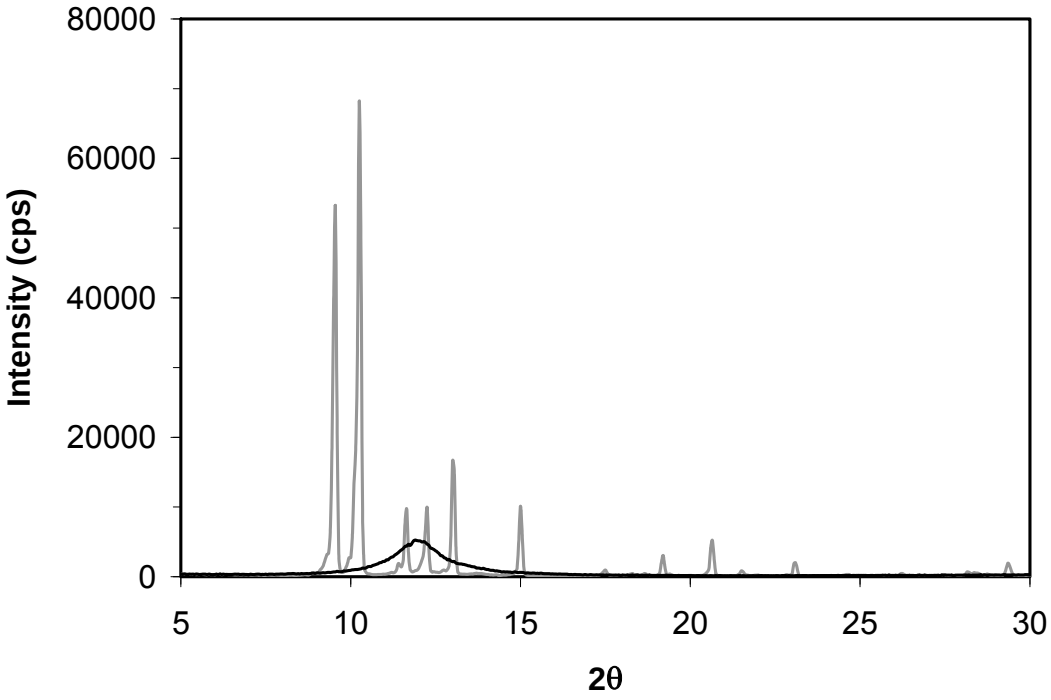

Figure 2.7. The x-ray powder diffraction patterns for unheated $(H_3O)_2Mo_6Cl_{14}•6H_2O$ (gray line), and Mo_6Cl_{12} (black line), obtained by heating the hydrochloride salt under vacuum to 150°C for 2 hours then increasing the temperature to 210°C. Once at 210°C, the sample temperature is maintained overnight.

The loss of two chlorides leaves two open coordination sites, and in solid state structures, these two sites form cluster-to-cluster bridges through chlorides. Experience has shown that Mo_6Cl_{12} is hygroscopic, reversibly taking up water that is presumably coordinated to the open coordination sites.

Thermogravimetric analysis (TGA) of Mo_6Cl_{12} in air (**Figure 2.8**) shows that Mo_6Cl_{12} undergoes a gradual weight loss from room temperature to 250°C.

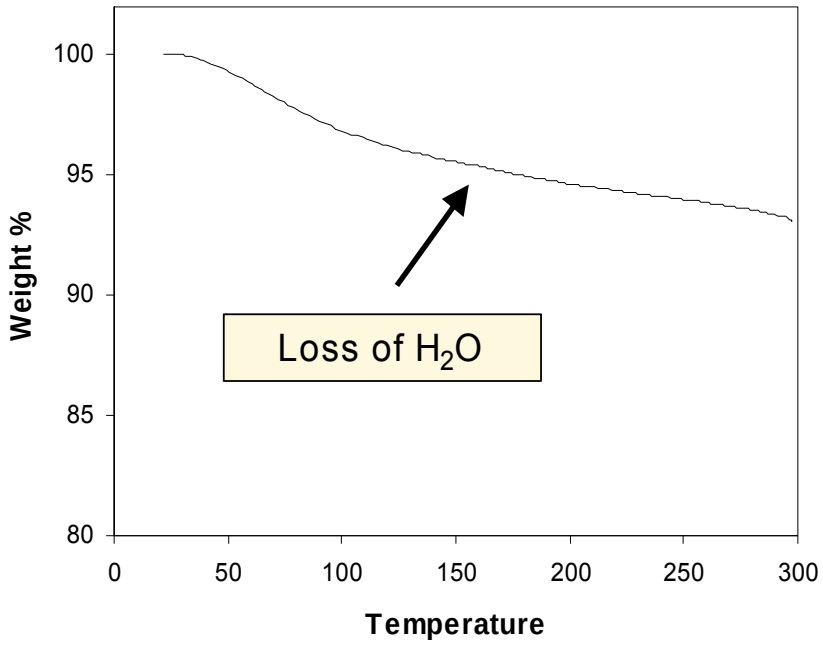

Figure 2.8. Thermogravimetric analysis of Mo_6Cl_{12}. The sample was heated at a rate of 10°C/min in air.

The percent weight loss is small (~5%) and reversible, with the weight loss dependent on the rigor in which the compound was protected from moisture. For example, Mo_6Cl_{12} that has been

rigorously dried under vacuum at 200°C shows no appreciable weight loss to 250°C. However, Mo_6Cl_{12} heated in air to >250°C undergoes irreversible changes in its structure and optical properties. Isothermal aging of Mo_6Cl_{12} at 300°C for 1 hour in air transformed the canary yellow Mo_6Cl_{12} into a gray solid. Chemical analysis of the gray material provided an empirical formula of $Mo_{1.0}O_{3.7}$; nitrogen, hydrogen, carbon, and chlorine were present at the ≤1% level.

The apparent oxidation of Mo_6Cl_{12} caused substantial changes in the optical properties of the clusters. An optical microscope equipped with a hot stage provided a convenient but qualitative understanding of the evolution of the optical properties of Mo_6Cl_{12} with temperature. A sample of pristine Mo_6Cl_{12} was heated on a hot stage at 10°C/min in air, and images of Mo_6Cl_{12} were concurrently captured and evaluated using commercial imaging software. Shown in **Figure 2.9** is a plot of the "luminosity" (i.e. reflected light) from three independent Mo_6Cl_{12} samples as a function of temperature.

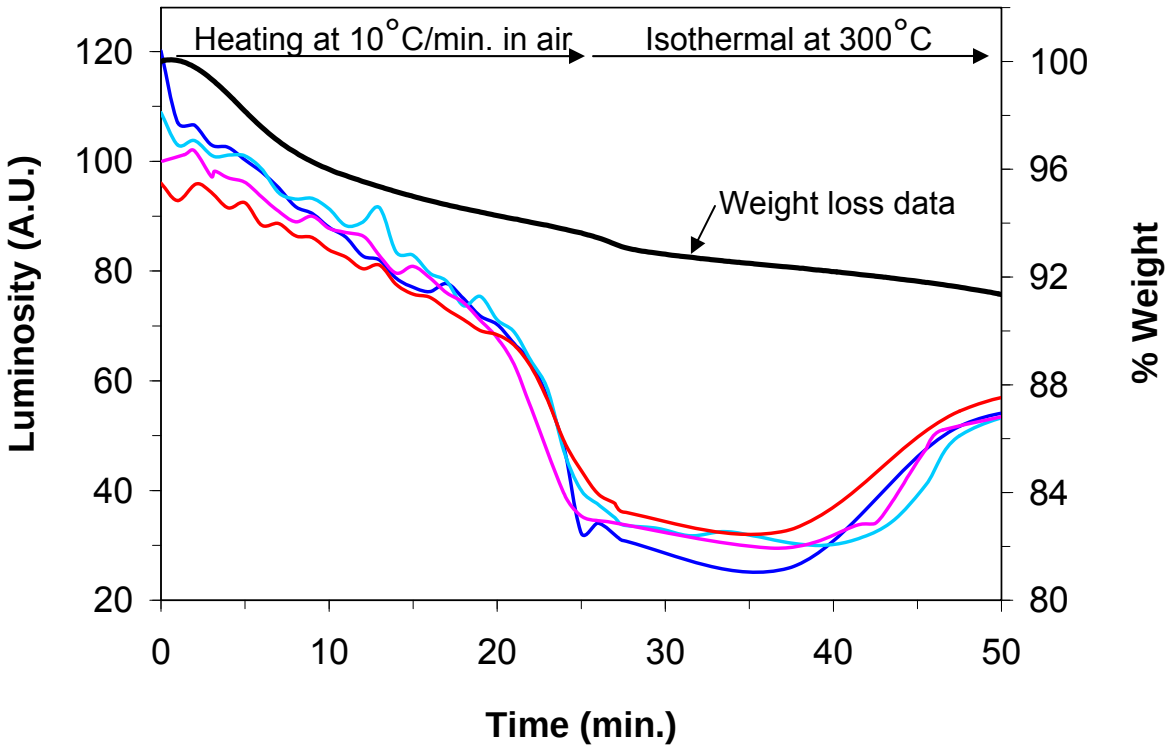

Figure 2.9. Changes in the luminosity of Mo_6Cl_{12} caused by heating in air. Weight loss data measured under the same heating protocol are shown for comparison.

Results for a TGA experiment run under the same conditions are included for comparison. The data show that decreases in luminosity and weight track each other up to 250°C. These changes are reversible. At T >250°C, the evolution of the changes in optical properties is irreversible, and isothermal aging at 300°C leads to further changes in the luminosity and weight loss. These thermally-induced changes were measured quantitatively by isothermal aging of pristine samples of Mo_6Cl_{12} for 1 hour at a series of temperatures, and after cooling to room temperature,

measuring their properties by UV-Visible and fluorescence spectroscopy. As shown in **Figures 2.10** and **2.11**, aging Mo_6Cl_{12} at T <250°C caused negligible changes in the optical properties of the clusters. However the absorption spectra of samples aged at T >250°C showed substantial changes, most importantly, a large decrease in luminescence compared to pristine Mo_6Cl_{12}.

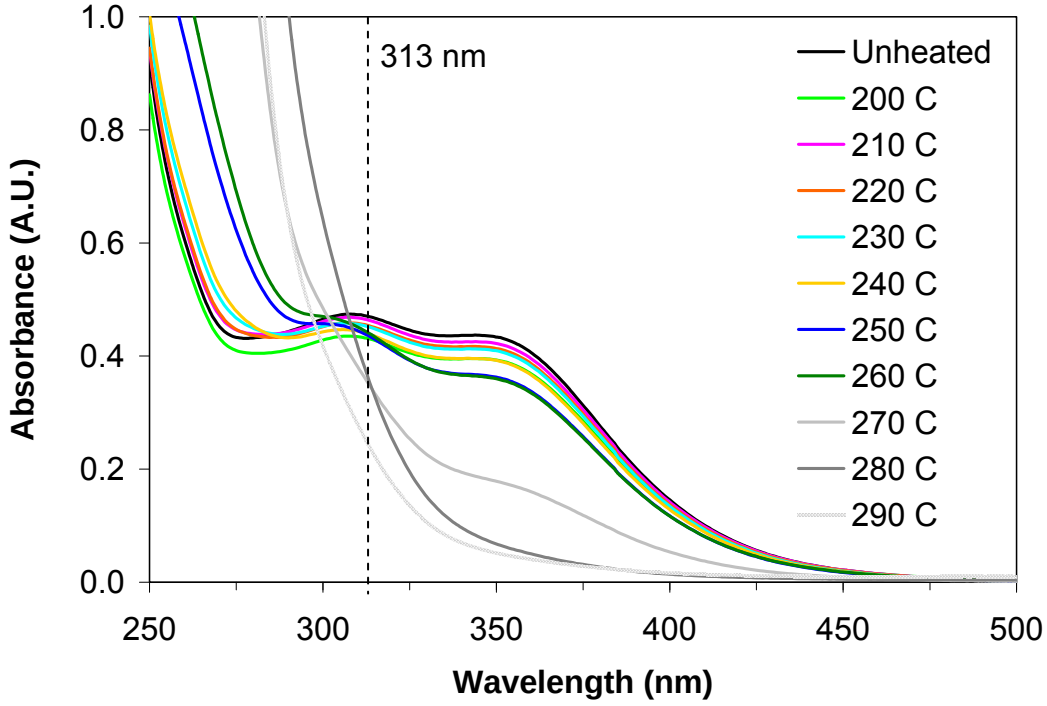

Figure 2.10. Absorption spectra of Mo_6Cl_{12} solutions in 6 M HCl after isothermal aging at the indicated temperatures.

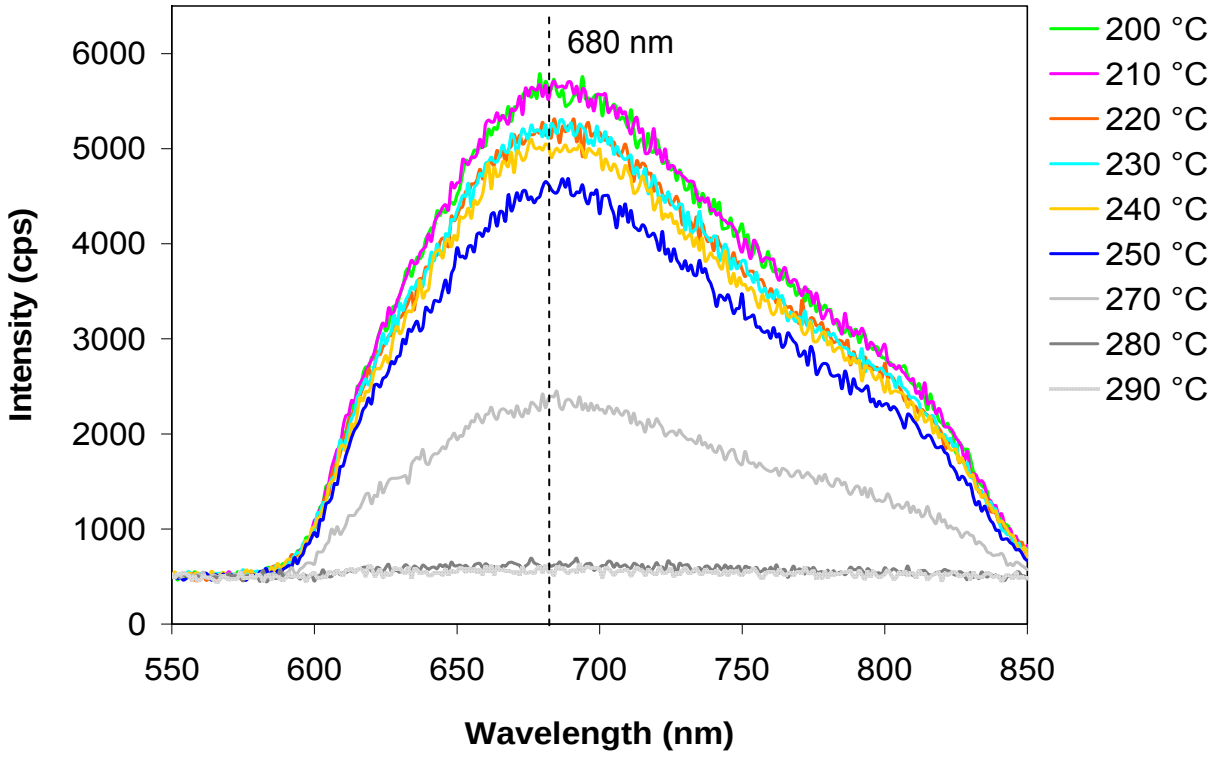

Figure 2.11. Uncorrected emission spectra of Mo_6Cl_{12} solutions in 6 M HCl after heating to the indicated temperature.

To confirm the nature of the oxidation product, Mo_6Cl_{12} was aged in air at 300°C for 1 hour, and the resulting gray powder was analyzed by x-ray powder diffraction. The gray powder had a fairly simple diffraction pattern (**Figure 2.12**), and a comparison of the diffraction pattern with that of MoO_3 shows that the two are nearly identical, consistent with Mo_6Cl_{12} degrading via oxidation to MoO_3.

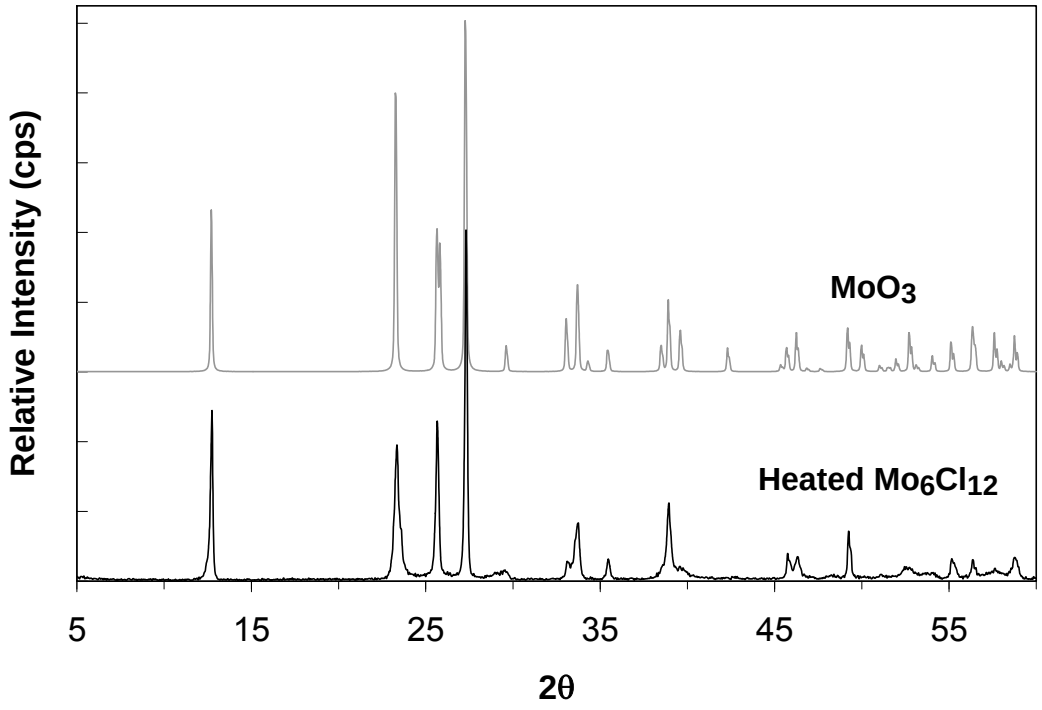

Figure 2.12. X-ray powder diffraction pattern data for Mo_6Cl_{12} after heating at 300°C for 1 hour in air using a microscope hot stage (lower trace). The pattern is a good match for the known pattern of MoO_3 (upper trace) available from the International Centre for Diffraction Data, Powder Diffraction File #35-0609.

While 250°C appears to be the upper limit of stability for Mo_6Cl_{12} in air, samples tolerate cycling at slightly lower temperatures. For example, the luminescence spectra in **Figure 2.13**, demonstrate that heat cycling to 200°C does not affect the cluster photophysics. In **Figure 2.13** the emission spectra of (i) our previously synthesized clusters[1] is compared to (ii) the present material that has been cycled in air three times from room temperature to 200°C. The spectra are taken in a nitrogen (<0.001% (v/v) oxygen) environment. The data show no change in the line shape (the divergence at shorter wavelengths is due to the use of a different high pass filter for the two experiments) confirming the stability of the clusters up to 200°C.

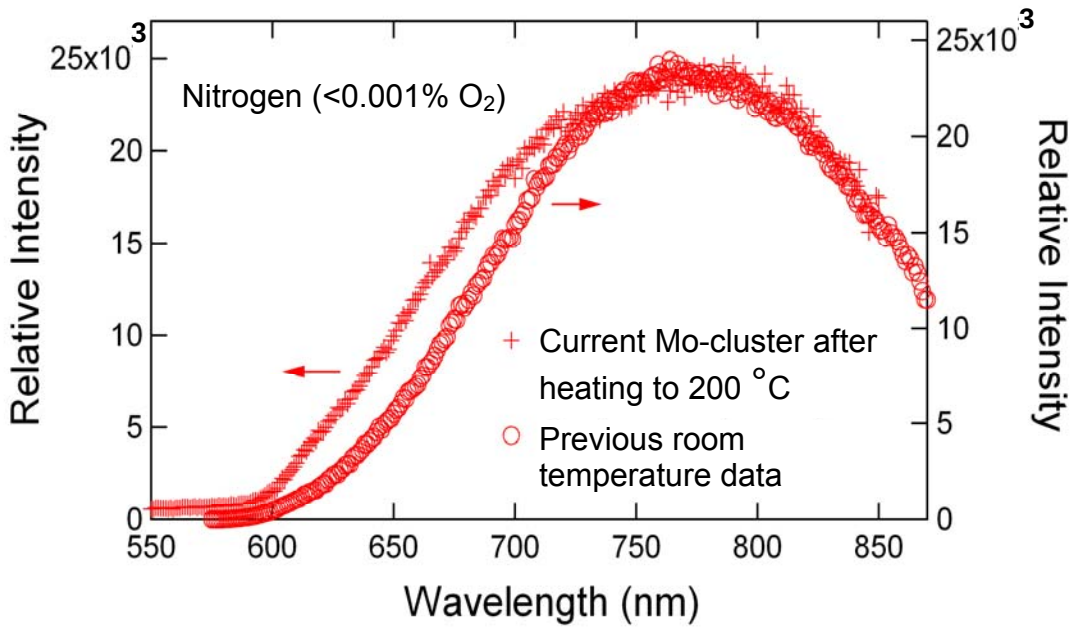

Figure 2.13. Emission spectra from our current Mo cluster compound after thermal cycling to 200°C and previous results from Ghosh et al.[1] Spectra were taken in a nitrogen (<0.001% (v/v) oxygen) environment. The data was obtained by the author in collaboration with R. N. Ghosh. Figure courtesy of R. N. Ghosh.

2.2.2 Immobilization of Mo_6Cl_{12} in sol–gel matrices

Developing a high temperature oxygen fiber sensor based on Mo_6Cl_{12} luminescence quenching requires a scheme for embedding the clusters in a matrix while retaining their unique optical properties. In addition, the matrix must have high oxygen permeability and adhere strongly to the optical fiber. These requirements can be satisfied by using a sol–gel matrix to immobilize the clusters at the tip of high temperature silica fibers, such as a commercially available gold clad silica fiber rated for long term operation up to 750°C.[14] The silanol terminated surface of the fiber ensures excellent adhesion to the matrix and prior work[15] has shown that the oxygen permeability of sol–gel matrices can be tailored by appropriate choice of reaction conditions.

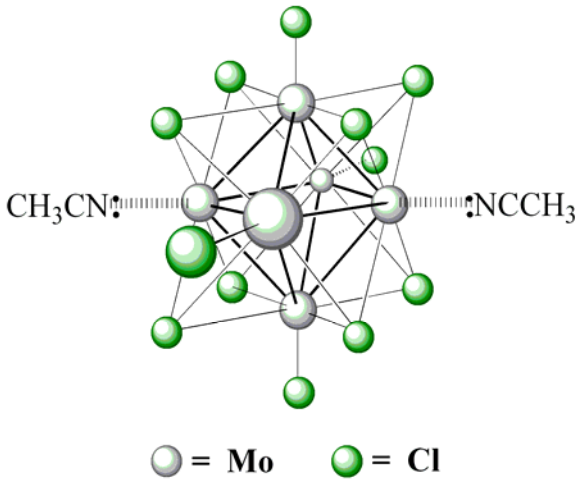

Figure 2.14. Luminescent Mo_6Cl_{12} clusters with acetonitrile bound to the two open coordination sites.

The process for embedding the luminescent clusters must be compatible with the solubility and chemical reactivity of Mo_6Cl_{12}. There are two open coordination sites in the hexanuclear Mo_6Cl_{12} structure (**Figure 2.14**). In the solid state, both sites are occupied by bridging chlorides from adjacent clusters resulting in a polymeric structure. In polar solvents such as ethanol or 6 M HCl, solvent displaces the bridging chlorides and the clusters dissolve to give the monomeric complexes. Since both ethanol and HCl strongly affect sol–gel processing, we used the acetonitrile complex of Mo_6Cl_{12} (Mo_6Cl_{12}•$2CH_3CN$)[16] in sol–gel syntheses since acetonitrile has been used successfully as a co-solvent in sol–gel syntheses. While stirring Mo_6Cl_{12} in acetonitrile for several days eventually yields concentrated orange-yellow solutions of the acetonitrile complex, we found that the complex is more conveniently prepared by loading Mo_6Cl_{12} into the thimble of a Soxhlet extractor and exhaustively extracting with dry acetonitrile.

The use of dry solvent is important as it minimizes formation of less soluble oxygen-bridged complexes.

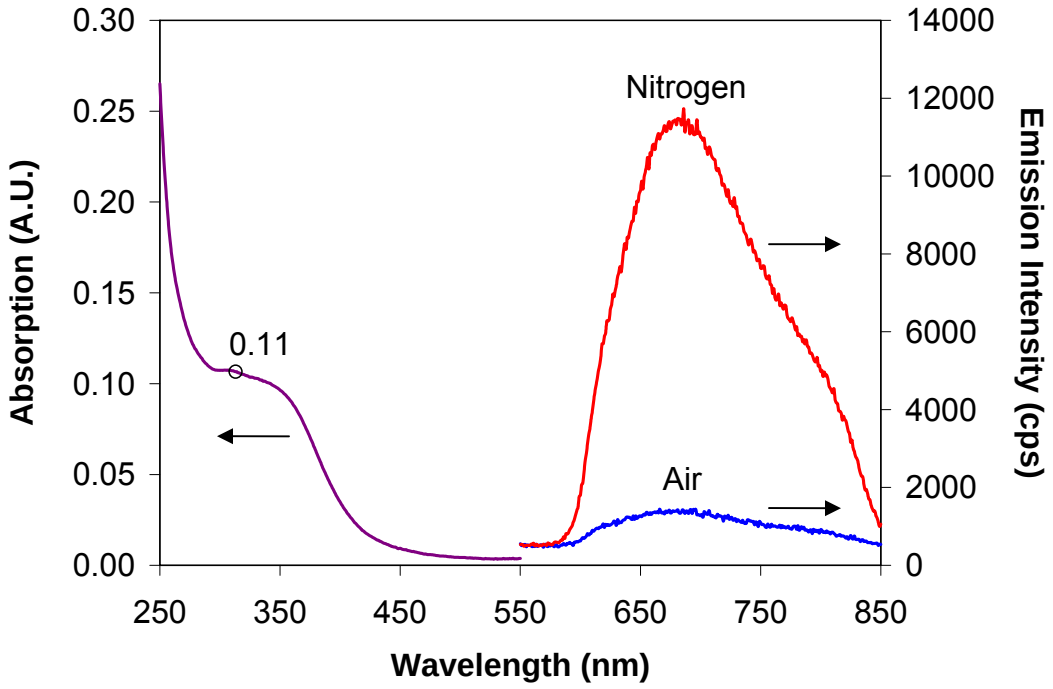

Figure 2.15. Absorbance and emission spectra of the acetonitrile complex of (~5 × 10^{-4} mol/L). The emission is the "uncorrected" raw data, taken with an excitation wavelength of 313 nm. Quenching of ~12× is observed between nitrogen (<0.001% (v/v) oxygen) and air (~20% (v/v) oxygen).

The spectroscopic features of the acetonitrile complex are shown in **Figure 2.15**. Excitation of Mo_6Cl_{12} clusters at wavelengths less than 400 nm leads to a long lived triplet state, which decays to the ground state with emission of red luminescence centered at ~750 nm. The large emission Stokes shift (>400 nm) greatly simplifies the design of a reflection mode fiber sensor since photons over the entire emission band can be collected and the UV excitation light can be removed using simple band pass filters. In addition, the large quantum yield (0.19 at 300K in acetonitrile[17-20] and 0.021 at 300K in the solid state[20]) allows simple sources such as

mercury pen lamps to be used as the UV source. Excitation spectra were obtained by exciting at 313 nm and scanning the emission monochromator from 550 nm to 850 nm. The absorbance of the solutions used for these experiments was adjusted to ~0.1 at 313 nm in order to minimize self-quenching effects. Using reported extinction coefficients for Mo_6Cl_{12} clusters (ε = 3000 L mol^{-1} cm^{-1}),[21] we estimate the solution concentration to be 3×10^{-5} M. A concern is whether the clusters in the matrix exist as isolated species or as aggregates. Having the former is important to avoid decreases in luminescence due to self-quenching. We believe that in solution, Mo_6Cl_{12}•$2CH_3CN$ is monomeric since the emission intensity and quenching behavior of its solutions are comparable to those of molybdenum clusters (e.g. $Mo_6Cl_{14}^{2-}$), which are known to be monomeric. In addition, the emission intensities scale linearly with changes in concentration.

The excited states of Mo_6Cl_{12} clusters are efficiently quenched by oxygen. Spectra for Mo_6Cl_{12}•$2CH_3CN$ solutions measured in room air and under nitrogen are shown in **Figure 2.15**. The data show quenching by a factor of 12, with the emission intensity and line shape returning to their original values upon equilibration with room air. Emission quenching data for Mo_6Cl_{12} clusters typically follows the Stern–Volmer equation,[5] $I/I_0 = 1/(1 + K_{sv}[O_2])$, where I and I_0 are the emission intensity in the presence and absence of oxygen of concentration $[O_2]$ and K_{sv} is the Stern–Volmer constant.[1]

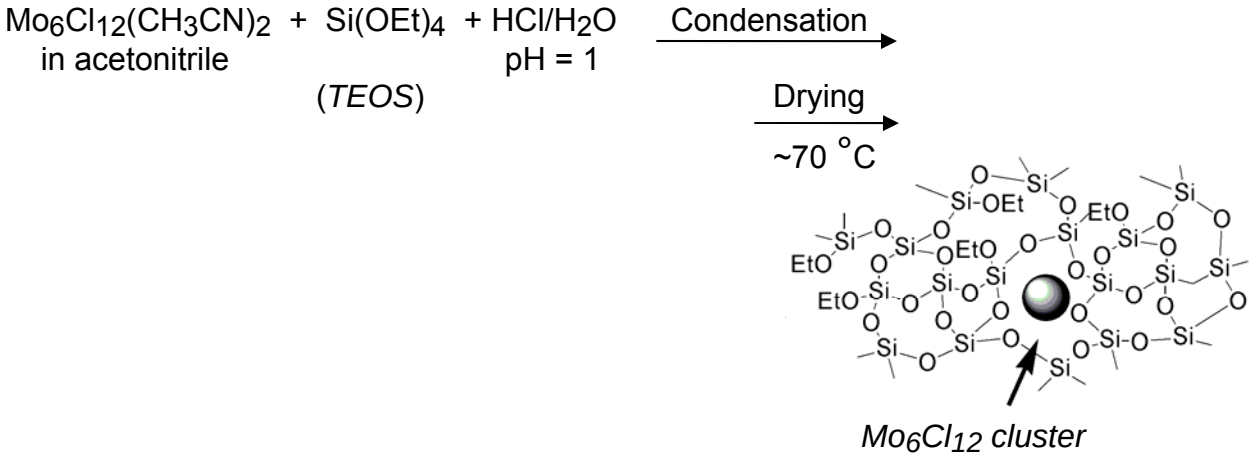

Figure 2.16. Synthetic route to sol–gel immobilized clusters.

The process used to embed the acetonitrile complex in a sol–gel matrix is outlined in **Figure 2.16**. The process is based on the controlled hydrolysis and condensation of tetraethyl orthosilicate where ethoxy groups are lost in the form of ethanol, and new Si-O-Si bonds form to generate the silica matrix. By carrying out the reaction in the presence of the clusters, Mo_6Cl_{12} is entrapped the in the final matrix. Because of its high solubility in the reactants, the acetonitrile complex of Mo_6Cl_{12} is particularly useful for obtaining sol–gel matrices that contain an appreciable concentration of Mo_6Cl_{12}. A requirement is that the sol–gel film be sufficiently porous to allow rapid diffusion of oxygen through the matrix. A series of experiments that lead to sol–gel matrices with different oxygen permeabilities have been reported.[15] Using those conditions as a starting point, we prepared a solution of TEOS, Mo_6Cl_{12}•$2CH_3CN$ dissolved in acetonitrile and aqueous HCl, and then aged the solution at 70°C for 2.5 hours. Since

acetonitrile is known to increase the rates of sol–gel reactions, we monitored the change in the viscosity of the solution and dip-coated clean quartz substrates at regular intervals. Drying at room temperature for ~1 week followed by heating at 70°C for 24 hours gave clear films that adhered strongly to the substrate. These films glow brightly when illuminated with a hand held UV lamp, and the emission line shape of Mo_6Cl_{12}•$2CH_3CN$ embedded in the sol–gel matrix (**Figure 2.17**) matches that of the cluster in CH_3CN.

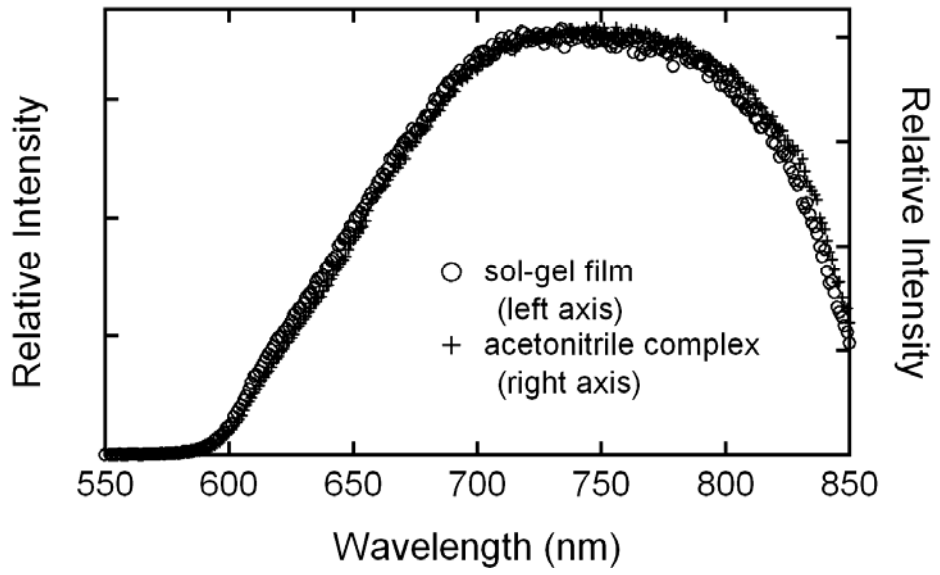

Figure 2.17. Emission spectra of Mo_6Cl_{12}•$2CH_3CN$ demonstrating no change in the cluster line shape between the CH_3CN solution and the sol–gel matrix.[22]

2.3.2 Evaluation of alkali metal salts of Mo_6Cl_{12} for improved thermal stability.

As the synthesis of Mo_6Cl_{12} can be carried out at temperatures >800°C under vacuum, the inherent thermal stability of Mo_6Cl_{12} is high. However, as described earlier, our experiments showed that the canary yellow Mo_6Cl_{12} clusters undergo oxidation in oxygenated environments

at temperatures >250°C to form a gray solid that does not luminesce. Elemental analysis indicates a chemical composition of MoO_x ($3 \leq x \leq 4$), consistent with oxygenation. Two open axial coordination sites on the Mo_6Cl_{12} cluster lead to the polymerization of clusters through shared chlorine bridges. These open sites also are the likely source of the oxidative instability of Mo_6Cl_{12}. The known $M_2Mo_6Cl_{14}$ salts, where M is an alkali metal cation such as Na^+, K^+, or Cs^+ should be more thermally robust since there is a full complement of chloride ligands and no open sites for cluster aggregation or oxidation, i.e. chlorides must be lost from the cluster for the cluster to undergo degradation.[23]

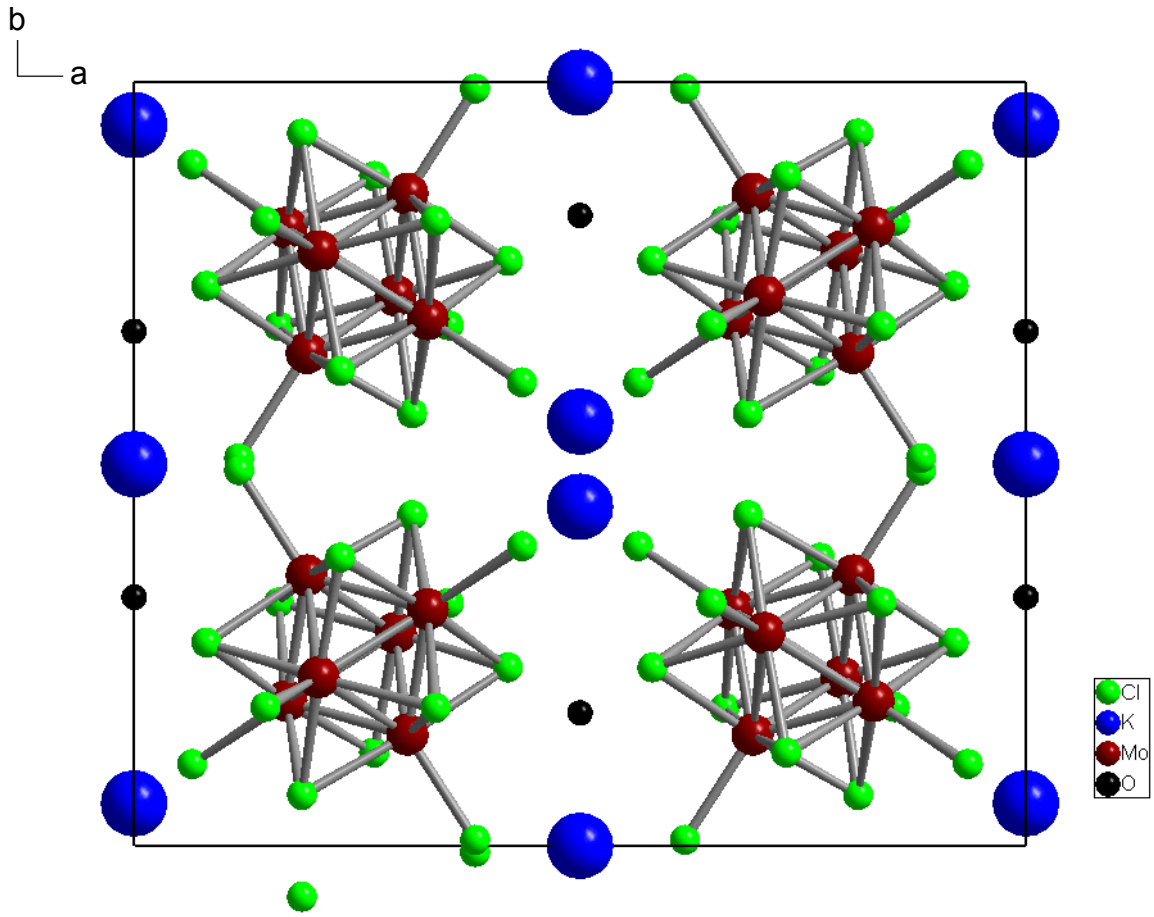

Figure 2.18. A view of the crystal structure of $K_2Mo_6Cl_{14}$•$1H_2O$ viewed down the *c* axis showing the positions of molybdenum, chlorine, potassium, and oxygen. The hydrogen atoms have been removed for clarity.

The K^+ salt shown in **Figure 2.18** was initially synthesized via a high temperature (800°C) metathesis reaction. In addition to being cumbersome, the product contained a substantial amount of impurities. On the advice of Prof Maverick at Louisiana State University, a simple solution-based synthesis was attempted. Mo_6Cl_{12} dissolved in HCl and treated with a large excess of KCl. The $K_2Mo_6Cl_{14}$•$1H_2O$ salt precipitated from solution and was collected by filtration. The K^+ salt was characterized by X-ray powder diffraction, UV-Visible absorption,

and emission spectroscopy. As shown in **Figure 2.19**, the X-ray powder diffraction pattern shows the transformation of the hydrochloride salt to the more stable potassium salt. The optical also data are consistent with successful synthesis of the salt, but the similarity of the optical properties of Mo_6Cl_{12} and the K^+ salt makes it difficult to conclude that there was no contamination by Mo_6Cl_{12}.

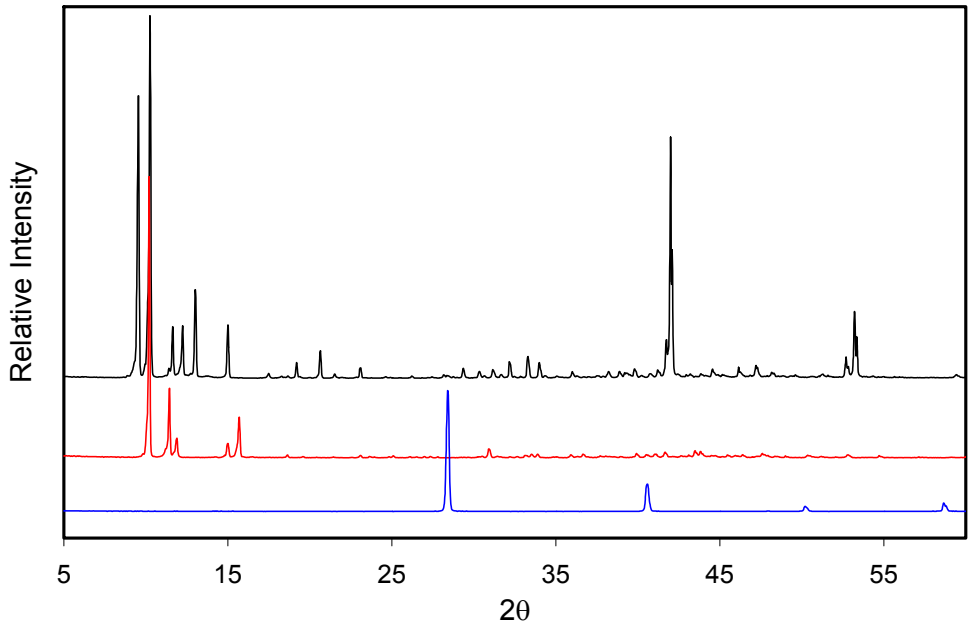

Figure 2.19. X-ray powder diffraction patterns for (top) Mo_6Cl_{12}, (middle) $K_2Mo_6Cl_{14}$•$1H_2O$, and (bottom) KCl.

Thermal analysis of the resulting complex shows improved thermal stability compared to Mo_6Cl_{12}. TGA measurements run in air at 10°C/min (**Figure 2.20**) showed reduced weight losses and, more importantly, after 2 hours at 280°C the samples still luminesced.

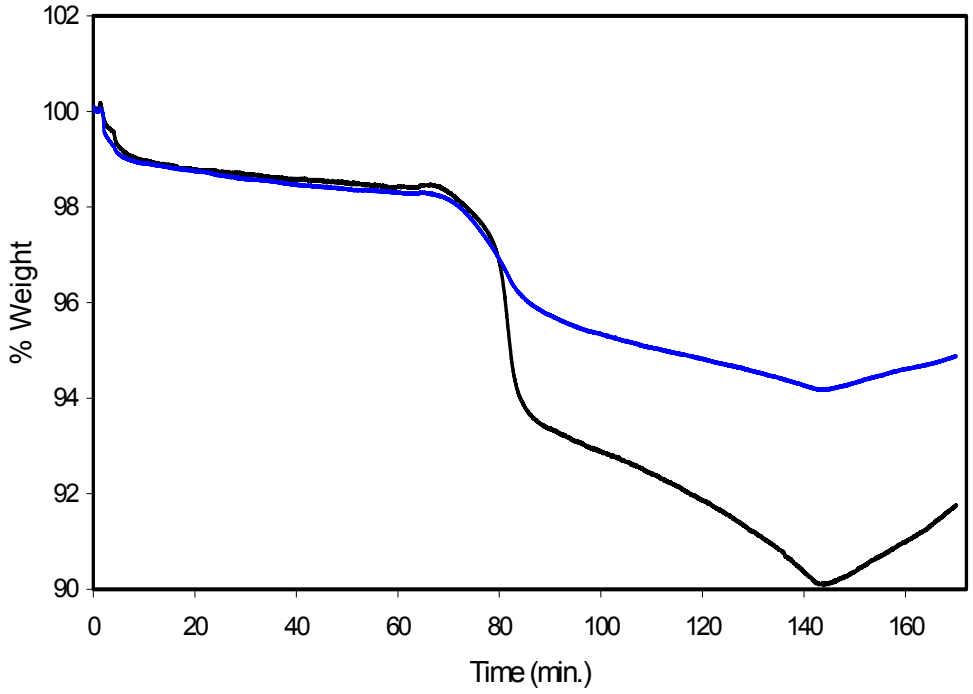

Figure 2.20. Thermal Gravimetric Analysis in air of (—) Mo_6Cl_{12} and (—) $K_2Mo_6Cl_{14}$•$1H_2O$. The samples were (1) heated to 120°C at 30°C/min, (2) held at 120°C for 1 hour, (3) heated to 280°C at 10°C/min, (4) held at 280°C for 1 hour, and (5) cooled to 40°C at 10°C/min.

Mo_6Cl_{12} run under the same conditions were optically dead. The color of the salt complex evolved from yellow to a greenish hue. For reasons noted above, we are unsure whether the color change resulted from partial degradation of the cluster, or is due to contamination by Mo_6Cl_{12}. Mo_6Cl_{12} and its potassium salt, $K_2Mo_6Cl_{14}$•$1H_2O$, were heated to 280°C in air for 1 hour, and after cooling to room temperature, both were dissolved in 6 M HCl. The UV-Visible spectra of the resulting solutions were measured. The data of **Figure 2.21** clearly show the enhanced thermal stability of the potassium salt. The intensity of the $K_2Mo_6Cl_{14}$•$1H_2O$

spectrum is ~2/3 of that for unheated Mo_6Cl_{12} while that for heat treated Mo_6Cl_{12} (run at a 23× higher concentration) shows none of the characteristics of the original complex.

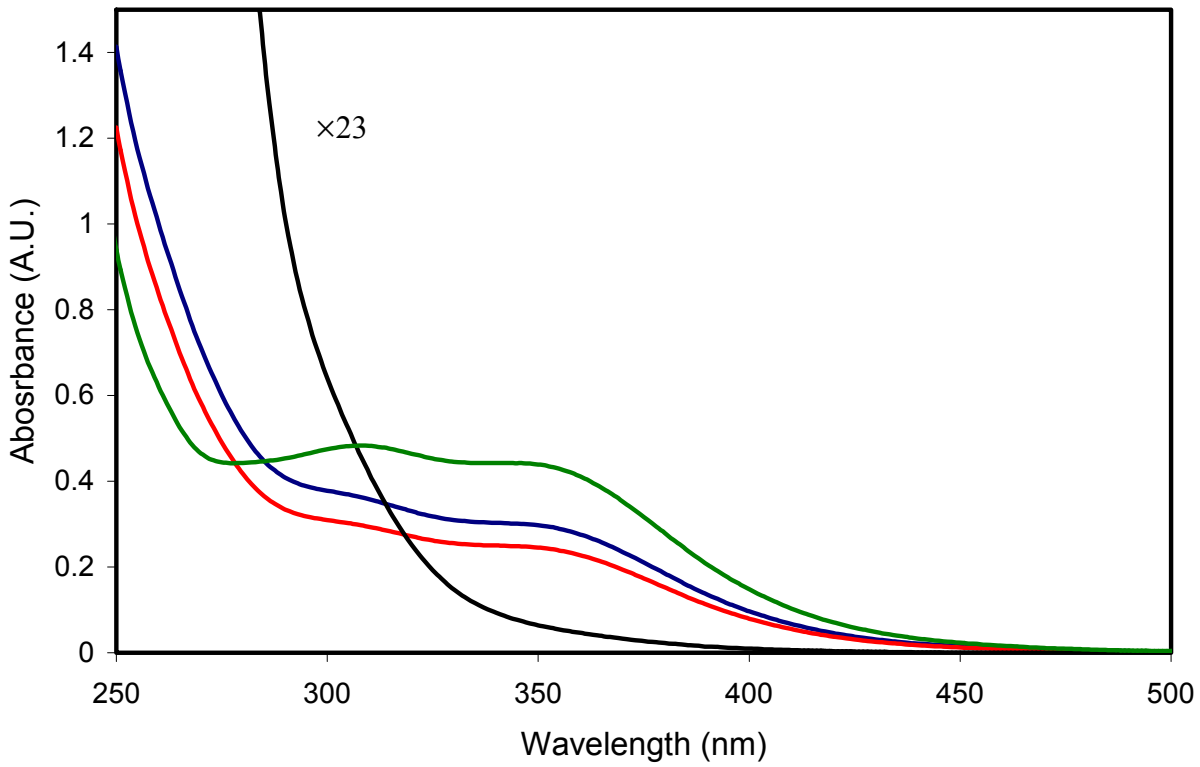

Figure 2.21. Absorption spectra for cluster samples heated at 280°C for 60 minutes and then dissolved in 6 M HCl. Samples shown are (—) $K_2Mo_6Cl_{14}$•$1H_2O$, heated in air in the TGA apparatus and (—)in a microscope hot stage, (—) Mo_6Cl_{12} heated in a hot stage, and (—) unheated Mo_6Cl_{12}. The concentrations of the solutions were 0.17 g/L, except for the heated Mo_6Cl_{12} sample, which was 23 times higher (4 g/L).

The previous data show that $K_2Mo_6Cl_{14}$•$1H_2O$ has superior thermal stability compared to Mo_6Cl_{12}. Two analytical tests were devised for qualifying new syntheses of $K_2Mo_6Cl_{14}$•$1H_2O$, isothermal aging in air at 280°C, and measuring the optical properties before and after thermal aging. The potassium salt shows at most a few percent weight loss during four hours of

isothermal aging, but samples contaminated with Mo_6Cl_{12} degrade significantly and lose substantial weight early in the analysis. Two large scale batches of the potassium salt, **MM-7** and **MM-8**, were prepared and aged isothermally in air using TGA. As shown in **Figure 2.22,** their thermal degradation profiles are nearly identical to **FJ-17**, one of the first syntheses of $K_2Mo_6Cl_{14}•1H_2O$. The profile of **MM-5**, prepared at approximately the same time as **FJ-17**, shows a significant weight loss early in the run, and we conclude from its similarities to the weight loss profile of Mo_6Cl_{12} that **MM-5** is contaminated by the less stable Mo_6Cl_{12}.

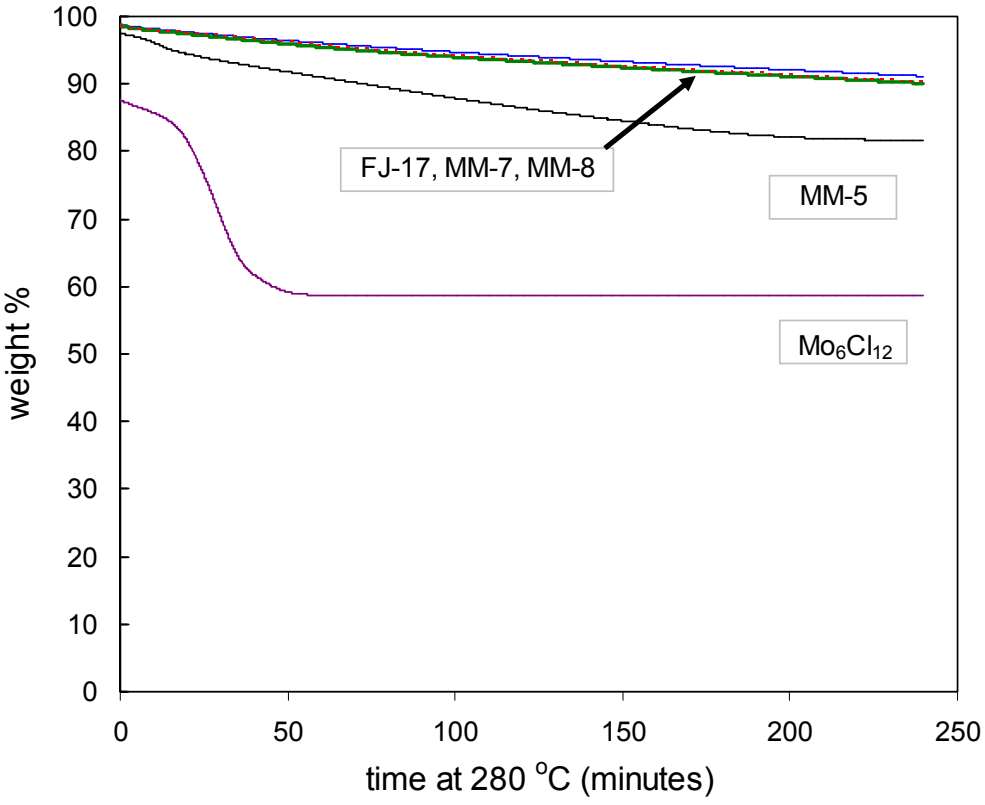

Figure 2.22. Isothermal aging tests of four preparations of $K_2Mo_6Cl_{14}•1H_2O$ (**FJ-17**, **MM-5**, **MM-7**, and **MM-8** at 280°C in air, showing the consistent thermal profiles of recently prepared batches of $K_2Mo_6Cl_{14}•1H_2O$. The corresponding data for $(H_3O)_2Mo_6Cl_{14}•6H_2O$ are shown for comparison.

While characterizing the weight loss profile of a candidate salt is a rapid assay for the purity of the salt, a more rigorous test is measurement of the optical properties of the lumophore. Solutions of **MM-7**, **MM-8**, and **FJ-17** were prepared in acetonitrile and their luminescent properties were measured. Data measured at room temperature shown in **Figure 2.23**, demonstrate that both the line shape and luminescence intensity of for all three samples are nearly identical and are consistent with the notion that the lumophores in **FJ-17**, **MM-7** and **MM-8** are identical. Samples of the same salts were then heated to 200°C for four hours, cooled to room temperature, and again solutions of the salts in acetonitrile were prepared and their luminescent properties were measured.

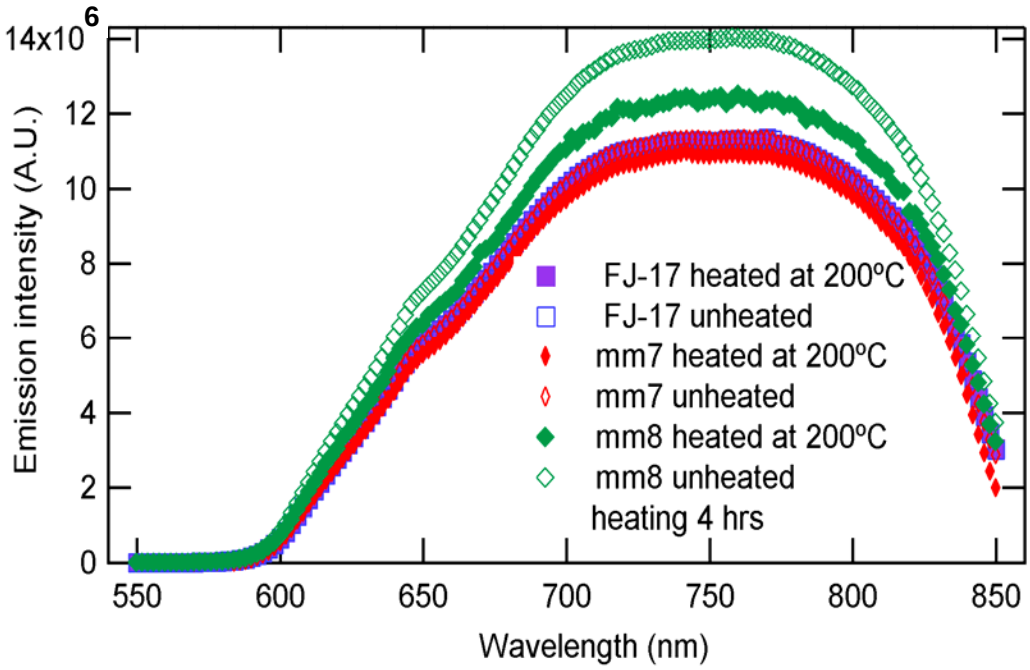

Figure 2.23. A comparison of the emission spectra from three different preparations of $K_2Mo_6Cl_{14}$•$1H_2O$, **FJ-17**, **MM-7**, and **MM-8**. Data are shown for as-prepared samples, as well as samples that have been heated to 200°C for 4 hours, illustrating that both lineshape and intensity are conserved. Solution concentrations: **MM-8**: 0.118 mM ± 1.4% and 0.115 mM ± 1.4% after heating; **MM-7**: 0.0959 mM ± 1.4%, and **FJ-17:** 0.087 mM ± 1.4%. Within the error bars of the measurement the emission intensity scales with concentration. The data was obtained by the author in collaboration with R. N. Ghosh. Figure courtesy of R. N. Ghosh.

The results again are consistent with the conclusion from the isothermal aging experiments, that the clusters from all three batches are identical. Note that the as expected the emission intensity scales linearly with cluster concentration. While the data presented above emphasize the similarity of the three different batches of potassium salt, UV-Visible data suggest that there may be a silent impurity present in all three samples. UV-Visible spectra were taken of the three salts as solutions in acetonitrile. As shown in **Figure 2.24** the spectra have similar but not identical line shapes.

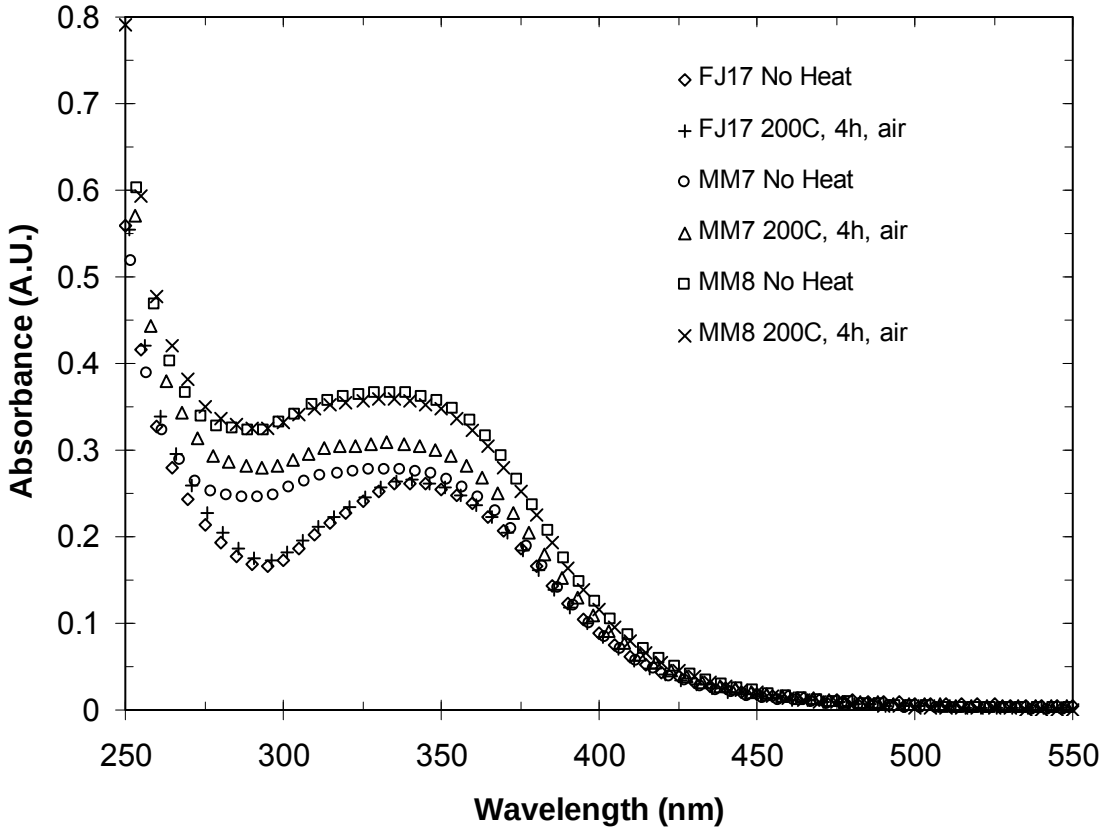

Figure 2.24. Absorption spectra from three different preparations of $K_2Mo_6Cl_{14}$•$1H_2O$, FJ-17, MM-7, and MM-8. Data are shown for as-prepared samples, as well as samples that have been heated to 200°C for 4 hours. The intensity of the "excess" absorption centered at 300 nm correlates with the age of the solutions. Solution concentrations: **MM-8**: 0.118 mM ± 1.4% and 0.115 mM ± 1.4% after heating; **MM-7**: 0.0959 mM ± 1.4%, and **FJ-17** 0.087 mM ± 1.4%.

While the low energy side of the absorption envelope (>350 nm) for all three salts appear to be identical, the spectra of the three salts differ at shorter wavelengths. The data suggest an additional absorbance feature centered at 300 nm for **MM-7** and **MM-8**. Additional experiments on **FJ-17** confirms that this feature is present in all three samples, and its intensity is related to the age of the solution. Since the absorption envelope for λ >350 nm remains unchanged in intensity and shape as the 300 nm grows in, we speculate that the increase in absorption at 300 nm is due to a nanoparticulate impurity that is not removed by filtration during purification of the salts. When dispersed in acetonitrile, the impurity apparently dissolves to give a soluble Mo complex with an absorption peak at 300 nm. Since the luminescence spectra do not show the same effect (**Figure 2.25**), the impurity is apparently non-luminescent and does not interfere with the luminescence quenching of $K_2Mo_6Cl_{14}$•$1H_2O$.

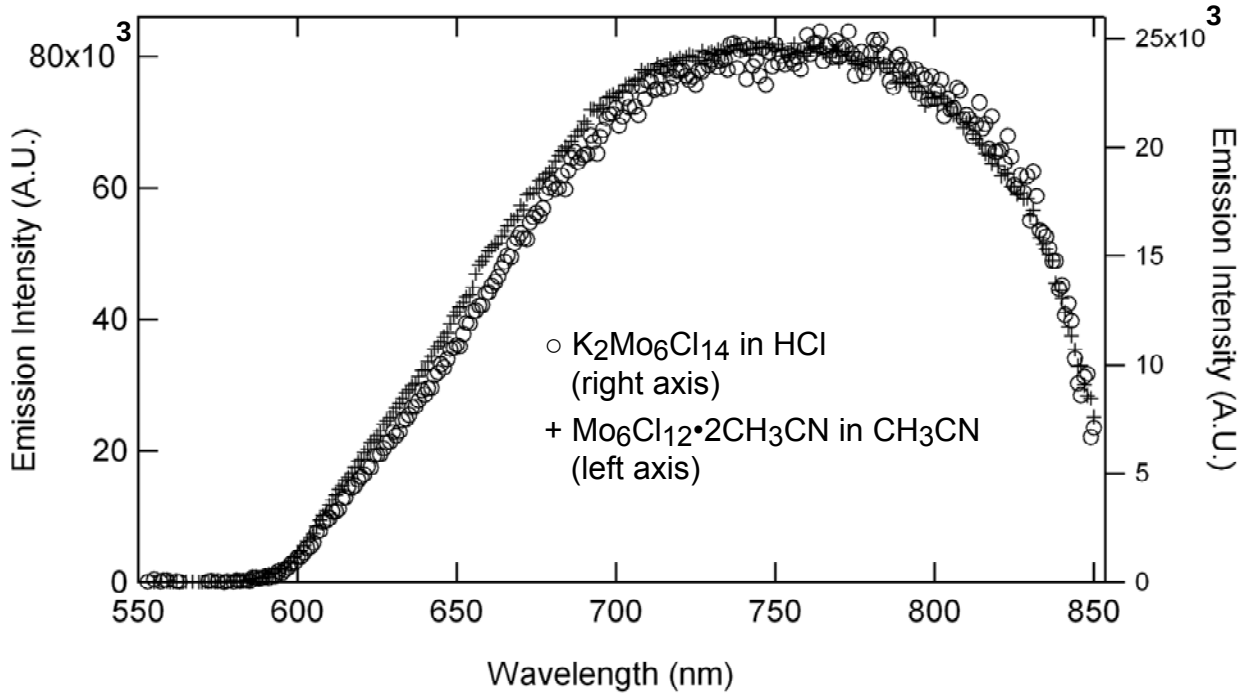

Figure 2.25. Emission spectra in nitrogen (<0.001% (v/v) oxygen) of (a) $K_2Mo_6Cl_{14}$•$1H_2O$ and (b) Mo_6Cl_{12}•$2CH_3CN$ in CH_3CN, demonstrating that the cluster photophysics is not affected by ligand substitution. Note that the potassium salt has been heat cycled to 280°C for one hour. The data was obtained by the author in collaboration with R. N. Ghosh. Figure courtesy of R. N. Ghosh.

2.4 CONCLUSIONS

A study of the high temperature stability of the Mo_6Cl_{12} clusters in oxygenated environments revealed irreversible changes in the optical absorption spectrum at T >250°C and a loss of the red luminescence that is characteristic of pristine clusters. Thermal aging experiments run in air and under nitrogen point to oxidation of the clusters as the cause of the change in optical properties. X-ray powder diffraction measurements on samples annealed at 300°C under

controlled conditions are consistent with oxidation of Mo_6Cl_{12} to form MoO_3 as the principal degradation product. Two open axial coordination sites on the Mo_6Cl_{12} cluster lead to the polymerization of clusters through shared chlorine bridges. These open sites also are the likely source of the oxidative instability of Mo_6Cl_{12}. The known $M_2Mo_6Cl_{14}$ salts, where M is an alkali metal cation such as Na^+, K^+, or Cs^+ should be more thermally robust since there is a full complement of chloride ligands and no open sites for cluster aggregation or oxidation, i.e. chlorides must be lost from the cluster for the cluster to undergo degradation.

The potassium salt of Mo_6Cl_{12} ($K_2Mo_6Cl_{14}$•$1H_2O$) was synthesized and it was found that the alkali salts of Mo_6Cl_{12} are more stable that the parent compound. Optical and thermal aging experiments show that the alkali metal salts of Mo_6Cl_{12} have higher thermal stabilities and remain luminescent after long-term aging at 280°C.

REFERENCES

REFERENCES

[1] R. N. Ghosh, G. L. Baker, C. Ruud, D. G. Nocera, *Applied Physics Letters* **1999**, *75*, 2885.

[2] N. Prokopuk, D. F. Shriver, in *Advances in Inorganic Chemistry, Vol. 46*, Academic Press Inc., San Diego, CA, **1999**, 1.

[3] H. Schaefer, H. G. v. Schnering, J. Tillack, F. Kuhnen, H. Worle, H. Z. Baumann, *Zeitschrift fuer Anorganische und Allgemeine Chemie* **1967**, *353*, 281.

[4] T. C. Zietlow, M. D. Hopkins, H. B. Gray, *Journal of Solid State Chemistry* **1985**, *57*, 112.

[5] O. Stern, M. Volmer, *Physikalische Zeitschrift* **1919**, *20*, 183.

[6] J. C. Sheldon, *Journal of the Chemical Society* **1960**, 1007.

[7] D. N. T. Hay, J. A. Adams, J. Carpenter, S. L. DeVries, J. Domyancich, B. Dumser, S. Goldsmith, M. A. Kruse, A. Leone, F. Moussavi-Harami, J. A. O'Brien, J. R. Pfaffly, M. Sylves, P. Taravati, J. L. Thomas, B. Tiernan, L. Messerle, *Inorganica Chimica Acta* **2004**, *357*, 644.

[8] A. I. Busev, *Analytical chemistry of molybdenum*, Ann Arbor-Humphrey Science Pub., **1969**.

[9] International Centre for Diffraction Data, *Powder Diffraction File #01-074-0480*, **2005**.

[10] W. C. Dorman, R. E. McCarley, *Inorganic Chemistry* **1974**, *13*, 491.

[11] R. D. Mussell, Ph. D. Dissertation, Michigan State University (East Lansing), **1988**.

[12] *SMART, SAINT, and SHELXTL V-5*, Bruker Analytical X-ray Systems, Inc.: Madison, WI **1998**.

[13] H.-H. Perkampus, *Encyclopedia of spectroscopy*, English ed. ed., VCH, Weinheim, Germany ;, **1995**.

[14] Fiberguide, in *Fiberguide Specification sheet for Superguide G ultraviolet-visible fiber with gold jacket*, Fiberguide Industries, Stirling, NJ, Website.

[15] C. McDonagh, P. Bowe, K. Mongey, B. D. MacCraith, *Journal of Non-Crystalline Solids* **2002**, *306*, 138.

[16] G. M. Ehrlich, C. J. Warren, R. C. Haushalter, F. J. Disalvo, *Inorganic Chemistry* **1995**, *34*, 4284.

[17] A. W. Maverick, H. B. Gray, *Journal of the American Chemical Society* **1981**, *103*, 1298.

[18] A. W. Maverick, J. S. Najdzionek, D. Mackenzie, D. G. Nocera, H. B. Gray, *Journal of the American Chemical Society* **1983**, *105*, 1878.

[19] A. W. Maverick, Ph.D. Dissertation, California Institute of Technology (United States -- California), **1982**.

[20] M. D. Newsham, Doctoral Dissertation, Michigan State University (East Lansing), **1988**.

[21] J. C. Sheldon, *Nature* **1959**, *184*, 1210.

[22] D. J. Osborn III, G. L. Baker, R. N. Ghosh, *Journal of Sol-Gel Science and Technology* **2005**, *36*, 5.

[23] J. C. Sheldon, *Journal of the Chemical Society* **1962**, 410.

Chapter 3 – Sensor support-matrix development and characterization

3.1 INTRODUCTION

Maximizing the efficiency of the combustion process requires real-time control of the correct fuel/oxygen ratio.[1] This requires the ability to sense oxygen levels over a broad range of concentrations with fast response times and under rapidly varying conditions of pressure and temperature. Maverick,[2] Mussell,[3] Newsham,[4] and Ruud[5] previously reported preliminary studies of the synthesis and optical properties of Mo_6Cl_{12}-based clusters that are relevant to this project. In particular, Newsham describes the properties of neutral Mo_6Cl_{12} clusters and their salts in a sol–gel matrix.[6] Newsham's data indicate that the photophysical properties of the clusters are maintained in sol–gel matrices. To prepare a fiber optic oxygen sensor based on Mo_6Cl_{12}, Ruud dispersed Mo_6Cl_{12} in poly[1-trimethylsilyl-1-propyne] (PTMSP), and used a dipping technique to immobilize the composite at the cleaved end of a silica optical fiber. Ghosh and co-workers demonstrated a fast room temperature fiber optic sensor based on oxygen quenching of the luminescence from the PTMSP/Mo_6Cl_{12} composites.[7] The nature of the signal determined from this sensor is luminescence intensity that is proportional to partial pressure of O_2, as determined in chapter 2. Plotted in **Figure 3.1** is the output signal from the sensor as a function of oxygen concentration from 0–20% oxygen, with nitrogen as the balance gas. Note from the error bars within the 6 Hz measurement bandwidth the relative standard deviation is less than 2% of the signal. The data demonstrate that the sensor can clearly resolve

changes of 0.1% (v/v) oxygen concentration in the 0–1% (v/v) range, changes of 0.5% (v/v) oxygen concentration in the 1–4% (v/v) range, changes of 1% (v/v) oxygen concentration in the 4–10% (v/v) range, and changes of 2% (v/v) oxygen concentration in the 10–20% (v/v) range. These measurements were made on a 1.5 m long fiber probe. The auto-fluorescence is small for this long length of fiber, demonstrating the feasibility of probing remote locations with such a fiber sensor. From the inset to **Figure 3.1** it appears that an upper bound to the sensor switching time is 30 seconds. This is not the intrinsic response time of the sensor, which is estimated to be 1 second. In addition it was demonstrated[7] that the quenching of the cluster luminescence shown in **Figure 3.1**, obeys the Stern–Volmer equation as expected from theory.[8]

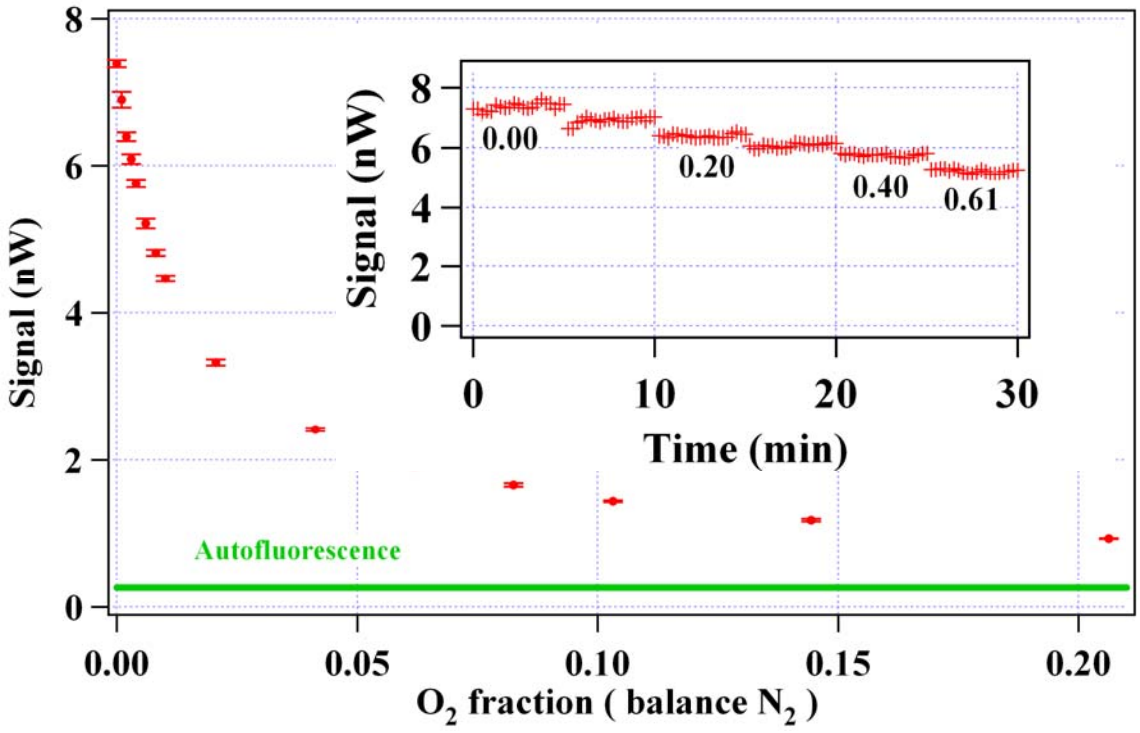

Figure 3.1. Output signal from the room temperature fiber oxygen probe as a function of volume % oxygen.[7] The sensor signal as a function of time for low oxygen concentrations is shown in the inset.

While the PTMSP support is adequate for room temperature applications, is unable to withstand the temperatures associated with combustion in a power plant.[9, 10] To modify the sensor for high-temperature applications, PTMSP can be replaced with a thermally stable sol–gel matrix that will withstand the higher temperature requirements of the power plant combustion process. The idea of using a sol–gel as the support matrix for a high-temperature oxygen sensor application is not new. Remillard and coworkers have shown that a sol–gel supported copper based oxygen sensor can be used in a combustion process.[11] However, Remillard's sensor relies on the oxidation and reduction of copper.[12] By developing a sensor that is based on luminescence, we can avoid the need for a procedure that regenerates the oxygen sensitive probe.

3.2 EXPERIMENTAL

3.2.1 Materials.

Ethanol (Koptec, anhydrous, USP), 2-propanol (Mallinckrodt, AR (ACS)), methanol (VWR), dichloromethane (Mallinckrodt, AR (ACS)), chloroform (Mallinckrodt, AR (ACS)), toluene (Mallinckrodt, AR (ACS)), and hexanes (Mallinckrodt, AR (ACS)), hydrochloric acid (Columbus Chemical Industries, electronics grade) were used as received. Acetonitrile (Spectrum Chemical Company, HPLC grade and EMD Chemicals, OmniSolv) were dried overnight using activated molecular sieves (Spectrum Chemical, 1/16" pellets, type 4 Å) and then distilled from CaH_2 (Spectrum Chemical, anhydrous, desiccant, 40–20 mesh) prior to use. Ethanol (95%) was prepared by addition of Milli-Q water to absolute ethanol. Water used was either reverse osmosis (in-house) or deionized using a Millipore purification system (Milli-Q, 18

MΩcm). $MoCl_2$ was obtained from Cerac (lot 172938-A-1) or City Chemical (lots 40C65, 40M21, and 30L114). Anhydrous $MoCl_5$ (Strem, 99.6%, lot B035113), Bi powder (Strem, 99.9%, lot B7709023), potassium chloride crystals (Spectrum Chemical, Reagent A.C.S., lot QE7300) or (Columbus Chemical Industries, ACS grade, crystals), phenolphthalein (Spectrum Chemical, powder, Reagent A.C.S., lot LM0200), sodium hydroxide pellets (Mallinckrodt, AR (ACS), lot C41P01), potassium hydroxide pellets (Jade Scientific, ACS Reagent), concentrated sulfuric acid (Fisher Scientific, Reagent grade and (Columbus Chemical Industries, ACS/Reagent grade), hydrofluoric acid (JT Baker, technical grade, 47.0–52.0%, lot J22906), glacial acetic acid (Fisher Scientific certified ACS Plus, lot 993730), H_2O_2 (Fisher, 30%), 8-hydroxyquinoline (Sigma-Aldrich, 99+%), and tetrabutylammonium chloride (Fluka, purum, ≥97% (Cl), lot 1327989) were used as received. Holmium(III) oxide, Ho_2O_3, (Aldrich, 99.999%) was used as received. Potassium dichromate, $K_2Cr_2O_7$, (Mallinckrodt, Analytical Reagent (AR), lot KTCA) was recrystallized 2× using reverse osmosis water. Medium-fast filter paper (Whatman, 150 mm diameter circles, #1 qualitative) or (Whatman, 185 mm diameter circles, #1 qualitative), borosilicate microfiber filters (Micro Filtration Systems, GD120 grade, 47 mm diameter), 350-mL fritted funnel (Pyrex, ASTM 10-15 M), 350-mL fritted funnel (Kimax, 80 C), 350-mL fritted funnel (ACE Glass, POR A, ASTM 145-175), 60-mL fritted funnel (ChemGlass, medium porosity), cellulose extraction thimble (Whatman Inc., 33 × 94 mm, single thickness), and syringe filters (Whatman Inc., 4 μm pore size) were used as received. All glassware used for spectroscopic measurements was cleaned by soaking in concentrated hydrochloric acid, scrubbed with water and Alconox soap, rinsed with reverse osmosis water, and then oven dried prior to use. Tetraethyl orthosilicate (TEOS) (Aldrich, 99.999%), *n*-

octyltrimethoxysilane (OtMOS) (Aldrich, 96%), *n*-propyltrimethoxysilane (PtMOS) (Gelest, 98%), octyltriethoxysilane (OtEOS) (Aldrich, ≥96%), and (3,3,3-trifluoropropyl)-trimethoxysilane (TFP-tMOS) (Gelest, >95%) were used as received. Corning 7980 quartz microscope slides (7.62 cm × 2.54 cm × 0.1 cm) were obtained from Technical Glass Products and were cut into 1.27 cm × 2.54 cm pieces. Slides were handled with gloves and tweezers in order to minimize surface contamination and then washed with Alconox, rinsed with distilled water, soaked in a base bath (~5M NaOH in 95% ethanol), rinsed with distilled water, and stored in distilled water until use. Fibers were purchased from 3M (FP-1.0-UHT) and Ceramoptec (PUV 1000/1300N), and were handled with gloves in order to minimize surface contamination.

3.2.2 Preparation of the acetonitrile complex of Mo_6Cl_{12}. (Mo_6Cl_{12}•$2CH_3CN$)

All glassware and solvents were dried prior to use. The Mo_6Cl_{12} hydrochloride salt was heated under vacuum at 210°C for 12 hours to yield Mo_6Cl_{12}. The resulting yellow powder was loaded into the thimble of a pre-dried Soxhlet extraction apparatus. Dry acetonitrile (250 mL) was added to the extractor and the receiving flask was heated to start the extraction process. After 3 days, the yellow solution was removed and concentrated to 10 mL. The products were characterized using UV-visible and emission spectroscopy.

3.2.3 Preparation of sol–gel solutions containing Mo_6Cl_{12}•$2CH_3CN$.

A typical stock solution for the coating process was prepared as described below. The acetonitrile complex (1.4 mL, 7 mmol) was added with stirring to TEOS (2.0 mL, 9.0 mmol) in a 10 mL Erlenmeyer flask. Water (0.65 mL, adjusted to pH=1 with HCl) was added and the

solution was stirred for 1 hour at room temperature. The stir bar was removed from the flask and the solution was heated in an oil bath at 70°C for 2.5 hours. The solution was then transferred to a 20 mL glass scintillation vial, capped, and aged at room temperature until use.

3.2.4 Preparation of sol–gel solutions containing $K_2Mo_6Cl_{14}$ clusters.

A typical TEOS-based sol–gel binder solution was prepared by adding TEOS (100 mL, 0.477 mol) and acetonitrile (70.3 mL) to a 500 mL Erlenmeyer flask. With stirring, water (32.3 mL, adjusted to pH = 1 with HCl) was added and the solution was stirred for 1 hour at room temperature. The stir bar was removed from the flask and the solution was heated in an oil bath at 70°C for 2.5 hours. The solution was then transferred to a 500 mL glass bottle, capped, and aged at room temperature until use. Approximately three days before dipping the slides, 25.5 mg of $K_2Mo_6Cl_{14}\cdot 1H_2O$ was added to a scintillation vial containing 10 mL of the stock TEOS-based sol–gel solution and stirred for three days to ensure complete dissolution of the complex.

3.2.5 Synthesis of cluster-containing sol–gel particulates.

Sol–gel solutions **29**, **31**, and **34g-o** containing $K_2Mo_6Cl_{14}$ were prepared as described in chapter 3 then aged in sealed scintillation vials for 4–7 months at room temperature to form solid monoliths. The monoliths were ground using a mortar and pestle (abbreviated mp) and then cured at 70°C for 5 days to complete the sol–gel reaction and minimize further densification of the sol–gel matrix to produce the larger (~250 μm) **mp29**, **mp31**, and **mp34g-o** particles. Pulverizing **mp29** and **mp34g-o** for 15minutes using a small stainless steel Wig-L-Bug ball mill (abbreviated wlb) from Bratt Tech, Inc. produced the smaller (1 – 8 μm) **wlb29** and **wlb34g-o**

particles. The initial $K_2Mo_6Cl_{14}$ concentration of sol–gel solutions used to prepare **mp31**, **wlb29**, and **wlb34g-o** particulates was 8.6×10^{-3} M, 2.2×10^{-3} M, 2.3×10^{-3} M respectively.

3.2.6 Synthesis of 55 mol% OtMOS/TEOS sol–gel solution.

The preparation of a typical 55 mol% OtMOS/TEOS sol–gel binder solution is described below. A stock solution of 55 mol% OtMOS in 45 mol% TEOS was prepared by mixing 10.20 mL of OtMOS and 7.30 mL of TEOS while stirring. The solution was then stored in a brown glass bottle with a Teflon-lined cap until needed. The OtMOS/TEOS mixture (1.75 mL) and co-solvent (see below) were added to a 20 mL scintillation vial, which was then capped and stirred until clear. Once the solution became clear, 0.40 mL of 0.1 M HCl was added. After recapping the vial, the solution was stirred at room temperature until clear (~15 minutes). The solution was diluted 1:1 v/v with additional co-solvent to decrease the viscosity of the solution, and aged at room temperature until used. For binder solutions with acetonitrile as the co-solvent, dry acetonitrile (1.70 mL, 0.352 mol) was added. For binder solutions using ethanol as the co-solvent (1.80 mL, 0.352 mol) was added.

3.2.7 Synthesis of 50 mol% OtEOS/TEOS sol–gel solution.

The preparation of a typical 50 mol% OtEOS/TEOS sol–gel binder solution is described below. A stock solution of 50 mol% OtEOS in TEOS was prepared by adding 10.20 mL of OtEOS to 7.30 mL of TEOS with stirring. The solution was then stored in a brown glass bottle with a Teflon-lined cap until needed The OtEOS/TEOS mixture (1.75 mL) and co-solvent (see below) were added to a 20 mL scintillation vial, capped, and then stirred until clear. Once the solution became clear, 0.40 mL of 0.1 M HCl was added. The vial was recapped and the solution was

stirred at room temperature until clear (~15 minutes). To decrease the viscosity, the solution was diluted with an additional portion of co-solvent (1:1 v/v) and then the solution was aged at room temperature until used. For binder solutions with acetonitrile as the co-solvent, dry acetonitrile (1.70 mL, 0.352 mol) was added. For binder solutions using ethanol as the co-solvent (1.80 mL, 0.352 mol) was added.

3.2.8 Synthesis of 67 mol% TFP-tMOS/PtMOS sol–gel solution.

The preparation of a typical 67 mol% TFP-tMOS/PtMOS sol–gel binder solution is described below. A stock solution of 67 mol% TFP-tMOS in PtMOS was prepared by mixing TFP-TMOS (3.00 mL, 156.7 mmol) and PtMOS (1.40 mL, 79.3 mmol) while stirring. The solution was then stored in a brown glass bottle with a Teflon®-lined cap until needed. A 4.40 mL portion of stock solution, 1.30 mL of deionized water, HCl (0.15 mL, 0.1 M), and the co-solvent (see below) were added to a 20 mL scintillation vial, capped, and stirred until clear. The solution was then sonicated for 1 hour while capped. For binder solutions with acetonitrile as the co-solvent, dry acetonitrile (2.70 mL, 51.7 mmol) was added. For binder solutions using ethanol as the co-solvent (3.00 mL, 51.4 mmol) was added.

3.2.9 Preparation of composite powders for composite blends.

A previously prepared cluster-containing sol–gel solution was aged at room temperature for 4 months in a sealed vial to obtain a solid monolith. The monolith was then ground by hand to a powder with particle sizes ranging from 25 μm – 250 μm using a mortar and pestle. The powder was then cured for 24 hours at 70°C to drive the sol–gel reactions toward completion. Blends of 30, 50, 60, and 80 w/w% were prepared by adding a known mass of stock sol–gel solution to a

predetermined mass of the composite powder to obtain a light yellow suspension that was then mixed with gentle grinding in a small vial to maximize homogeneity.

A control for fiber sensor analysis was prepared from a stock sol–gel solution without added cluster. After aging at room temperature for 4 months in a sealed vial, the solid monolith was ground using a mortar and pestle to a powder with particle sizes ranging from 25 μm – 250 μm. The powder was cured for 24 hours at 70°C to drive the sol–gel reactions toward completion and then was pulverized for 15 minutes in a Wig-L-Bug (a small ball mill) to obtain a white powder with 1–2 μm diameter particles.

3.2.10 General procedure for dip coating glass or quartz planar substrates.

Slides were handled while wearing Supreno SE™ brand powder free nitrile gloves. The slides were washed with Alconox™, rinsed with distilled water, soaked in a base bath for ~6 hours, rinsed with distilled water, and soaked in distilled water. Just prior to use, each slide was dried using a stream of house nitrogen and then immediately coated by dipping the slide into the sol–gel solution at a rate of approximately 1 mm/sec. For most slides, one surface was masked using a piece of Scotch Magic™ tape to limit the sol–gel coating to one side of the substrate. The sol–gel solution vial was re-capped after each dip coat. Once coated, the slides were either (1) placed flat on a piece of aluminum foil and then placed into an oven at 70°C for 24 hours to cure or (2) placed in a capped 20 mL vial laying on its side. The evaporation rate was controlled by how tightly the vial was sealed. Slow evaporation rates gave films with better adhesion and fewer cracks. When dry, the films were thermally cured in an oven in air at 70°C for 1 to 24

hours, depending on the sample. A few slides were prepared using slight modifications of the above scheme. In some cases, the number of coatings and times between coats were varied.

A simple dip coater was built to better control the uniformity of coated slides, especially at low dipping rates (~1 mm/sec). Slides were clamped in the dip coater, dipped with no hold time and placed directly into a 20-mL scintillation vial and handled as described above. A dip rate of 1 to 1.6 mm/sec gave good quality films. Loss of ethanol during dipping significantly changed the viscosity of the sol–gel solution. Adding ethanol to compensate for losses increased the lifetime of the solution.

3.2.11 General procedure for dip coating fibers.

Approximately 1 cm of jacket and cladding were mechanically removed to expose the fiber core. The exposed core was wiped with an acetone-soaked Kimwipe to remove residual cladding material and the tip was suspended in stirred acetone and for 30 minutes. The fiber was removed, wiped with an acetone-soaked Kimwipe, rinsed with deionized water, and the fiber tip was suspended in a stirred solution of 2 M KOH for 60 minutes. The fibers were removed from the KOH solution, rinsed with 10 mL of deionized water, and re-dipped into 2 M KOH to test wetting. If necessary, the KOH treatment, water rinse, and wetting test were repeated until the KOH solution wet the fiber surface. Once wetting was satisfactory, the fiber tip was rinsed with 10 mL of deionized water and dried using a stream of nitrogen gas. The fibers were immediately dipped by hand into the sol–gel solution at a 15° angle for better coating of tip, and allowed to dry vertically for one hour under ambient conditions to maximize coating uniformity on the tip. Fibers were cured at 70°C for times ranging from 4 to 12 hours. Scotch tape was used to

assemble a flat bundle of five fibers with the fiber tips separated by 1 mm. The bundle of five fibers was dipped by hand at a 15° angle (for better coating of tip) into binder/particle mixtures, being careful to maintain the gap between the fiber tips. The fibers were hung vertically (tip down) and dried under ambient conditions for one hour to promote uniform coating of the fiber tips.

3.2.12 Procedure for the coating of fibers with 55 w/w% powder / sol–gel blends.

Typically, a paste containing ~55 w/w% particles was prepared by adding a known mass of sol–gel particles to a binder solution that had been aged for 5 days at room temperature. The paste was then mixed with gentle grinding in a small vial to increase homogeneity. A clean dry fiber was then dipped at an angle of 15° and hung vertically for 1 hour to achieve a uniform coating and pre-dry the film. The pre-dried film was the cured at 70°C for 16 hours.

3.2.13 Procedure for the coating of fibers with 60 w/w% powder / sol–gel blends.

A paste containing 60 w/w% was prepared by adding a known mass of room temperature aged 55 mol% OtMOS/TEOS based sol–gel solution to a predetermined mass of wlb29 powder to obtain an off-white paste. The paste was then mixed with gentle grinding in a small vial to increase homogeneity. A clean dry fiber was then dipped at an angle of 15° and hung vertically for 1 hour to achieve a uniform coating and pre-dry the film. The pre-dried film was the cured at 70°C for 12 hours.

3.2.14 Procedure for spray coating fiber and planar substrates.

Following the procedure described by Remillard et al,[11] viscous sol–gel solutions containing $K_2Mo_6Cl_{14}$, composite powder, or a combination of both were applied to substrates using a Paasche double action airbrush. Fibers were supported in the barrel of a hypodermic syringe ~4 cm from the tip of the spray coater. The fiber was coated in 1 second bursts aimed directly at the tip with 15 seconds of dry time in between each burst. The pressure of gas supplied to the airbrush was set at 10 psi, and the spray burst size was varied to determine the optimal spray conditions.

Planar substrates were coated similarly. For **slide 38Q**, 25.9 mg of $K_2Mo_6Cl_{14}{\cdot}H_2O$ was added to 10 mL of 10-day old stock sol–gel solution. After stirring overnight, 35.9 mg of composite 31 (25 – 250 μm diameter particles) was added and stirred for 24 hours to form a cloudy suspension. Once stirring ceased, ~25% of the particulates remained suspended. A single coat was applied to a 2.4 cm × 1.25 cm quartz slide for 1 second at a distance of 4 cm from the airbrush tip using nitrogen gas at 10 psi. Immediately after coating the sample, it was placed into an oven and cured for 30 minutes in air at 200°C.

3.2.15 Thermal treatment of samples.

Thermal treatment and curing of coated samples was accomplished by placing them in a vacuum oven (Fischer® model) under various conditions. Coated planar substrates were cured by placing them in a small vial in the horizontal position either under vacuum or ambient pressure at temperatures ranging from room temperature to 200°C and curing for times ranging from 30

minutes to 24 hours. Coated fibers were cured by placing them horizontally on a rack with the coated tip elevated so that it did not touch any surfaces. The fibers were then cured either under vacuum or ambient pressure at temperatures ranging from room temperature to 75°C and curing for times ranging from 30 minutes to 24 hours.

3.2.16 Absorption spectroscopy.

Instrumental details for absorbance measurements can be found in the experimental section of chapter 2.

3.2.17 Optical microscopy of samples.

The details concerning the optical microscopy of samples can be found in the experimental section of chapter 2.

3.2.18 Dark field imaging.

Dark field optics is a low cost alternative to phase contract microscopy that allows one to readily obtain information on surface topography. In dark field the sample is illuminated from above, and only photons collected by annular apertures are collected to form the image. A perfectly flat sample with no topography will appear dark and any topographic features will be accentuated in the image. For dark field imaging, an Olympus BX60 optical microscope in the Michigan State University Keck Microfabrication Facility clean room, with 10×, 20×, 50× and 100× dark field objectives and a SPOT video camera (Diagnostic Instrument model 1.3.0) with ImageGear version 6.6.4 software to determine the particle size of sol–gel powders prepared using the small ball mill (Wig-L-Bug). The individual particles are ~5 μm, with larger 50 μm aggregates.

3.2.19 Mechanical testing of composite adhesion.

A qualitative test of adhesion was performed using a stream of nitrogen gas at ~10 psi directed at the coating on the fiber tip and then followed by gently tapping the distal fiber edge on the edge of the laboratory bench top. An apparatus similar to the Izod impact pendulum[13] was fabricated for more quantitative measurements of adhesion (**Figure 3.2)**.

Fibers were imaged and weighed before testing, and then tape was used to secure the fiber to a sewing thread. The fiber was attached to the pendulum with the length adjusted so that the metal stop impacted the fiber where the fiber jacket had been removed, ~1 cm above the tip. The distance between the fiber impact point and the upper metal bar was ~22–26 cm. The fiber was then set to the desired angle, released, and allowed to impact the metal stop. The fibers were imaged after each test to assess changes in the film morphology. The impact force was calculated using equation 1:

$$I = 2mt^{-1}[3gL(1 - \cos(\theta)]^{½} \quad (1)$$

where I is the impact force in N, m is the mass of the fiber and string in kilograms, t is the amount of time the fiber is in contact with the impact point (estimated at ~0.5×10^{-3} s),[14, 15] θ is the angle of travel in degrees, g is the acceleration due to gravity (9.8 m/s^2), and L is the distance from the pendulum attachment point to the impact point in meters. The estimate used for the time of contact, t, was based on the value used for calculations of impact force between a golf club and a golf ball. While the components of the two systems are obviously different, the physics involved are similar.

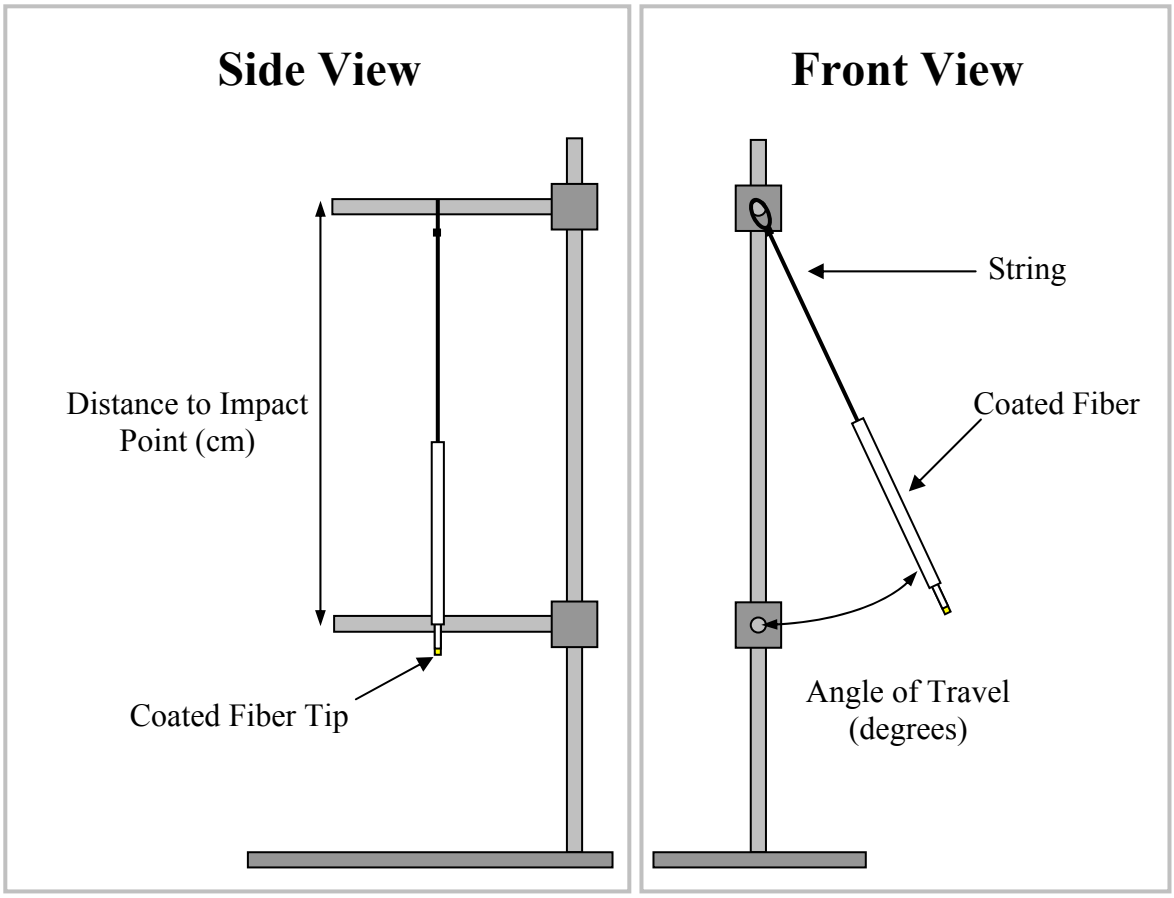

Figure 3.2. The pendulum style apparatus used to quantify the adhesion of coatings on fibers.

3.3 RESULTS AND DISCUSSION

3.3.1 Immobilization of Mo_6Cl_{12} in sol–gel matrices

Developing a high-temperature oxygen fiber sensor based on Mo_6Cl_{12} luminescence quenching requires a scheme for embedding the clusters in a matrix while retaining their unique optical properties. The matrix must adhere strongly to the optical fiber and have high oxygen permeability. These requirements can be satisfied using a sol–gel matrix to immobilize the clusters at the tip of high-temperature silica fibers, such as commercially available gold clad silica fiber rated for long term operation up to 750°C.[16] The silanol terminated surface of the fiber ensures excellent adhesion to the matrix and prior work has shown that the oxygen permeability of sol–gel matrices can be tailored by appropriate choice of reaction conditions.[17] The process for embedding the luminescent clusters must be compatible with the solubility and chemical reactivity of Mo_6Cl_{12}. There are two open coordination sites in the hexanuclear Mo_6Cl_{12} structure (**Figure 3.3**).

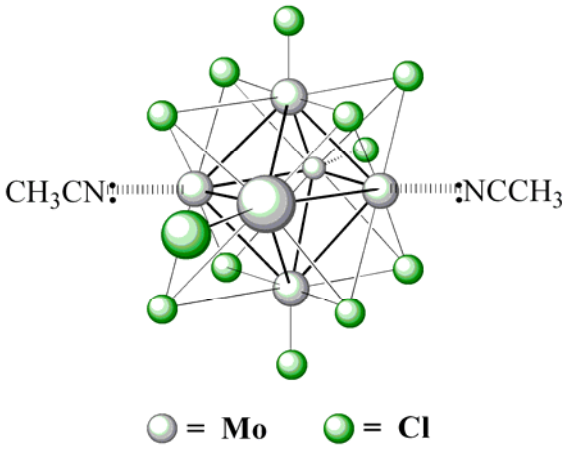

Figure 3.3. Luminescent Mo_6Cl_{12} clusters with acetonitrile bound to the two open coordination sites.

In the solid state, both sites are occupied by bridging chlorides from adjacent clusters resulting in a polymeric structure. In polar solvents such as acetonitrile, ethanol or 6 M HCl, the solvent displaces the bridging chlorides to give a complex. Because HCl strongly affects the sol–gel reaction rate and the cluster formed insoluble oxo-bridged species in ethanol, the acetonitrile complex of Mo_6Cl_{12} (Mo_6Cl_{12}•$2CH_3CN$) was used in the sol–gel syntheses since acetonitrile has been used successfully as a cosolvent in sol–gel syntheses.[18] While stirring Mo_6Cl_{12} in acetonitrile for several days eventually yields concentrated orange-yellow solutions of the acetonitrile complex, it was found that the complex is more conveniently prepared by loading Mo_6Cl_{12} into the thimble of a Soxhlet extractor and exhaustively extracting with dry acetonitrile. The use of dry solvent is important as it minimizes formation of less soluble hydroxyl-substituted complexes.

The spectroscopic features of the acetonitrile complex are shown in **Figure 3.4**. Excitation of Mo_6Cl_{12} clusters in the UV (λ <400 nm) leads to a long lived excited state, which decays to the ground state with emission of red luminescence centered at ~750 nm.

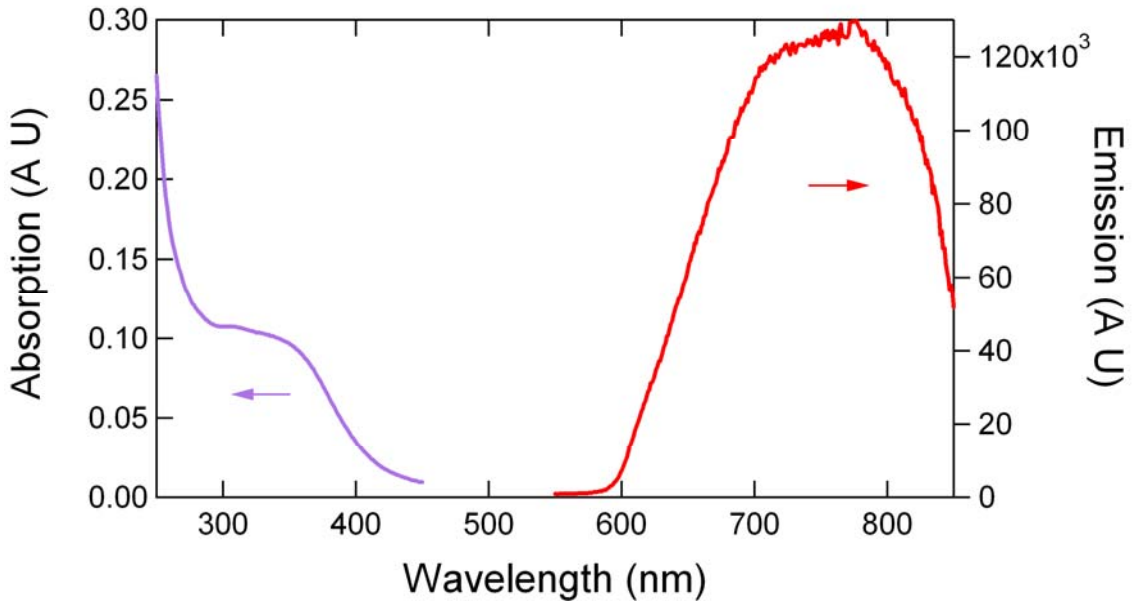

Figure 3.4. Absorbance and emission spectra of the acetonitrile complex of (~4 × 10^{-5} mol/L). The emission is the uncorrected raw data, taken with an excitation wavelength of 313 nm. Quenching of ~12× is observed between nitrogen (<0.001 vol% oxygen) and air. The data was obtained by the author in collaboration with R. N. Ghosh.

The large Stokes shift of the emission (>400 nm) greatly simplifies the design of a reflection mode fiber sensor since photons over the entire emission band can be collected and the UV excitation signal can be removed using simple band pass filters. The large quantum yield (0.19 in acetonitrile at 300K) allows simple sources such as a UV LED or mercury pen lamp to be used as the UV source. Excitation spectra were obtained by exciting at 313 nm while scanning the emission from 550 nm to 850 nm. The absorbance of the solutions used for these experiments were adjusted to ~0.1 at 313 nm to minimize self-quenching effects. Using reported extinction coefficients for Mo_6Cl_{12} clusters (ε = 3000 L mol^{-1} cm^{-1})[19-21], the concentrations were estimated to be 4 × 10^{-5} M. A concern is whether the clusters in the matrix exist as isolated species or as aggregates. Having the former is important to avoid decreases in luminescence due

to self-quenching. In solution, Mo_6Cl_{12}•$2CH_3CN$ appears to be monomeric since the luminescence intensities scale linearly with changes in concentration and the luminescence intensity and quenching behavior of its solutions are comparable to those of molybdenum clusters (e.g. $Mo_6Cl_{14}^{2-}$), which are known to be monomeric.[19] The excited states of Mo_6Cl_{12} clusters are efficiently quenched by oxygen. Spectra for Mo_6Cl_{12}•$2CH_3CN$ solutions measured in room air and under nitrogen are also shown in **Figure 3.4**. The data indicate quenching by a factor of 12×, with the luminescence intensity and line shape returning to their original values upon equilibration with room air. Luminescence quenching data for Mo_6Cl_{12} clusters follows the Stern–Volmer equation[7] for bimolecular collisional quenching, $I/I_0 = 1/(1+K_{sv}[O_2])$, where I and I_0 are the luminescence intensity in the presence and absence of oxygen of concentration $[O_2]$ and K_{sv} is the Stern–Volmer constant.

The process used to embed the acetonitrile complex in a sol–gel matrix outlined in **Figure 3.7** is based on the controlled hydrolysis and condensation of tetraethylorthosilicate where ethoxy groups are lost in the form of ethanol, and new Si-O-Si bonds form to generate the silica matrix.

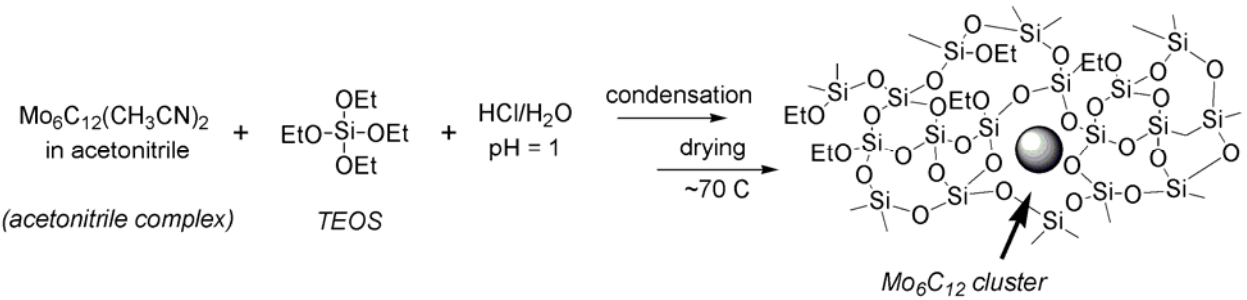

Figure 3.5. Synthetic route to sol–gel immobilized clusters.

By carrying out the reaction in the presence of the clusters, Mo_6Cl_{12} is entrapped the in the final matrix. Because of its high solubility in the reactants, the acetonitrile complex of Mo_6Cl_{12} is particularly useful for obtaining sol–gel matrices that contain an appreciable concentration of Mo_6Cl_{12}. A requirement is that the sol–gel film be sufficiently porous to allow rapid diffusion of oxygen through the matrix. A series of experiments that lead to sol–gel matrices with different oxygen permeabilities have been reported.[17, 22, 23] Using those conditions as a starting point, a solution of TEOS, Mo_6Cl_{12}•$2CH_3CN$ dissolved in acetonitrile and aqueous HCl was prepared, and then aged the solution at 70°C for 2.5 h. Since acetonitrile is known to increase the rates of sol–gel reactions,[18] the change in the viscosity of the solution was monitored and clean quartz substrates were dip-coated at regular intervals. Drying at room temperature for ~1 week followed by heating at 70°C for 24 hours gave clear films that adhered strongly to the substrate. These films glow brightly when illuminated with a hand held UV lamp, and as shown in **Figure 3.6** the emission line shape of Mo_6Cl_{12}•$2CH_3CN$ embedded in the sol–gel matrix matches that of the cluster in CH_3CN.

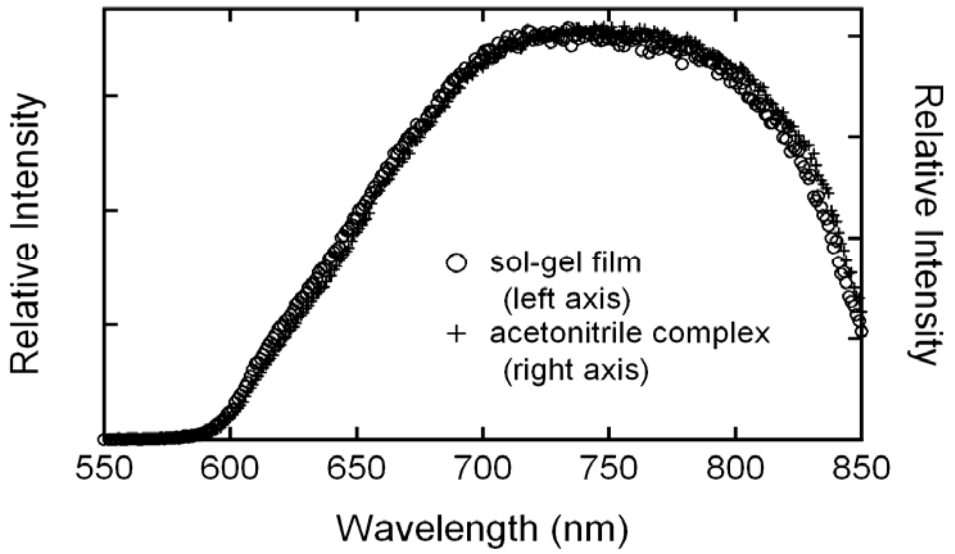

Figure 3.6. Emission spectra of Mo_6Cl_{12}•$2CH_3CN$ demonstrating no change in the cluster line shape between the CH_3CN solution and the sol–gel matrix.[24]

3.3.2 Film deposition techniques

Coating quartz substrates with $K_2Mo_6Cl_{14}$•$1H_2O$ clusters embedded in sol–gel films is a key prerequisite for studying the temperature dependent photophysics of $K_2Mo_6Cl_{14}$•$1H_2O$ clusters relevant to oxygen sensing based on luminescence quenching. The film requirements are high optical clarity (absence of cloudiness or substantial cracking), mechanical stability (good adhesion), uniformity in thickness and a sufficient concentration of clusters to support luminescence and quenching measurements over a broad range of temperatures. Both hand dipping and a mechanized dipping process were used to coat planar substrates. The apparatus used for mechanized dipping, shown in **Figure 3.7,** provides precise control over the rate at which substrates are withdrawn from sol–gel solutions. Using constant dipping rates resulted in improved film quality as evidenced by smooth films with decreased cracking frequency.

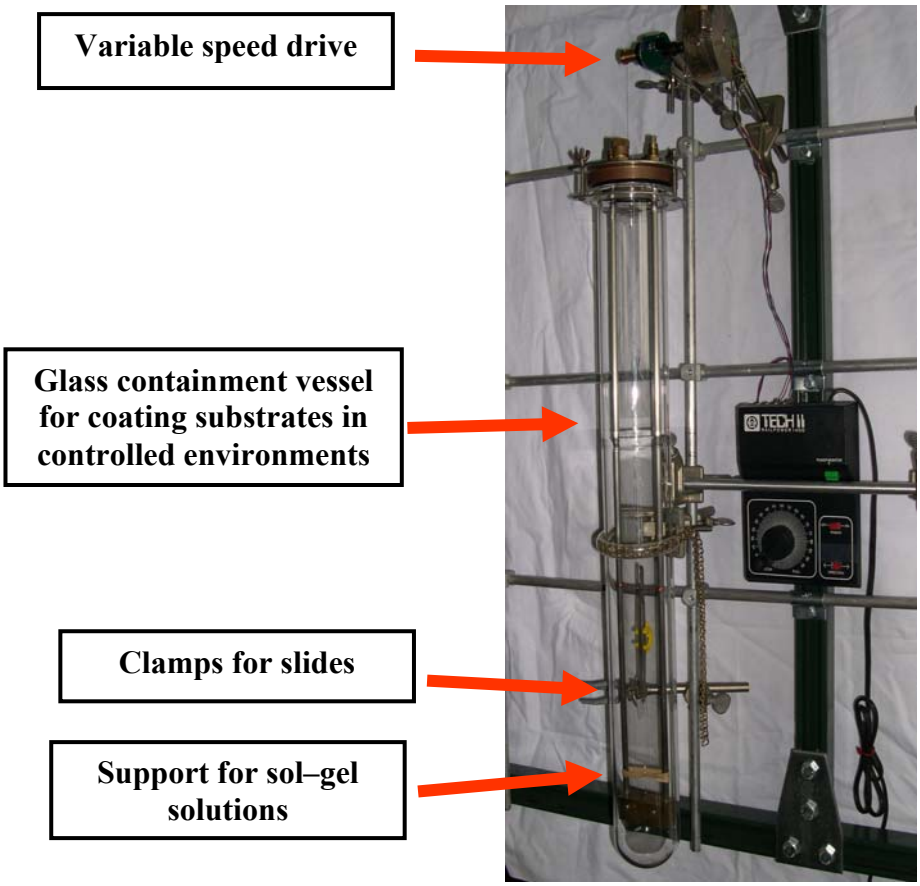

Figure 3.7. Apparatus used for controlled coating of planar substrates. The overall height of the apparatus is approximately one meter.

A second technique suitable for deposition of films on substrates is spray coating. Advantages of spray coating include the ability to deposit thin films uniformly and rapidly on surfaces, rapid drying times, and high throughput. A disadvantage of spray coating is that the resulting films generally are quite thin, often on the order of 1 μm. A convenient way of applying films in the laboratory is to use the commercial airbrush. Shown in **Figure 3.8** is a simple rig for spray deposition on planar substrates and at the tips of fibers. The target and the spray apparatus can be enclosed to control the evaporation rate of the solvent. Since the films are thin, significant cracking characteristic of thicker films is avoided. These films are suitable for spectroscopic

measurements of the clusters embedded in the matrix. However multiple coats need to be deposited to obtain thicker films so that the signal from the lumophores is sufficiently strong for simple optical detection of the luminescence quenching.

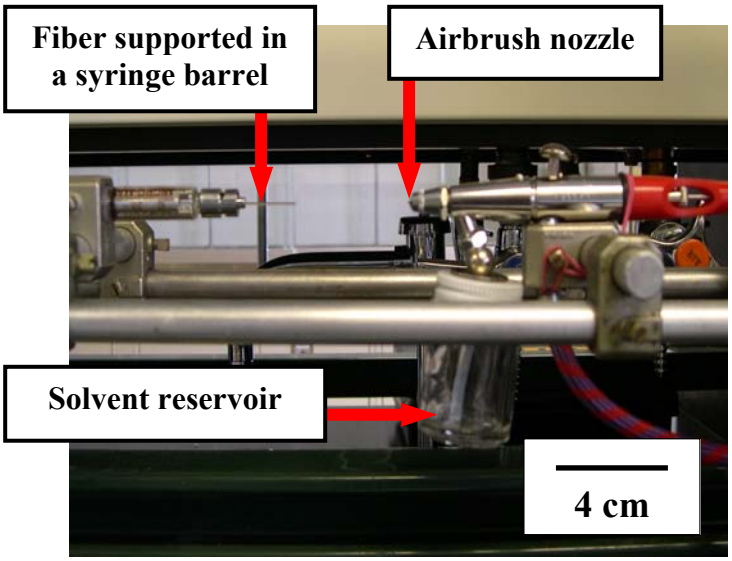

Figure 3.8. Apparatus used for spray coating of high-temperature optical fibers

Deposition of sol–gel films on fibers is more challenging. Spray coating results were disappointing in that we have been unable to apply multiple coatings to build up thick films and at the same time avoid cracking. A typical spray coating result is shown in the optical micrographs in **Figure 3.9**. Cracking in the sol–gel film spray coated on the surface of a high-temperature optical fiber is conspicuous. In addition the thinness of the film translates into a low absolute number of clusters available for sensing. Simply increasing the concentration of clusters in the sol–gel solution is limited to the low solubility of clusters in the acetonitrile solvent. Another disadvantage of spray coating with clusters dissolved in a sol–gel solution is that the

sol–gel matrix undergoes a large decrease in volume as the sol–gel matrix cures. The large internal stress in such films exacerbates potential cracking problems.

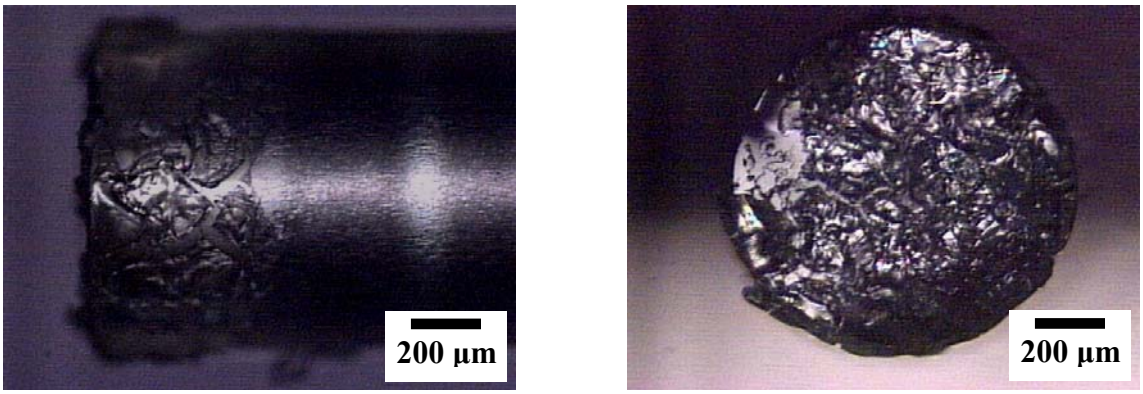

Figure 3.9. Typical results for multilayer deposition of sol–gel solution by spray coating showing obvious cracking.

3.3.3 Controlling the morphology of sol–gel films on surfaces and fibers.

One problem characteristic of materials prepared by sol–gel synthesis is their propensity to fracture during curing. This problem can be understood by considering the changes in the structure of sol–gel matrices as they cure. The chemistry of the sol–gel process involves the condensation of tetraethylorthosilicate (TEOS) in the presence of either an acid or a base catalyst and solvent. As TEOS hydrolyzes and loses ethanol, the silanols generated by hydrolysis condense to form the "sol". At some point in the process, the sol solution is spread on the surface of a substrate by dip or spray coating. Solvent evaporation plus the hydrolysis and condensation of residual alkoxysilanes complete the process. If the substrate is non-adhesive, the film (often termed a monolith if it is too thick to be considered to be a film) shrinks both laterally and in thickness, and if done under near-equilibrium conditions where the rates of condensation and evaporation are uniform throughout the material, the film or monolith is

transformed into a homogeneous solid. Thin films deposited on fibers or planar substrates for optical experiments must have good adherence to the substrate. For these cases, condensation and drying develops substantial strain in the material, often exceeding the yield stress of the material. Such films crack, and upon release of the strain, delaminate from the surface. The likelihood of such failures increases as the films are made thicker.

To obtain high quality films for optical experiments, a systematic evaluation of cleaning and deposition procedures that lead to high quality films was carried out. A range of surface preparation techniques were examined and it was found that the choice of surface preparation did not correlate with the likelihood of a film cracking. However, film thickness did correlate with cracking, with thinner films being less likely to crack. An interesting example of this phenomenon is shown in a series of slides prepared by dip coating clean slides into a sol–gel solution. The sol–gel film was deposited on both sides of the substrate and then the substrates were stored horizontally in small vials and allowed to dry. All of the films on the top side of the substrate (see **Figure 3.10**) cracked within 24 hours, while those on the bottom of slide did not. The crucial difference was that the film on the bottom face of the substrate was in contact with the walls of the vial allowing a portion of the film to flow from the slide to the wall, effectively thinning the film. These slides are shown in the micrographs in **Figure 3.10**.

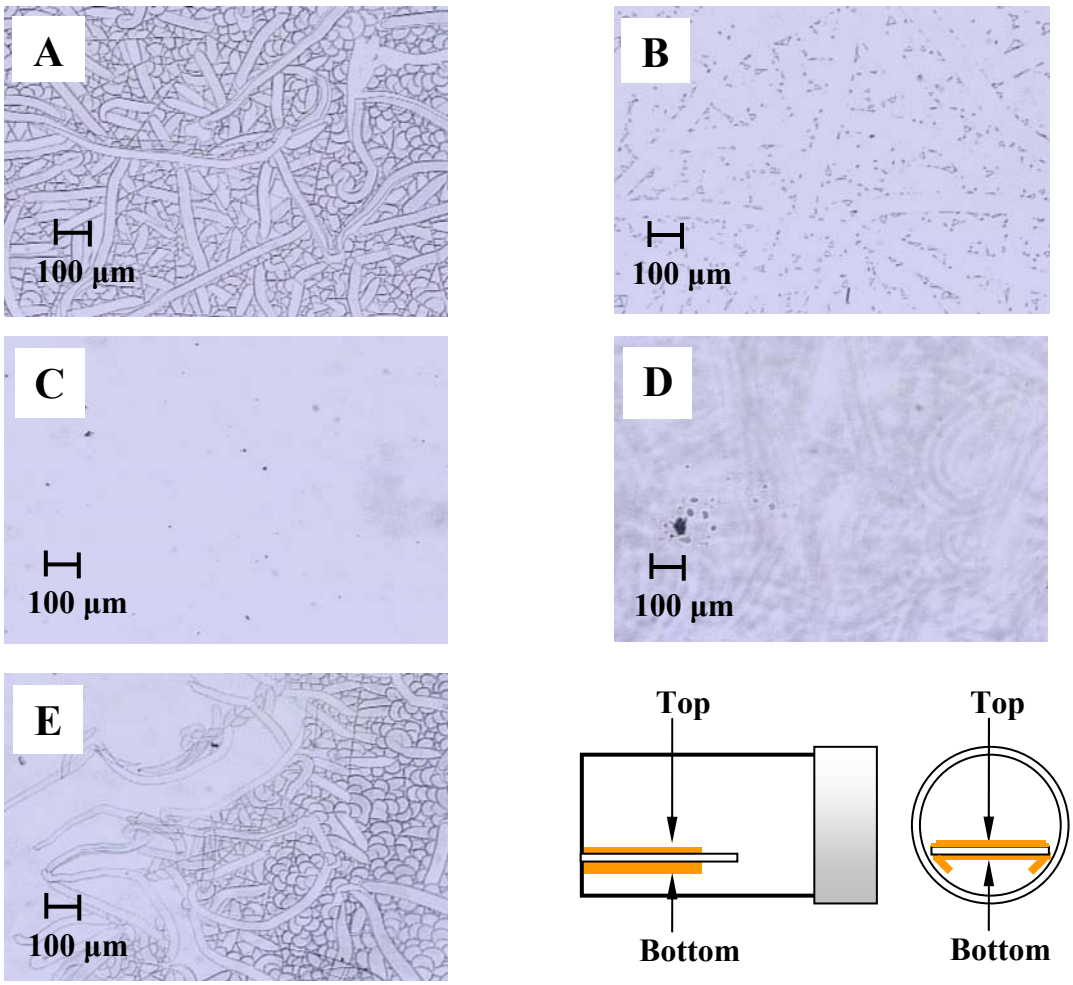

Figure 3.10. Optical micrographs of the surfaces of slides coated with sol–gel films. (A) Top face of a slide showing the characteristic cracking pattern of thick films. (B) Top face after applying and removing tape. Note that while nearly all of the film has been removed, the original pattern can be inferred from residual fragments of the sol gel film. (C) Bottom face of the same slide showing no cracking. The film on the top face was removed by tape as in panel B. (D) The same face after applying and removing tape. This micrograph was taken in an area of the film where the top film was not removed. The unfocussed image of the top film (cracked) can be seen in the background. (E) Cracking pattern seen at the extreme edges of the film showing the evolution of cracking. The schematic at the bottom right defines the orientation of the film while drying.

Panel A shows the dried film deposited on the top side of the substrate. During the drying process, the stress induced by the drying led an interesting and extensive pattern of cracking. The cracked film has poor adhesion to the surface. As shown in panel B, applying tape to the

surface followed by peeling the tape from the surface removes nearly all of the sol–gel film. Carrying out the same experiment on the bottom side of the film led to strikingly different results. The film, initially clear with no visible cracks, is unaffected by the tape test indicating excellent adhesion. Only the extreme edges of the film showed any sign of delamination (panel E). These observations suggest that under identical drying conditions, film thickness is the primary variable that determines film quality. This hypothesis was confirmed by dip coating a series of slides and orienting them vertically during the drying process. In this case, both sides of the film were crack free, with cracking seen only for the bottom edge of the film which had the highest thickness. Similar effects were seen in experiments on optical fibers. The fibers used were standard optical fibers – suitable for testing film deposition and adherence, but not rated for UV. Approximately twenty fibers were dip coated and after drying, they were subjected to a simple adhesion test, snapping the end of the fiber with a finger. Fibers with thick coatings generally failed with the sol–gel matrix fracturing and often dislodged from the fiber. In contrast, those fibers with thin coatings passed the test and showed no fractures. **Figure 3.11** shows two such fibers, one having a thin uniform coating, and a second example showing a fracture developed in the sol–gel film.

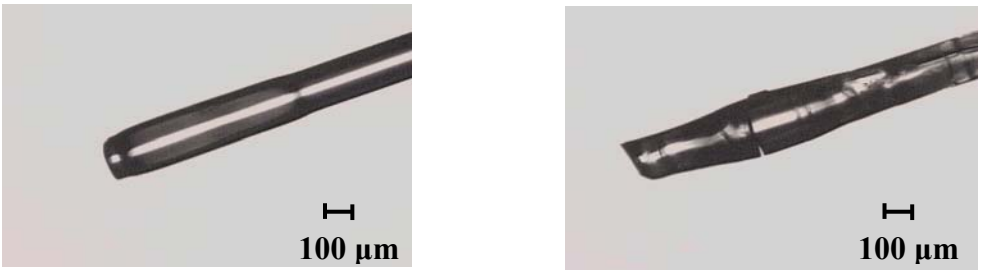

Figure 3.11. Optical micrographs of optical fibers coated with a sol–gel matrix containing no Mo_6Cl_{12} clusters. Note the cracking for the thick film on the right.

3.3.4 Optical properties of Mo_6Cl_{12} embedded in sol–gel matrix

Using the process described in the Experimental section, thin films of the Mo-cluster/sol–gel composite were deposited on quartz slides and allowed to cure. The emission spectra of the Mo-cluster/sol–gel films were measured and then the samples were heated to 200°C for one hour. Depending on the thickness of the film and the details of the preparation, the films developed a network of cracks forming domain size on the order of 100 μm after curing that was largely unchanged by the heating process. Since the core diameter of the high-temperature optical fiber is ~100 μm, this process should provide crack free Mo-cluster/sol–gel composite films that completely coat the end of the fiber. Adhesion of films to substrates is excellent; attempts to scratch the film to measure thickness using a surface profilometer were unsuccessful. Oxygen quenching of the luminescence from Mo-cluster/sol–gel film **15F** after heating to 200°C are shown in **Figure 3.12**.

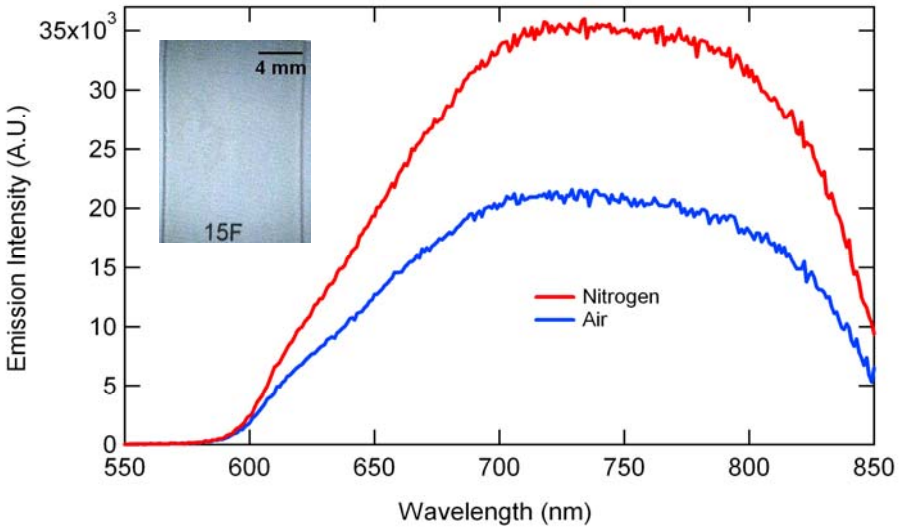

Figure 3.12. Emission spectra of Mo-cluster/sol-gel composite film **15F** (inset), after heating to 200°C for one hour.[24] Quenching of 1.7× is observed between nitrogen (< 0.001% oxygen) and air (~20% oxygen). Excitation wavelength is 313 nm. The data was obtained by the author in collaboration with R. N. Ghosh.

The film was heated to 200°C for one hour prior to the measurement. Note that the clusters immobilized in the sol–gel matrix after heat treatment have the same emission lineshape as the isolated clusters in solution (**Figure 3.6**). This indicates that neither the sol–gel chemistry nor heating to 200°C have adverse effects on the cluster photophysics. We believe that the lower degree of oxygen quenching in the sol–gel matrix as compared to the solution results is related to the porosity of the sol–gel matrix, which can be controlled by aging time and the inclusion of porogens in the sol–gel process.

3.3.5 The composite material approach to sensing layers.

To realize a practical sensor based on $K_2Mo_6Cl_{14}•1H_2O$, the molybdenum clusters must be immobilized at the end of high-temperature optical fibers using methods that ensure high luminescence intensity from the clusters and strong quenching of the luminescence in the presence of oxygen. Previously we discovered that despite long aging and drying times, films deposited on substrates continued to evolve when they were tested at high temperatures. In general the quenching ratio ($I_{oxygen}/I_{nitrogen}$) decreased, which is consistent with densification of the sol–gel matrix. It appears that the limiting factor in the quenching process is the diffusion of oxygen to the molybdenum clusters, and that the oxygen diffusivity in the heat-treated sol–gel matrices was low. Both the change in the physical parameters of the sol–gel matrix and the low quenching ratio are problems that must be solved in any practical sensor.

A composite material approach was developed that involves embedding molybdenum-containing sol–gel particles in a binder that essentially glues the particles to the substrate (**Figure 3.15**).

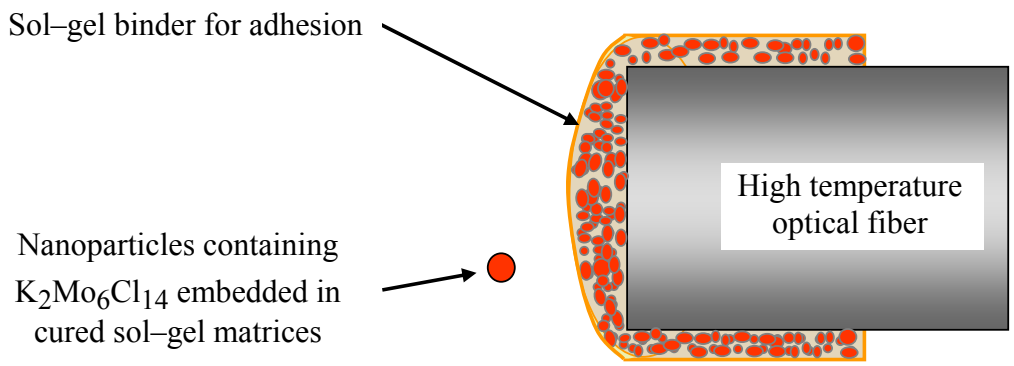

Figure 3.13. Schematic showing the expected morphology resulting from dip or spray coating a slurry of particles in a sol–gel binder solution. The particles correspond to pre-cured sol–gel particles containing $K_2Mo_6Cl_{14}$•$1H_2O$ clusters.

This approach offers several advantages that overcome some of the limitations encountered when depositing a homogeneous solution of the cluster in a sol–gel solution. First, by using a preformed and fully equilibrated cluster containing sol–gel matrix, issues related to the long-term aging of the sol–gel matrix are avoided. Second, the use of small particle sizes should lead to large quenching ratios since in the limit of infinitely small particles the diffusivity of oxygen should be dominated by the permeability of the binder. We expect that the binder will be a minority component of the matrix, filling the void space between the particles, and that curing the binder will lead to little change in the volume of the composite. The net result is that the binder should have a low density, high oxygen permeability, and that the composite matrix should have an enhanced quenching ratio compared to sol–gel monoliths. Third, the composite material approach allows us to use the same cluster/sol–gel source for a series of sensors leading to sensors with predictable characteristics. To that end a monolith previously prepared from a

sol–gel solution containing molybdenum clusters (**MM-5**) was selected. **Figure 3.14** shows a micrograph of the **MM-5** containing sol–gel and the particle size achieved by grinding the monolith into a fine powder using a standard mortar and pestle.

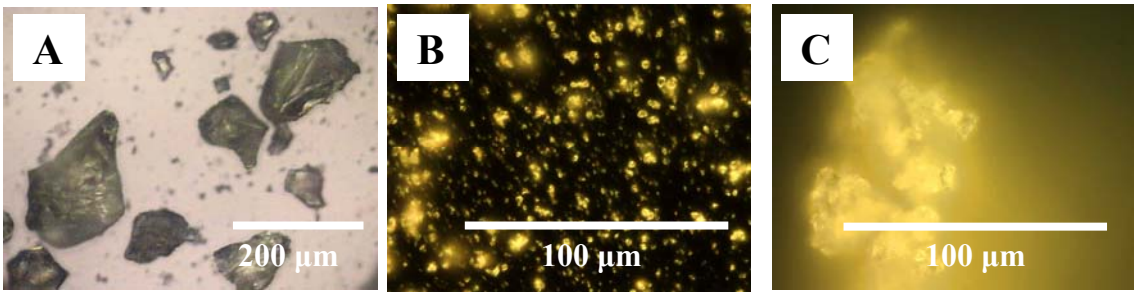

Figure 3.14. Optical micrographs of sol–gel particles (A) bright field image (10×) showing a sol–gel monolith containing **MM-5** pulverized using a mortar and pestle, 25 µm –250 µm particle size, (B) a sol–gel monolith (no clusters), 1 µm – 2 µm particle size, and (C) dark field image (100×) showing a sol–gel monolith containing **MM-5** pulverized via ball milling, 2 µm – 8 µm particle size.

Adding a freshly prepared sol–gel solution gave a paste-like material composed of either 50 wt% or 60 wt% particles and the remainder binder. While the viscosity of the paste proved to be too high for effective spraying, reduction of the particle size seems to be the logical approach for reducing the viscosity since diluting the particles with more sol–gel solution would reduce the net luminescence of the matrix. Coating slides and fibers using a hand-dipping procedure gave films that strongly luminesced. An examination of films deposited on fibers (**Figure 3.15**) shows that the particle sizes are relatively large, between 25 µm and 150 µm for fibers **C**, **D**, and **E**. As noted above, smaller particles are desired to achieve better quenching ratios and more uniform deposition.

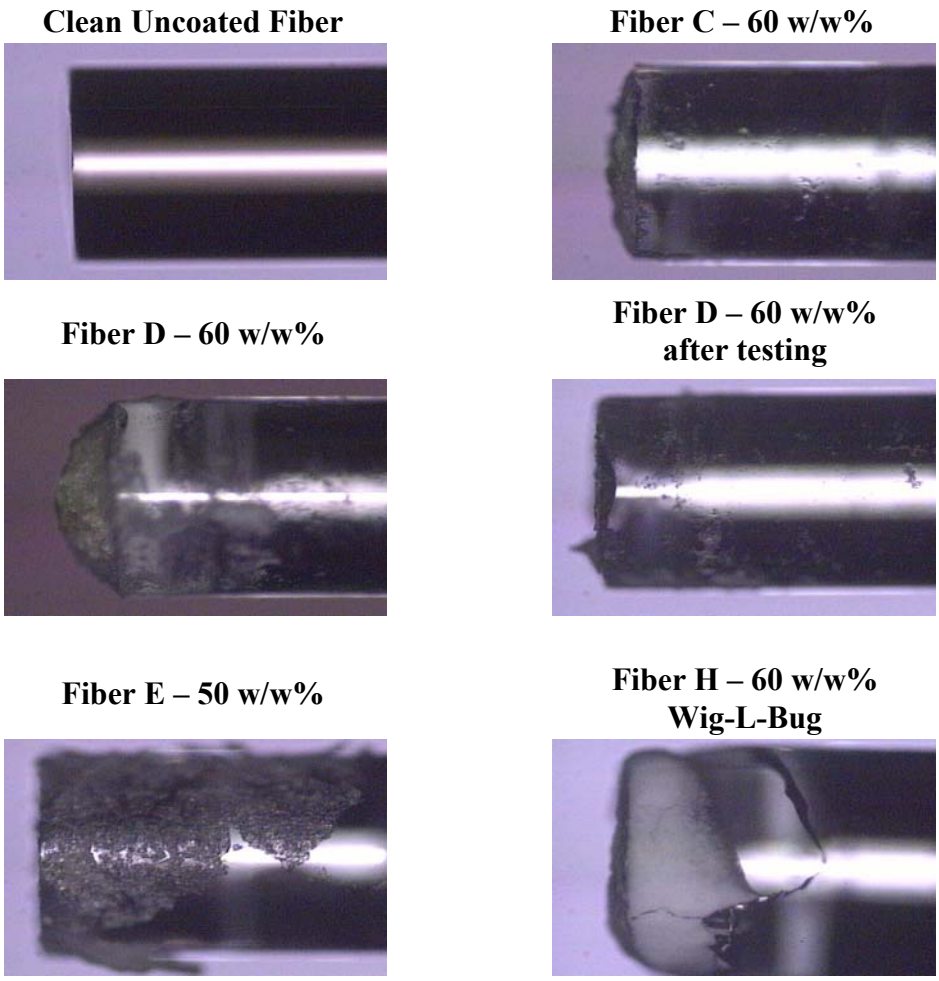

Figure 3.15. Typical dip coating results for deposition of composite/sol–gel binder blends 1000-μm diameter fibers.

Using a ball milling technique reduced the particles to ~5 μm with a significantly tighter size distribution 1 μm – 8 μm (see **Figures 3.16b** and **3.16c).** The films prepared from these materials are more uniform and smooth (fiber **H**, **Figure 3.15**). Using a monolith with the same room temperature aging time (7 months), cluster source (**FJ-17**), and cluster density (1×10^{-18} cluster/cm^3), we used the ball milling technique to prepare particles of roughly the same size (**wlb34g–o**, 1 μm – 8 μm, **Figure 3.16)**.

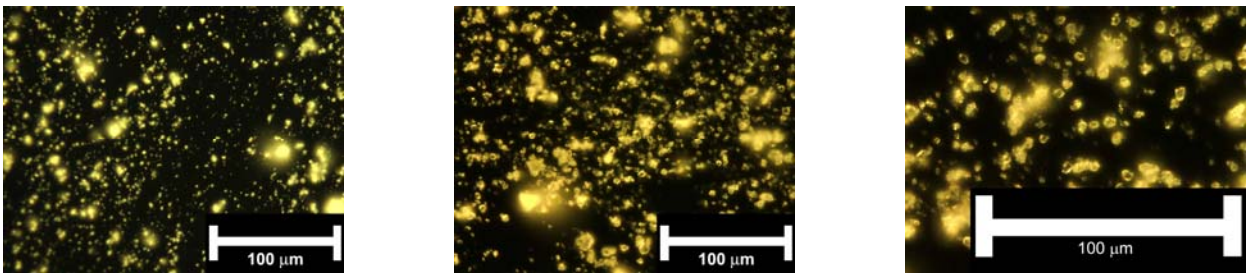

A **B** **C**

Figure 3.16. Dark field optical micrographs of 1 μm – 8 μm sol–gel particles (cluster source **FJ-17**) prepared by ball milling (A) previously prepared **wlb29** (50×), (B) **wlb34g–o**, (50×) and (C) **wlb34g–o**, dark field (100×).

The materials we generated by this approach are promising in that the quenching ratios were >5× for some fibers coated with a composite material. In addition the optical fibers have more stable properties using the particle in binder approach. One problem was not solved by this approach; the adhesion of the composite material to the tip of the fiber was poor, and the fibers that were produced by this method are probably too fragile for most applications. There was a common failure mode for these fibers, after thermal cycling the composite was completely dislodged from the fiber tip. Close analysis of the fibers after failure suggests that in many cases there was a thin sol–gel layer still adhering to the surface. We believe that the failure stems from the shrinkage of the sol–gel binder that leads to a large stress at the interface and eventually catastrophic failure.

The obvious solution to this problem is to remove the source of stress and/or strengthen the mechanical properties of the binder itself. Two approaches were investigated. In the first, the chemistry used in the sol–gel binder was altered to reduce binder shrinkage during curing.

Minimizing shrinkage should improve adhesion by reducing the stress at the interface between the composite and the fiber. In the second, a somewhat unusual approach was taken and the possibility of using commercial adhesives to glue the sol–gel particles to the fiber surface was briefly investigated. If successful, this would simplify sensor fabrication since most glues cure rapidly. A commercial cyanoacrylate adhesive (Tite Bond super glue®) was used to test the notion that the sol–gel particles could be glued directly to the end of the fiber. This process simply requires coating the tip of the optical fiber with glue and then depositing the sol–gel particles containing the molybdenum complex onto the surface of the fiber. Curing is completed in minutes. The resulting fibers are quite interesting and not surprisingly, there is excellent adhesion of the glue and particles to the surface of the fiber. As shown in **Figure 3.19**, the particles appear to cover the surface although the uniformity of the coating is poor, partly due to the use of large particles.

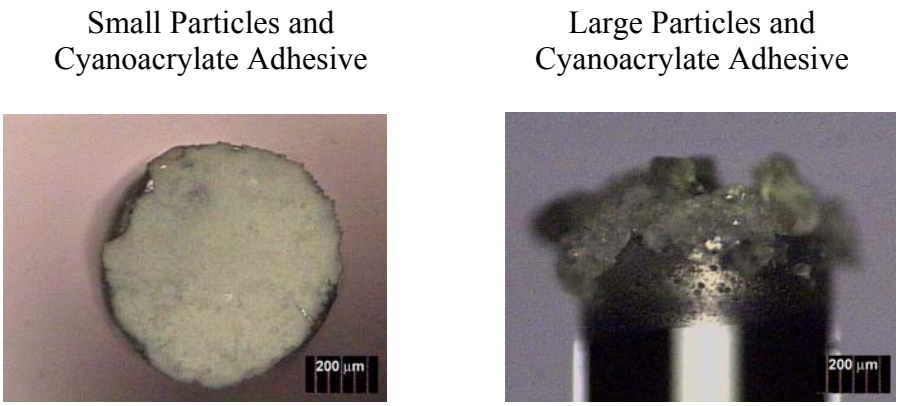

Figure 3.17. Images showing the range of results using cyanoacrylate adhesive as a binder. Small particles are 1 µm – 8 µm and large particles are 25 µm – 250 µm.

The uniformity of the coating seems inferior to the control sample shown in the left panel. The luminescence intensities from these fibers in nitrogen and oxygen yield high quenching ratios that approach those of solutions. However, there are two significant problems with this approach. The first is that the fiber-particle interface is a thin layer of glue, and particle-particle adhesion is poor. Not surprisingly, the composite material at the tip of the fiber was easily abraded from the surface. Using more glue resulted in high luminescence intensity and quenching ratio, but the luminescence from the composite degraded over time, suggesting a deleterious chemical interaction between the glue and the clusters. The latter result prompted us to reconsider sol–gel binders.

It was found that a reliable way to increase the adhesion of the composite to the fiber tip is to use a sol–gel binder that undergoes minimal shrinkage as it cures. Such materials can be prepared by replacing a portion of the TEOS in the sol–gel recipe with alkyltriethoxysilanes such as octyltrimethoxysilane (OtMOS). Reducing the number of functional groups from four to three plus the addition of the alkyl group directly bonded to silicon reduces the cross-link density in the resulting sol–gel matrix and decreases the shrinkage that occurs during curing. Cleaned fibers were coated with a mixture of sol–gel particles and the new binder formulation with ethanol as the co-solvent, cured, and then evaluated by microscopy and by luminescence measurements. These fibers (**Figure 3.18**) showed improved uniformity, and their adhesion to the tip of the fiber also was improved.

Small Particles in 55 mol% OtMOS / TEOS binder using the indicated solvent

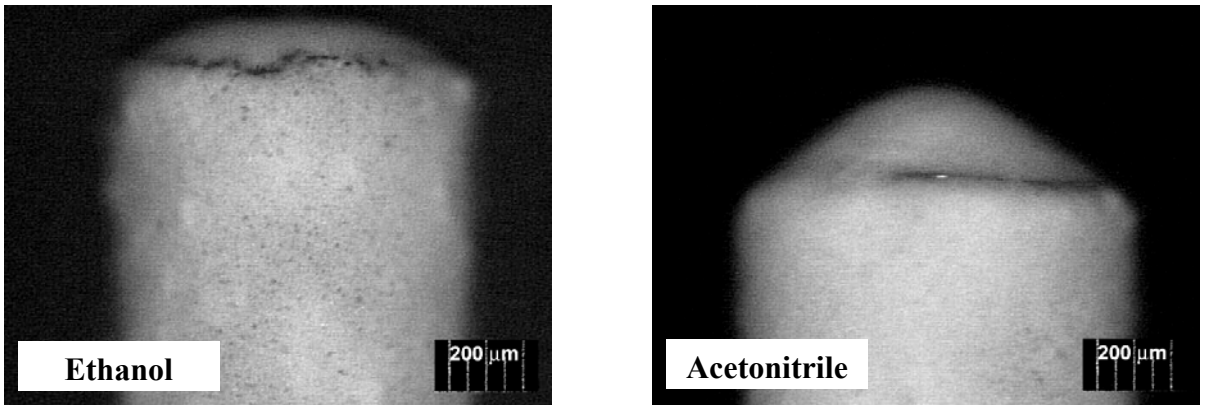

Large Particles in 55 mol% OtMOS / TEOS binder using the indicated solvent

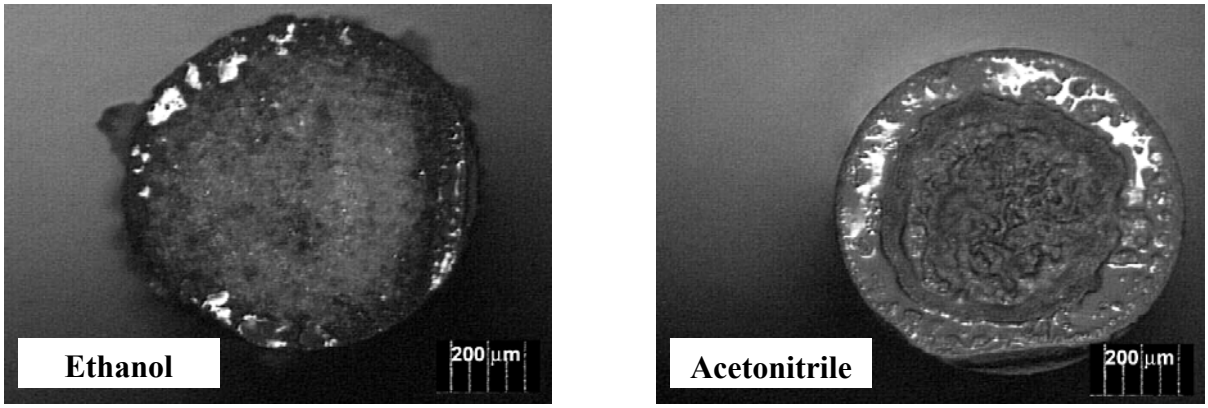

Figure 3.18. Images showing the range of results obtained from coating with different binder solutions and particle sizes. The large particles are 25 µm – 250 µm and the small particles are 1 µm – 8 µm.

Figure 3.19 shows further examples of this modified approach, contrasting the use of acetonitrile and ethanol as co-solvents. All of the samples used finely powdered sol–gel particles and all show excellent coating and adhesion to the fiber surface.

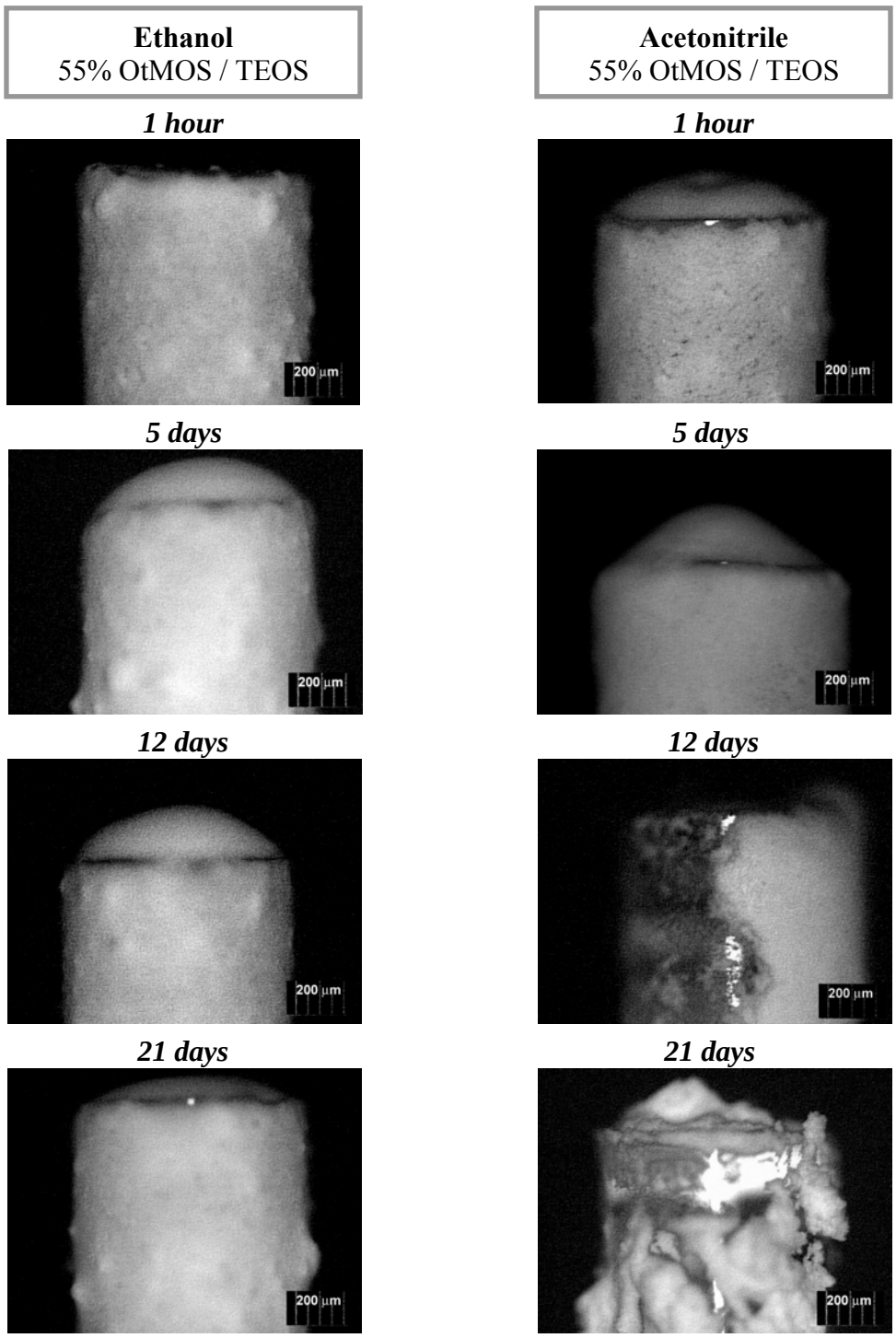

Figure 3.19. Images showing the range of film properties and adhesion obtained by varying the sol–gel aging time and cosolvent. The binder composition is 55 mol% OtMOS/TEOS and the diameter of the particles are 1 µm – 8 µm for all samples.

Given the success of the 55 mol% OtMOS/TEOS binder solution, two alternative binders were briefly investigated. It was reported that quenching ratios of ~14 and linear Stern–Volmer calibration plots for organic lumophores immobilized in matrices prepared from octyltriethoxysilane (OtEOS) in TEOS.[22] Another publication reported quenching ratios of ~35 and linear Stern–Volmer calibration plots from a 67 mol% (3,3,3-triflouropropyl)tri-methoxysilane (TFP-tMOS) in propyltrimethoxysilane (PtMOS) sol–gel system.[23] The fluorinated sol–gel system may prove interesting in aqueous dissolved oxygen sensing. **Figure 3.20** shows examples of these two sol–gel systems as applied to potassium cluster lumophores. All samples used finely powdered sol–gel particles and all show excellent coating and adhesion to the fiber surface.

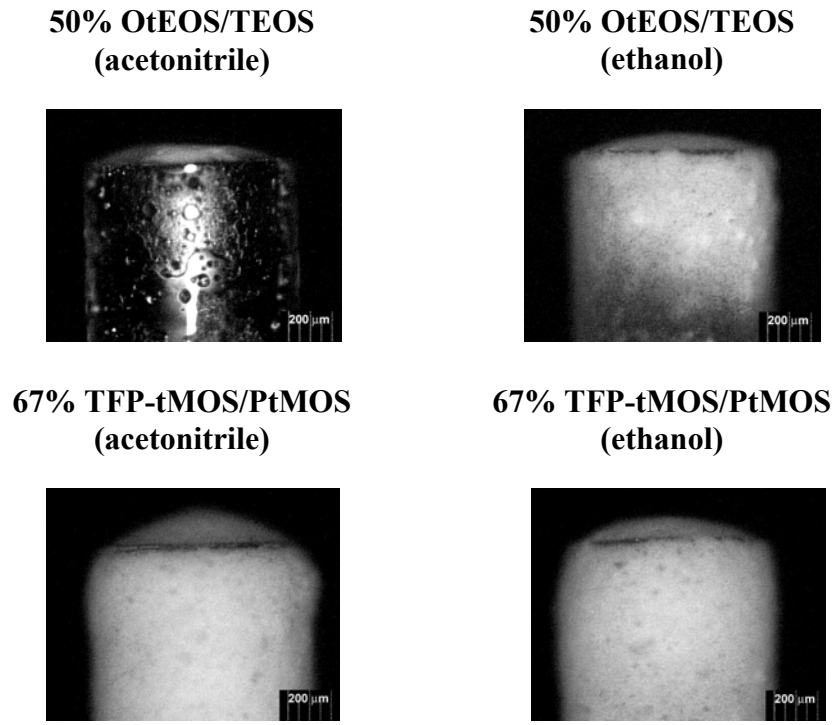

Figure 3.20. Typical results for fibers coated with 53 wt% particles in 50 mol% OtEOS/TEOS and 67 mol% TFP-tMOS/PtMOS.

3.3.6 Multifiber dip-coating of fiber sensors

We moved from single fiber dipping to dip-coating a 5-fiber array to minimize fiber-to-fiber variation. In principle, this process can be scaled to allow simultaneous coating of a large number of fibers. Tape was used to assemble a flat bundle of five fibers with the fiber tips separated by 1 mm. The bundle of five fibers was dipped by hand into binder/particle mixtures, being careful to maintain the gap between the fiber tips and dried under ambient conditions for one hour to promote uniform coating of the fiber tips. Typical results from the simultaneous dipping of five fibers are shown in **Figure 3.21**. Access to fibers with similar properties enables parallel testing of fibers under a broad range of conditions. Different cluster/sol–gel monoliths were tested to optimize sensor performance and adhesion for each case. The smaller particles obtained using a small ball mill gave better adhesion and sensor performance.

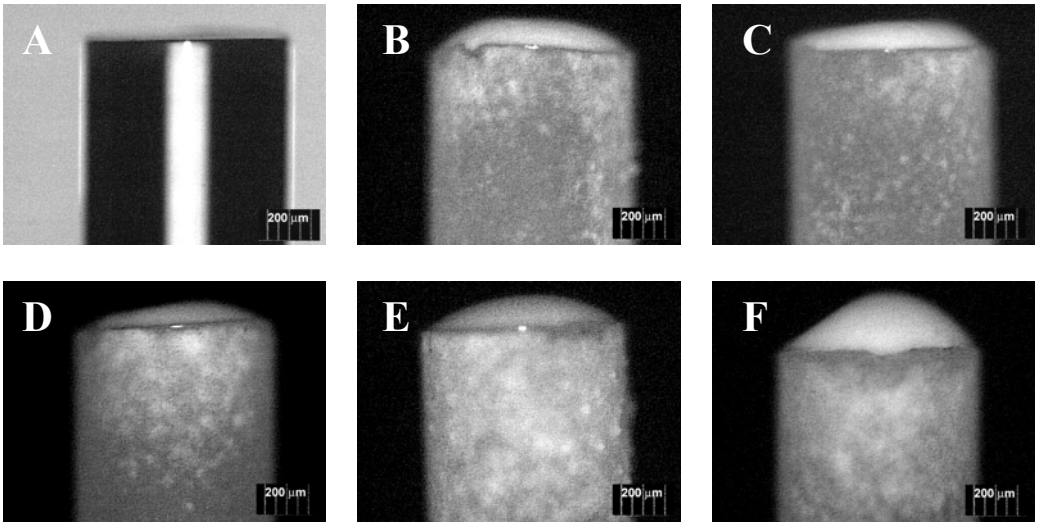

Figure 3.21. Typical results for simultaneous dip coating five 1000-µm diameter fibers with particle/sol–gel binder blends. Image A shows an uncoated fiber for reference. Images B–D are fibers were coated with a mixture of 53 wt% **wlb29** powder in 55 mol% OtMOS/TEOS binder.

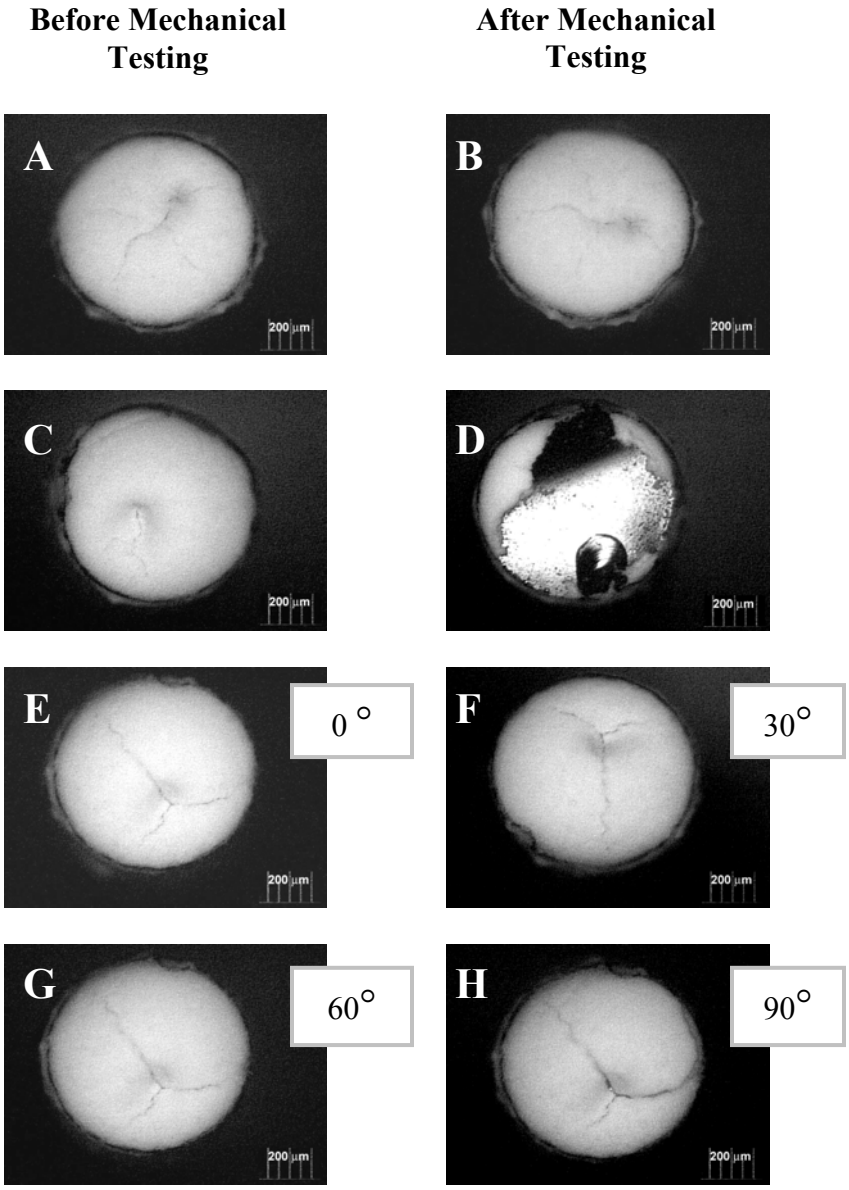

Figure 3.22. Images of fibers coated with 53 wt% **wlb29** powder in 55 mol% OtMOS/TEOS binder before and after mechanical testing. Panels A and B are the before and after images of a fiber tested at 30°; C and D are the before and after images from a second fiber tested at 90°. Images E–H are from a single fiber. Image E shows the fiber before testing, and F, G, and H show results after impacting from 30°, 60° and 90°, respectively.

The fibers were weighed, imaged, and then attached to the pendulum via a piece of sewing thread. Fibers images from representative pendulum tests are shown in **Figure 3.22** and details of the experiments and results are shown in **Table 3.1.** The fibers survive these tests surprisingly well. Films that appear to be cracked prior to testing generally survive, when the angle of travel reached 90°. These flaws may be surface features that do not affect adhesion at the fiber-composite interface.

Table 3.1. Mechanical testing results for fibers coated with 53.4 wt% **wlb34g-o** powder in binder.

Fiber	Binder Used (Aged 5 days)	Cure Parameters (°C, hours)	String, Tape, and Fiber Mass (kilograms)	Distance to Impact Point (meters)	Angle (degrees)	Impact Force (N)
A/B	55 mol% OtMOS/TEOS (ethanol)	70, 16.5	2.396×10^{-4}	0.225	90	1.24
C/D	55 mol% OtMOS/TEOS (ethanol)	70, 16.5	2.383×10^{-4}	0.263	30	0.480
E–H	55 mol% OtMOS/TEOS (ethanol)	70, 16.5	2.330×10^{-4}	0.263	30-90	1.30

3.3.7 High temperature survivability of $K_2Mo_6Cl_{14}$•$1H_2O$/sol–gel films.

The optical properties of sol–gel films embedded with $K_2Mo_6Cl_{14}$•$1H_2O$ were measured after being subjected to heating protocols where both temperature and time were varied. The measured luminescence intensity of the film in nitrogen and its quenching in air were used as an indication of the high-temperature survivability of each film.

The emission spectra in nitrogen of film **29L** and an acetonitrile solution of the potassium salt (**FJ-17**) used in the preparation of the film are shown in **Figure 3.23**. Film **29L** was dip coated three times using a 9-day old Mo-cluster/sol–gel solution, dried for 21 days under ambient conditions, and then cured for 24 hours at 70°C. The film was then aged in air at room temperature for 3 months. Using a variety of time and temperature combinations, film **29L** was annealed at 200°C for a total of 54 hours, with the emission spectra measured after each heating step. After subtracting the Raman scattering due to the sol–gel matrix it was found that the line-shape had not changed, confirming that sol–gel immobilization and thermal cycling did not adversely affect the emission of the potassium salt (**FJ-17**).

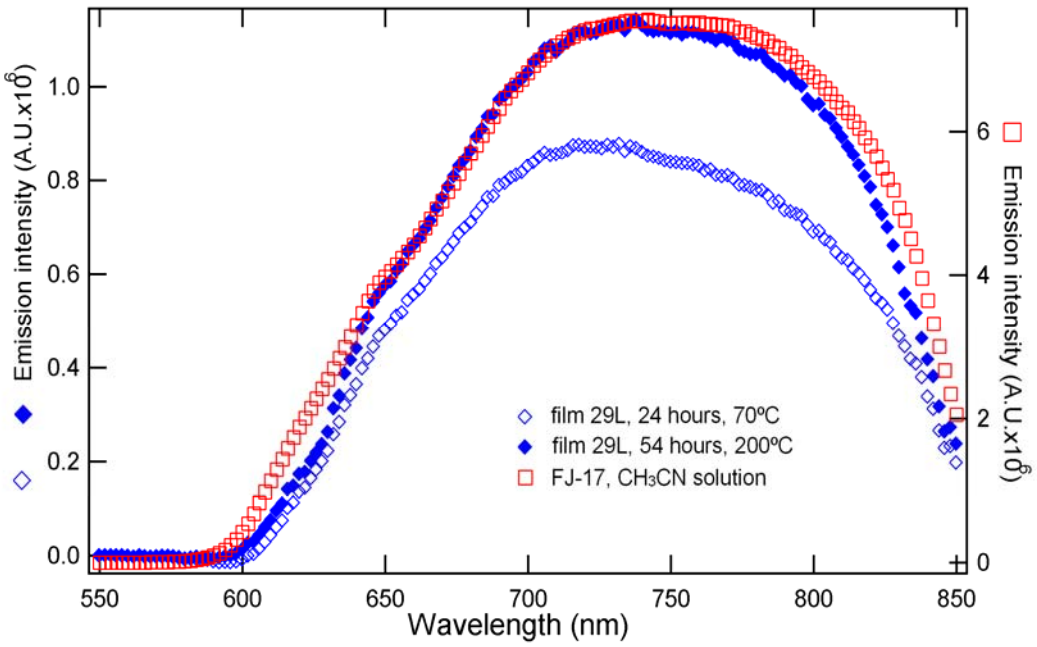

Figure 3.23. Room temperature emission spectra sol–gel film **29L** (◇) 1 day curing at 70°C, (◆) 54 hours of thermal cycling between 200°C, and the spectrum of its originating potassium salt **FJ-17** (□) in CH_3CN. All spectra were measured in 99.999% (v/v) nitrogen. The film concentration is 3.6 (±1.6) × 10^{21} cluster/cm^3 based on an estimated film thickness of 700 (±300) nm. The solution concentration is 0.087 mM (±1.4%). The data was obtained by the author in collaboration with R. N. Ghosh. Figure courtesy of R. N. Ghosh.

Shown in **Figure 3.24** is the emission intensity of film **29L** measured in nitrogen after each thermal cycle at 200°C. The data have been corrected for variations in the lamp intensity. Note that the luminescence intensity is nearly constant over the entire time interval, demonstrating the long-term stability of the cluster photophysics, even after extended aging at 200°C. However, the oxygen quenching ratio, defined as the ratio of the luminescence intensity in 99.999% (v/v) nitrogen to that in 21% (v/v) oxygen, decreased to 1.2 at the conclusion of the tests.

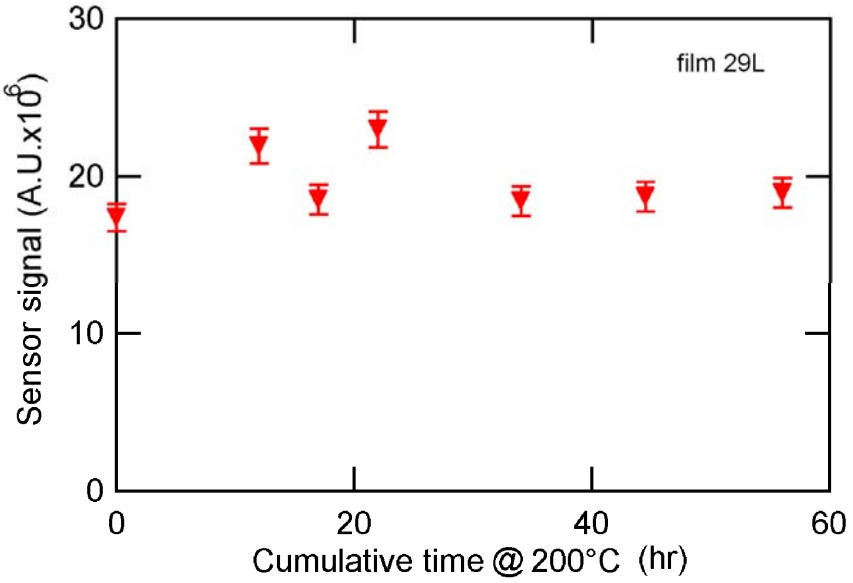

Figure 3.24. Integrated emission intensity (550 nm – 850 nm) from sol–gel film **29L** at room temperature, after heating at 200°C for the indicated time interval. See **Figure 3.29** for measurement information. The data was obtained by the author in collaboration with R. N. Ghosh. Figure courtesy of R. N. Ghosh.

3.4 CONCLUSIONS

Methods were developed for sol–gel film deposition on planar and optical fiber substrates by dip coating and spray coating. The mechanical properties of the films depended on the film thickness; thin films were stable, but cracks often formed in the thicker films needed for sensors. This problem was addressed using two strategies: altering the components of the sol–gel solutions used to embed the clusters and by devising a composite approach to sensing layers where a slurry of fully cured sol–gel particles containing $K_2Mo_6Cl_{14}•1H_2O$ in a sol–gel "binder" were deposited on substrates. The latter approach offers several advantages such as minimizing film shrinkage and hence, cracking, and the ability to use the same cluster/sol–gel source for a series of sensors leading to sensors with predictable characteristics. Films prepared from powdered sol–gel solutions showed promising results that corroborate the advantage of utilizing the composite approach to fabricate fiber sensors that have stable and predictable optical properties. Measurements of quenching ratios for planar substrates prepared by the composite route suggests a physical model where the cluster-containing particles form a continuous porous network analogous to a sintered glass that are highly permeable but mechanically and thermally stable.

REFERENCES

REFERENCES

[1] N. Docquier, S. Candel, *Progress in Energy and Combustion Science* **2002**, *28*, 107.

[2] A. W. Maverick, Ph.D. Dissertation, California Institute of Technology (Pasadena), **1982**.

[3] R. D. Mussell, Ph.D. Dissertation, Michigan State University (East Lansing), **1988**.

[4] M. D. Newsham, Ph. D. Dissertation, Michigan State University (East Lansing), **1988**.

[5] C. J. Ruud, Ph. D. Dissertation, Michigan State University (East Lansing), **1999**.

[6] M. D. Newsham, M. K. Cerreta, K. A. Berglund, D. G. Nocera, *Materials Research Society Symposium Proceedings* **1988**, *121*, 627.

[7] R. N. Ghosh, G. L. Baker, C. Ruud, D. G. Nocera, *Applied Physics Letters* **1999**, *75*, 2885.

[8] O. Stern, M. Volmer, *Physikalische Zeitschrift* **1919**, *20*, 183.

[9] T. Masuda, E. Isobe, T. Higashimura, K. Takada, *Journal of the American Chemical Society* **1983**, *105*, 7473.

[10] T. Masuda, B. Z. Tang, T. Higashimura, H. Yamaoka, *Macromolecules* **1985**, *18*, 2369.

[11] J. T. Remillard, J. J.R., B. D. Poindexter, C. K. Narula, W. H. Weber, *Applied Optics* **1999**, *38*, 5306.

[12] J. T. Remillard, B. D. Poindexter, W. H. Weber, *Applied Optics* **1997**, *36*, 3699.

[13] A. J. Monack, *Materials Research and Standards* **1970**, *10*, 26.

[14] S. Ujihashi, in *Science and Golf II: Proceedings of the 1994 World Scientific Congress of Golf* (Eds.: J. C. Alastair, F. Martin), Routledge (London), **1994**, 302.

[15] J. R. Roberts, R. Jones, S. J. Rothberg, *Sports Engineering* **2001**, *4*, 191.

[16] Fiberguide, in *Fiberguide Specification sheet for Superguide G ultraviolet-visible fiber with gold jacket*, Fiberguide Industries, Stirling, NJ, Website.

[17] C. McDonagh, P. Bowe, K. Mongey, B. D. MacCraith, *Journal of Non-Crystalline Solids* **2002**, *306*, 138.

[18] L. L. Hench, J. K. West, *Chemical Reviews* **1990**, *90*, 33.

[19] A. W. Maverick, J. S. Najdzionek, D. Mackenzie, D. G. Nocera, H. B. Gray, *Journal of the American Chemical Society* **1983**, *105*, 1878.

[20] J. C. Sheldon, *Nature* **1959**, *184*, 1210.

[21] J. C. Sheldon, *Journal of the Chemical Society* **1960**, 1007.

[22] Y. Tang, E. C. Tehan, Z. Y. Tao, F. V. Bright, *Analytical Chemistry* **2003**, *75*, 2407.

[23] R. M. Bukowski, R. Ciriminna, M. Pagliaro, F. V. Bright, *Analytical Chemistry* **2005**, *77*, 2670.

[24] D. J. Osborn III, G. L. Baker, R. N. Ghosh, *Journal of Sol-Gel Science and Technology* **2005**, *36*, 5.

Chapter 4 – High-temperature optical fiber oxygen sensors

4.1 INTRODUCTION

The sensor characterizations in this chapter were carried out by P. Zhang and R. Loloee in R. N. Ghosh's laboratory. Further information can be found in the unpublished article "Fiber optic oxygen sensing up tot 100°C using molybdenum chloride clusters embedded in a sol−gel matrix" submitted to Sensors & Actuators, and the manuscript "$K_2Mo_6Cl_{14}$ optical indicators embedded in sol−gel particles for oxygen sensing up to 100°C" submitted to Journal of Applied Physics (2014). Quenching of the fluorescence from organometallic compounds by oxygen has been used to develop a number of fiber sensors.[1-42] A major drawback of these organometallic indicators for energy plant applications is that the chromophores degrade over time, lack long term reliability, and have a limited operational temperature range, typically room temperature plus or minus 25°C. In Chapter 3, a room temperature fiber optic oxygen sensor that utilizes the emission from hexanuclear metal halide clusters such as Mo_6Cl_{12},[44] to detect oxygen in the 0.1% (v/v) to 20% (v/v) range was discussed. The simple schematic of the fiber optic oxygen sensor shown in **Figure 4.1** illustrates the key design elements.

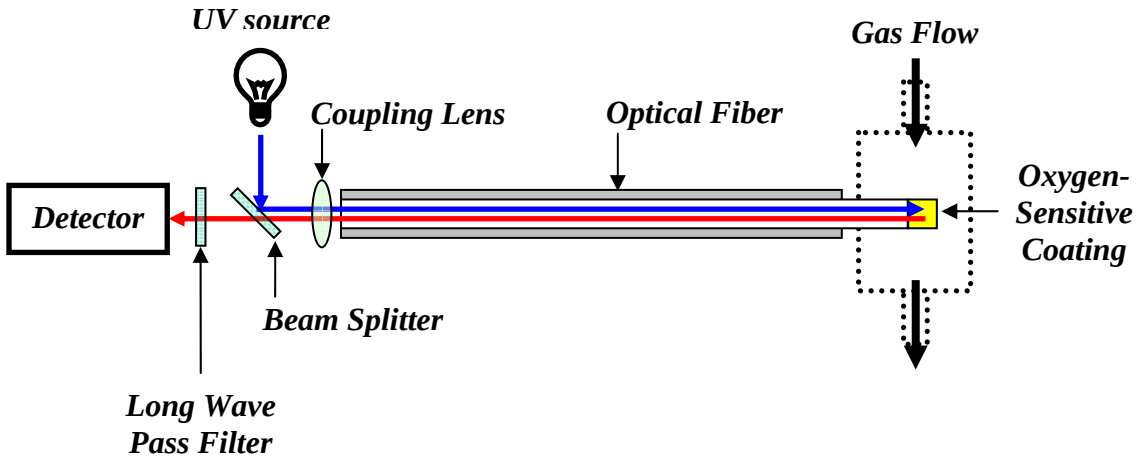

Figure 4.1. Schematic of the reflection mode fiber sensor. Adapted from a figure prepared by R. N. Ghosh.

First, the Mo_6Cl_{12} (Mo-cluster) was immobilized in an oxygen permeable matrix at one end of a silica fiber. Second, an ultraviolet optical source was coupled into the opposite end of the fiber and excited the clusters (excitation beam). Third, the reflected emission signal was also collected from the source end of the fiber. This geometry allows for the chemically sensitive end of the fiber sensor to be immersed in a harsh environment, while the excitation and collection optics are located in a more benign environment. Because the cluster is stable in air over extended periods of time at ~ 250°C, it should be possible to fabricate an optical fiber oxygen sensor which operates at temperatures that are much higher than current optical fiber oxygen sensor technology. The challenge is to overcome the temperature limitations of the polymer support matrix.[45, 46]

In this Chapter, several optical fiber sensors are fabricated and characterized in terms of mechanical stability, sensitivity, and repeatability at temperatures ranging from room temperature to >100°C, with its primary limitations being related to the stability of the cluster at temperatures in excess of 250°C.

4.2 EXPERIMENTAL

4.2.1 Materials.

Ethanol (Koptec, anhydrous, USP) and hydrochloric acid (Columbus Chemical Industries, electronics grade) were used as received. Water used was either reverse osmosis (in-house) or deionized using a Millipore purification system (Milli-Q, 18 MΩcm). Acetonitrile (Spectrum Chemical Company, HPLC grade and EMD Chemicals, OmniSolv) was dried overnight using activated molecular sieves (Spectrum Chemical, 1/16" pellets, type 4 Å) and then distilled from CaH_2 (Spectrum Chemical, anhydrous, desiccant, 40–20 mesh) prior to use. Sodium hydroxide pellets (Mallinckrodt, AR (ACS), lot C41P01), potassium hydroxide pellets (Jade Scientific, ACS Reagent), concentrated sulfuric acid (Fisher Scientific, Reagent grade or Columbus Chemical Industries, ACS/Reagent grade), and H_2O_2 (Fisher, 30%) were used as received. All glassware used for spectroscopic measurements was cleaned by soaking in concentrated hydrochloric acid, scrubbed with water and Alconox soap, rinsed with reverse osmosis water, and then oven-dried prior to use. Tetraethyl orthosilicate (TEOS) (Aldrich, 99.999%), *n*-octyltrimethoxysilane (OtMOS) (Aldrich, 96%), *n*-propyltrimethoxysilane (PtMOS) (Gelest, 98%), triethoxy(octyl)silane (OtEOS) (Aldrich, ≥96%), and (3,3,3-trifluoropropyl)trimethoxysilane (TFP-tMOS) (Gelest, >95%) were used as received. Fibers

were purchased from 3M (FP-1.0-UHT) and Ceramoptec (PUV 1000/1300N). Prior to coating, fibers were washed with Alconox, rinsed with distilled water, soaked in a base bath (~5M NaOH in 95% ethanol), rinsed with distilled water, and stored in distilled water until use and were handled with gloves in order to minimize surface contamination.

4.2.2 Synthesis of cluster-containing sol–gel particulates.

Sol–gel solutions **29**, **31**, and **34g-o** containing $K_2Mo_6Cl_{14}$•$1H_2O$ were prepared as described in chapter 3 then aged in sealed scintillation vials for 4–7 months at room temperature to form solid monoliths. The monoliths were ground using a mortar and pestle (abbreviated **mp**) and then cured at 70°C for 5 days to complete the sol–gel reaction and minimize further densification of the sol–gel matrix to produce the larger (~250 μm) **mp29**, **mp31**, and **mp34g-o** particles. Pulverizing **mp29** and **mp34g-o** for 15 minutes using a small stainless steel Wig-L-Bug ball mill (abbreviated **wlb**) from Bratt Tech, Inc. produced the smaller (1 – 8 μm) **wlb29** and **wlb34g-o** particles. The initial $K_2Mo_6Cl_{14}$•$1H_2O$ concentration of sol–gel solutions used to prepare **mp31**, **wlb29**, and **wlb34g-o** particulates was 8.6×10^{-3} M, 2.2×10^{-3} M, 2.3×10^{-3} M respectively.

4.2.3 Preparation of fiber M, (TEOS binder and mp31).

A light yellow paste containing 60 w/w% particle:binder was prepared by adding a known mass of TEOS-based sol–gel solution aged at room temperature for 70 days to a predetermined mass of **mp31** powder. The paste was mixed with gentle grinding in a small vial to increase homogeneity. A clean dry fiber was then dipped at an angle of 15° and hung vertically for 1

hour to achieve a uniform coating and pre-dry the film. The pre-dried film was cured at 70°C for 12 hours.

4.2.4 Preparation of fiber 45, (55 mol% OtMOS/TEOS and wlb29).

A off-white paste containing 53.2 w/w% particle:binder was prepared by adding a known mass of 55 mol% OtMOS/TEOS based sol–gel solution aged at room temperature for five days to a predetermined mass of **wlb29** powder. The paste was mixed with gentle grinding in a small vial to increase homogeneity. A clean dry fiber was then dipped at an angle of 15° and hung vertically for 1 hour to achieve a uniform coating and pre-dry the film. The pre-dried film was cured at 70°C for 16 hours.

4.2.5 Preparation of fiber 121, (55 mol% OtMOS/TEOS and wlb34g-o powder).

An off-white paste containing 54.9 w/w% particles:binder was prepared by adding 0.0652 g of **wlb34g-o** particles to 0.0536 g binder solution that had been aged for 5 days at room temperature. The paste was mixed with gentle grinding in a small vial to increase homogeneity. A clean dry fiber was then dipped at an angle of 15° and hung vertically for 1 hour to achieve a uniform coating and pre-dry the film. The pre-dried film was cured at 70°C for 16 hours.

4.2.6 Preparation of fiber 70, (55 mol% OtMOS/TEOS and wlb34g-o powder).

An off-white paste containing 53.4 w/w% particle:binder was prepared by adding a known mass of 55 mol% OtMOS/TEOS based sol–gel solution aged at room temperature for five days to a predetermined mass of **wlb34g-o** powder. The paste was mixed with gentle grinding in a small

vial to increase homogeneity. A clean dry fiber was then dipped at an angle of 15° and hung vertically for 1 hour to achieve a uniform coating and pre-dry the film. The pre-dried film was cured at 70°C for 16.5 hours.

4.2.7 Thermal aging of cluster-containing films.

The experimental details for the thermal aging of samples can be found in the experimental section of chapter 3.

4.2.8 Optical microscopy of samples.

The details concerning the optical microscopy of samples can be found in the experimental section of chapter 2.

4.2.9 Fiber optic oxygen sensor characterization system.

The response of fiber sensors to step changes in oxygen from 2% (v/v) to 21% (v/v) O_2 at temperatures between 23°C and 102°C was measured using a flow through system shown in **Figure 4.2**. Measurements on fibers **M** and **45** utilized a hand-switched gas divider while measurements for fibers **121** and **70** were improved by replacing the hand-switched system with a Horiba gas divider (SGD-710C) upstream of the gas inlet into the quartz chamber for precise (± % (v/v)) control over the oxygen concentration. The Horiba gas divider allows delivery of a precise gas stream, within ±0.5% of the component gas (0.1% (v/v) O_2) to the sensor.

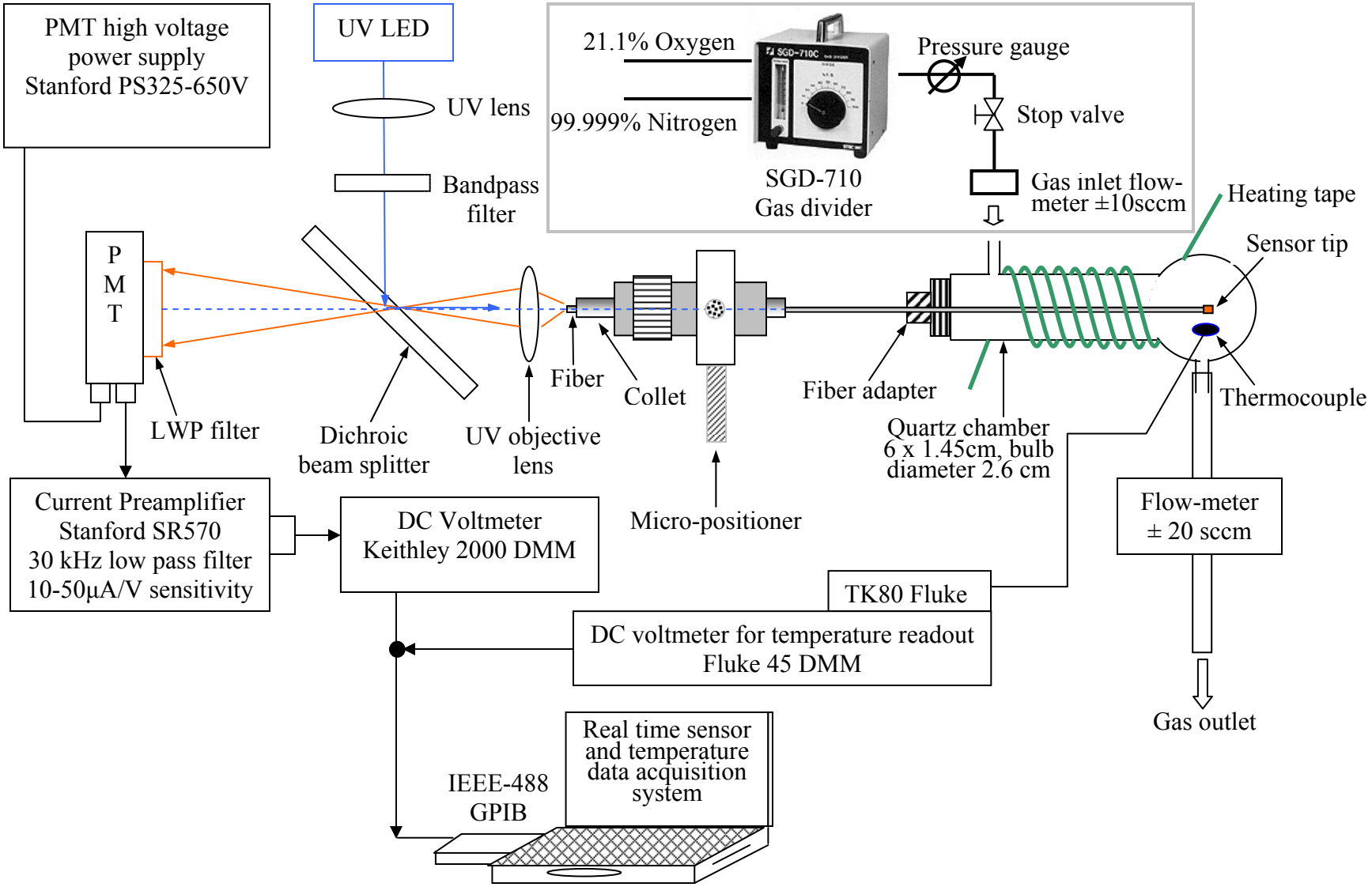

Figure 4.2. Apparatus for semi-automated high-temperature fiber optical oxygen sensor characterization system, for details see text. Figure courtesy of P. Zhang, R. Loloee, and R. N. Ghosh.

The automated high-temperature reflection-mode fiber optic sensor characterization set-up uses a specially designed quartz "furnace" to heat the tip of the fiber sensor up to ~110°C and monitor the temperature to within ±2°C using a thermocouple placed 1–2 mm near sensor tips. The gas flow in this flow-through cell is 300 – 400 mL/min. By monitoring both the inlet (±10 sccm) and outlet (±20 sccm) flows, we estimate a gas exchange time 10s for the system. The LabVIEW® program was used to simultaneously monitor the sensor signal and sensor temperature. The excitation source (UV Nichia LED, part# NSHU590B) intensity for the sensor measurements is ~700 μW at 365 nm. Using the dichroic beam splitter and the OFR UV objective lens (LLU-13-20-NUV, f = 20.0 mm, diameter = 12.5 mm, NA = 0.476, bandwidth 325 – 500 nm, average reflectance <0.5%) ca. 300 μW is coupled into the multimode fiber (1mm core diameter). The reflected phosphorescence (590 nm – 850 nm) from the tip of the fiber sensor is detected by a Hamamatsu R955 photomultiplier tube (PMT) with the output signal routed to a Stanford SR570 current pre-amplifier with a gain of 20 μA/V. A 45° dichroic beam splitter and a 590 nm long wave pass (LWP) filter are used to separate the excitation and signal beams. A 1 V signal at the voltmeter corresponds to ~1 nW of phosphorescence signal from the fiber sensor. In addition, the "unwanted" light in the emission bandwidth that reaches the detector is estimated at 1/160 the level of the smallest sensor signal in oxygen.

The entire optical path from the UV LED to the detector is aligned on a *single* optical bench, which has the following advantages. The first advantage is the ability to make meaningful long term (over several days) sensor measurements because of the stability of both the excitation power and also the manor in which it is coupled to the fiber sensor and the coupling of the output

sensor signal to the detector. The second advantage is the ability to remove a fiber sensor from the measurement system and reinstall it reproducibly. Repeatability of the LED-to-fiber coupling of better than 1% is achieved, which allows for meaningful comparisons between individual sensors. Beginning at the UV source, the UV LED, the collimating lens (f =20 mm, NA = 0.476) and a UV bandpass filter were placed inside a single stackable lens tube. This arrangement ensures the concentricity of all three components along the optical axis. The output UV beam is collimated with a 25% variation in the beam size at a distance of 6 cm. The purpose of the UV bandpass filter (Semorock FF01-377/50-25 351/405), which has a 93% transmission between 351 nm and 405 nm, is to reduce the unwanted visible light from the UV LED that reaches the detector (**Figure 4.3**).

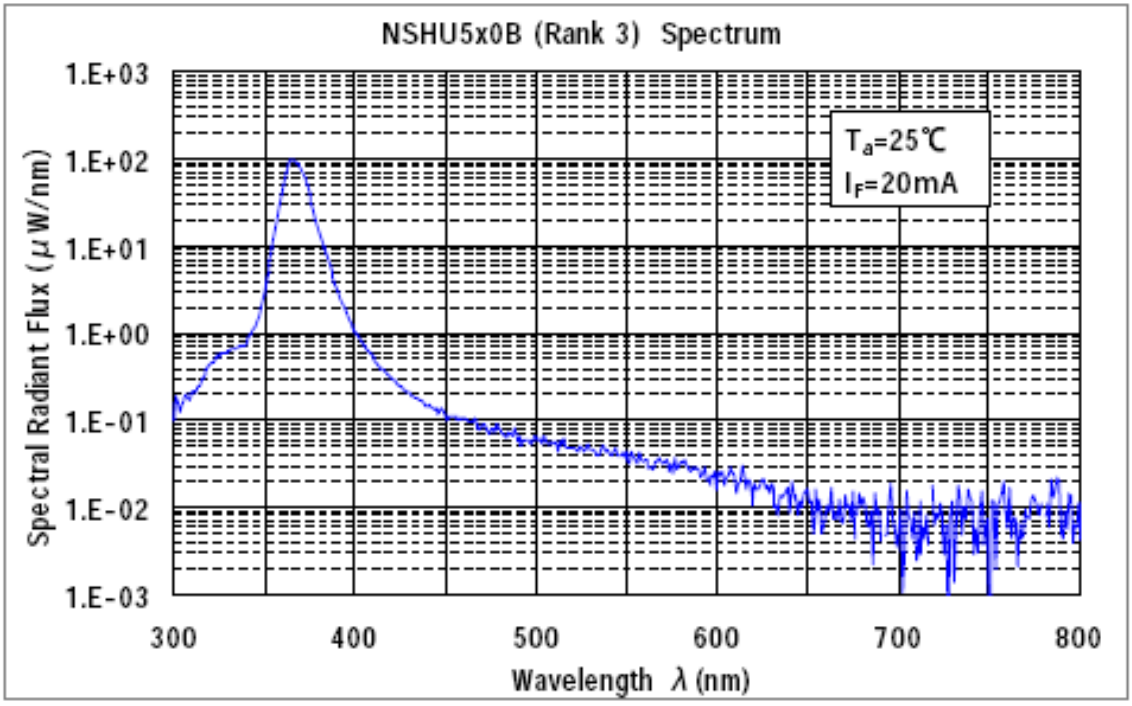

Figure 4.3. UV LED spectrum taken from the Nichia company data sheet.[43] There is 2 μW of unwanted visible signal from the LED itself in the emission bandwidth of the Mo-clusters. Figure courtesy of R. N. Ghosh.

Since the visible output from the UV LED is within the emission bandwidth of the Mo clusters, 600 nm – 800 nm, it is spectroscopically indistinguishable from the real sensor signal and limits the smallest signal that can be detected. The integrated power output of the LED is about 2 μW in wavelength range of 600 nm–800 nm based on the output spectrum of the UV diode. Without the Semrock visible rejection filter, this diode output results in a spurious signal of ~0.4 nW at the PMT. **Table 4.1** lists the transmission and reflection parameters for all the relevant optical components.

As shown in **Figure 4.4** the transmission through the Semrock bandpass filter is 93% in the UV and an average of 5×10^{-5} for 600 nm–700 nm and 3×10^{-3} for 700 nm–900 nm. The unwanted background from the LED should now be only 0.002 nW based on calculations. The measured transmission through an optical fiber coated with sol–gel coating without any Mo-cluster, was measured to be about 0.01 nW. This was a PUV fiber with clusterless sol–gel particles in a TEOS/OtMOS sol–gel binder, which mimics a real sensor structure. The measured intensity in emission bandwidth that is 30 times smaller than the intensity in oxygen. A black plastic enclosure now covers the entire optical path and our signal-to-noise ratio is improved 4× compared to our original characterization system.

Table 4.1. Reflectance and transmission in visible range for all the optical components used in the system shown in Figure 4.2. For 2 μW of Nichia UV LED power at 750 nm, the emission maximum, 0.002 nW of power is obtained at the PMT detector. Data and table courtesy of P. Zhang and R. N. Ghosh.

	Band-pass filter	Dichroic beam splitter	Lens-fiber coupling	Fiber-Fresnel reflection (air)	Dichroic beam splitter	Fiber-lens coupling	High-pass filter
	700-800 nm	~750 nm (Est.)	(Est.)	(Est.)	~750 nm (Est.)	(Est.)	>590 nm
Transmission	3.4×10^{-3}	--	0.4	--	0.97	0.50	0.92
Reflectance P = 2μW		0.03		0.04			

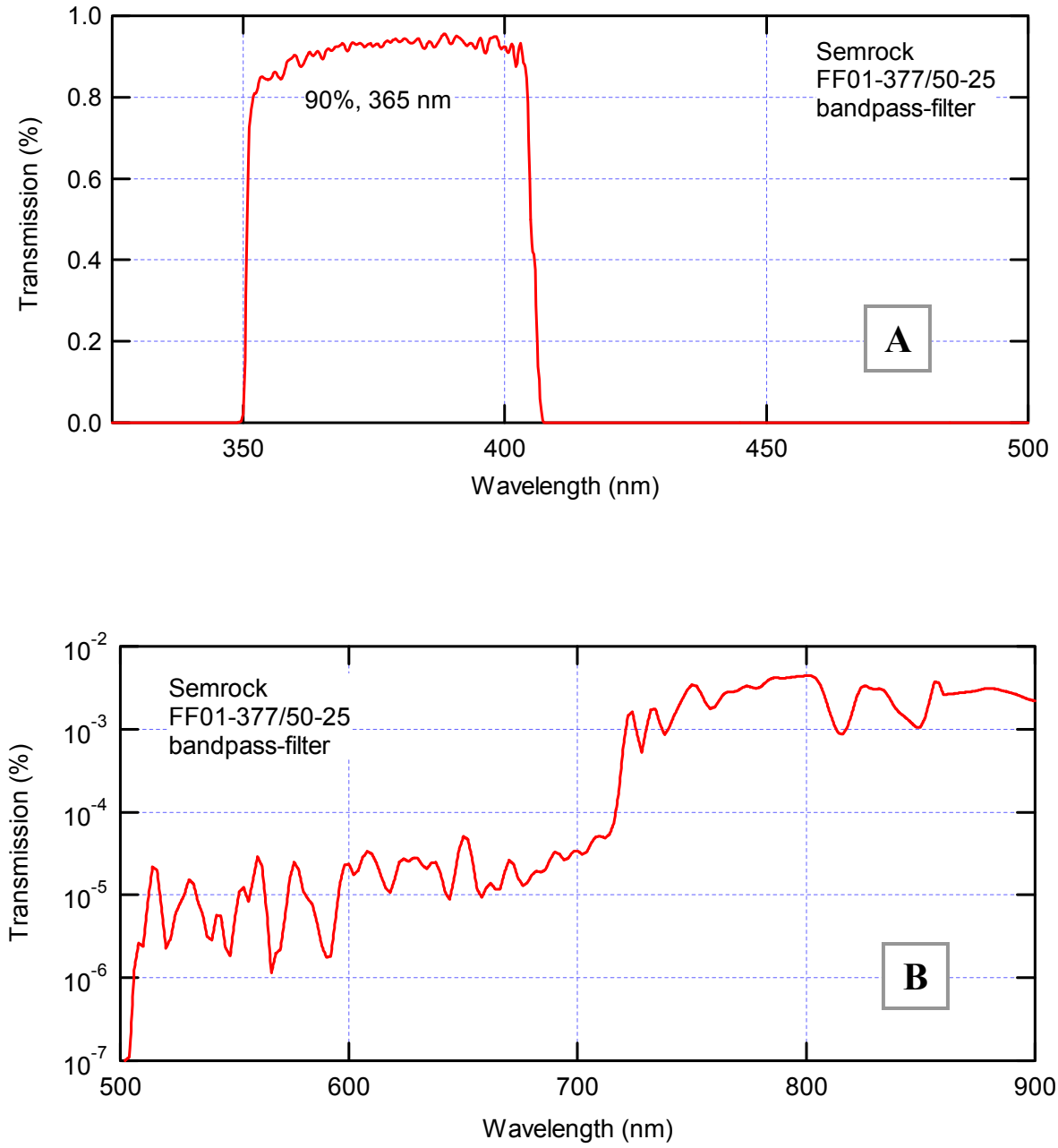

Figure 4.4. The Semrock (FF01-377/50-25) band-pass filter spectrum, (A) with a UV bandwidth 352 nm – 403 nm and 93% transmission, (B) enlarged spectrum in the range 500–900 nm, transmission 1×10^{-7} to 4×10^{-2}. The filter is used to remove the visible wavelengths from the Nichia UV LED output. Figure courtesy of P. Zhang and R. N. Ghosh.

4.2.10 Gas Divider.

A gas divider system shown in **Figure 4.5** was constructed to accurately prepare oxygen mixtures for the flowing gas stream experiments.

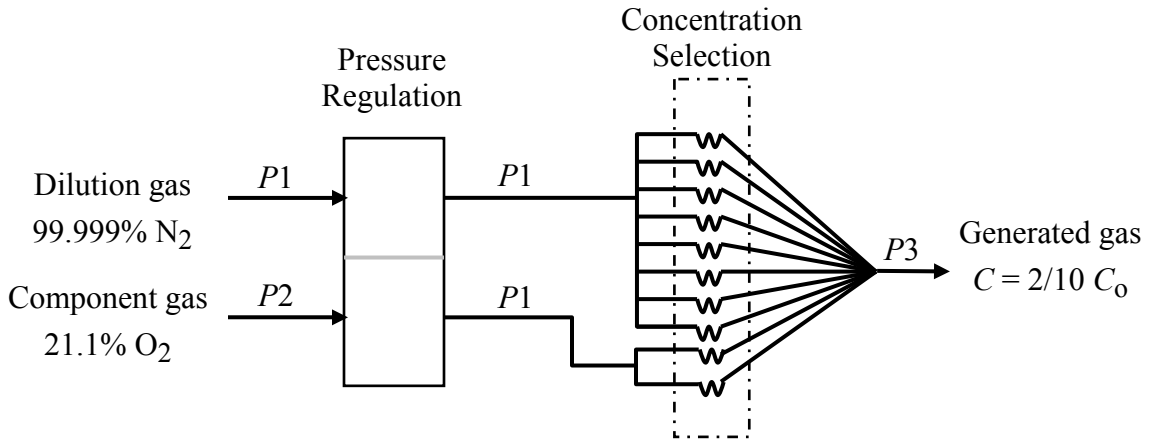

Figure 4.5. Schematic of the Horiba SGD-710 gas divider operating principles. The abbreviations for pressure and concentration are represented by *P* and *C* respectively. Figure courtesy of R. Loloee.

The Horiba gas divider (SGD-710C) mixes 21.1% (v/v) oxygen (component gas) with 99.999% (v/v) N_2 (dilution gas). The precision of the gas divider is 0.5% of the component gas, i.e. 0.1% (v/v) O_2 in our case, with a repeatability of 0.2% of the component gas. The gas divider consists of 10 identical capillary tubes. A mechanical switch sets the number of capillaries used for the component and dilution gas, such that the generated gas of concentration *C*, is given by $C = (m/10)C_o$, where C_o is the concentration of component gas (oxygen), and m is the number of capillaries in which component gas flows. The inlet pressure of the capillary tubes is controlled by a pressure regulating system which is precisely designed to allow the pressure of a component

gas (O_2) to remain same as that of a dilution (N_2) gas. The generated flow rate then depends upon on the pressure of the dilution gas which is set at 5 psi and has a total pressure of 10 psi.

When the measurement required only two preset oxygen levels, the gas divider was replaced with a 3-way solenoid valve (Cole-Parmer Inc., EW-98302-42) that automatically switched between the two gases. The time duration of each gas pulse can be set by the switch controller. This system allows long-term gas cycling measurements with flow rates from 100 – 1000 sccm.

4.2.11 Molar oxygen concentration [O_2].

The ideal gas law is used to calculate the molar oxygen concentration in the flow through cell at a given temperature T and pressure P:

$$PV = nRT$$

Hence, molar oxygen concentration $[O_2] = n/V = P/(RT)$. Where n is the number of moles of the gas, $R = 8.2057 \times 10^{-2}$ L•atm/mol•K is the universal gas constant, and T is the temperature in Kelvin. The measured pressure P in our flow through cell is 10 psi or 0.6803 atm. For a given oxygen fraction F (where $F = 1$ for 100% (v/v)) the molar oxygen concentration is:

$$[O_2] = n/V = 8.29F/T$$

A number of measurements were performed to characterize the optical performance of the overall system. First, the stray light level of the system was evaluated. With only the PMT and current preamplifier turned on, a 0.0005 nW signal was measured. Second, after turning on the excitation LED without an optical fiber in the path, the signal increased to 0.13–0.15 nW, which sets an upper bound on the *smallest* sensor signal detectable. As the UV rejection ratio of the 590 nm LWP filter in front of the PMT is very high, essentially none of the excitation signal can be scattered back into the detector, so the 0.15 nW signal must be due to visible fluorescence in the optical path. Potential sources of this fluorescence are being investigated in order to eliminate it. Third, the output signal from bare 1000-µm fibers of various lengths (no cluster on the fiber tip (see **Figure 4.6**) was measured.

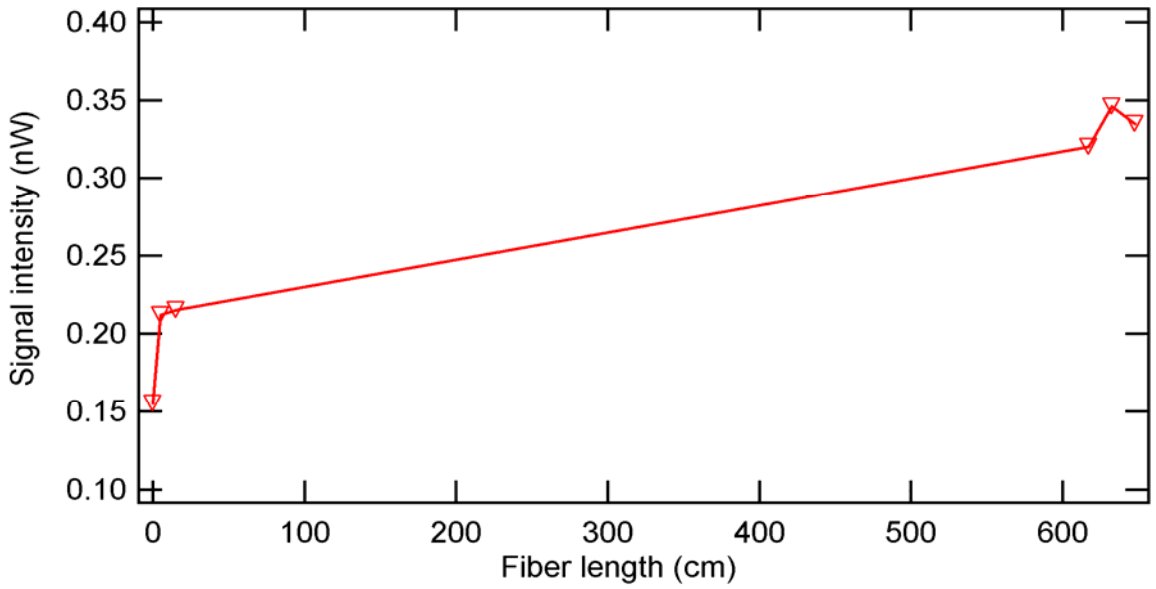

Figure 4.6. Signal from an uncoated optical fiber as a function of fiber length. The data show low autofluorescence (2.1×10^{-4} nW/cm). However, there is a 0.07 nW signal (bandwidth: 590 nm–900 nm) due to reflections off the front and back faces of the fiber. Figure courtesy of R. N. Ghosh.

For a short fibers, an additional 0.07 nW is added due to scattering from the front and back faces of the fiber. The autofluorescence of the fiber itself is low, 2.1×10^{-4} nW/cm. For a fiber sensor operating at 100°C, the signal to noise is ~4 dB in 21% (v/v) oxygen.

4.2.12 Sensor data acquisition and measurement.

For real time applications, a technique to monitor the signal from the fiber optic sensor as a function of both temperature and time is needed. With Mr. Nate Vehanovitz (Troy Inc.), a Labview program for sensor data acquisition and temperature monitoring was developed. The hardware requirements are a laptop running Windows XP or 2000 equipped with a PCMCIA-GBIP card from National Instruments, a GPIB cable, a Keithley digital multimeter (DMM) and Fluke 45 voltmeter **(Figure 4.7).** During fiber sensor measurements, the Keithley voltmeter monitors the sensor signal (a voltage proportional to the emission intensity) while the Fluke DMM monitors the temperature output from a k-type thermocouple and 80TK readout module. The front panel of the data acquisition program is shown in **Figure 4.8**.

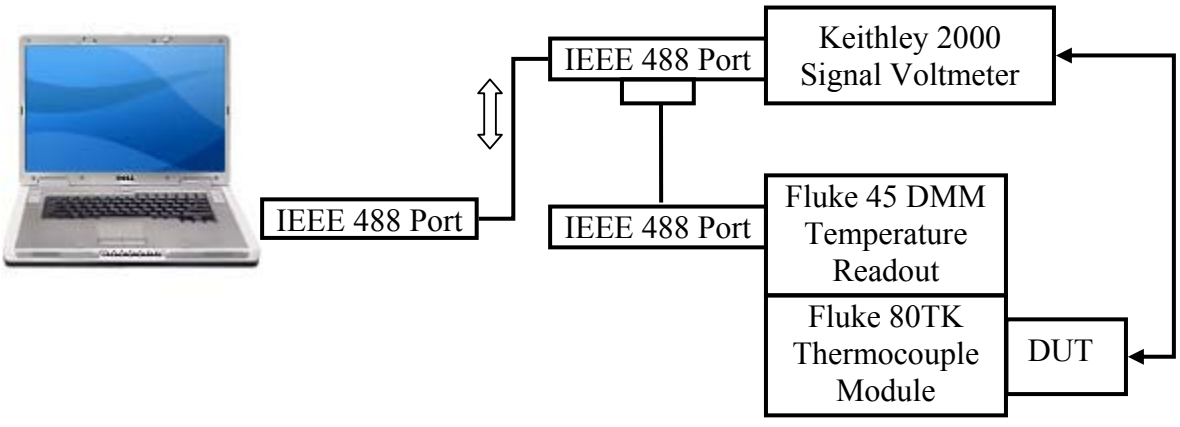

Figure 4.7. Block diagram of the sensor and temperature data acquisition system. Figure courtesy of P. Zhang and R. Loloee

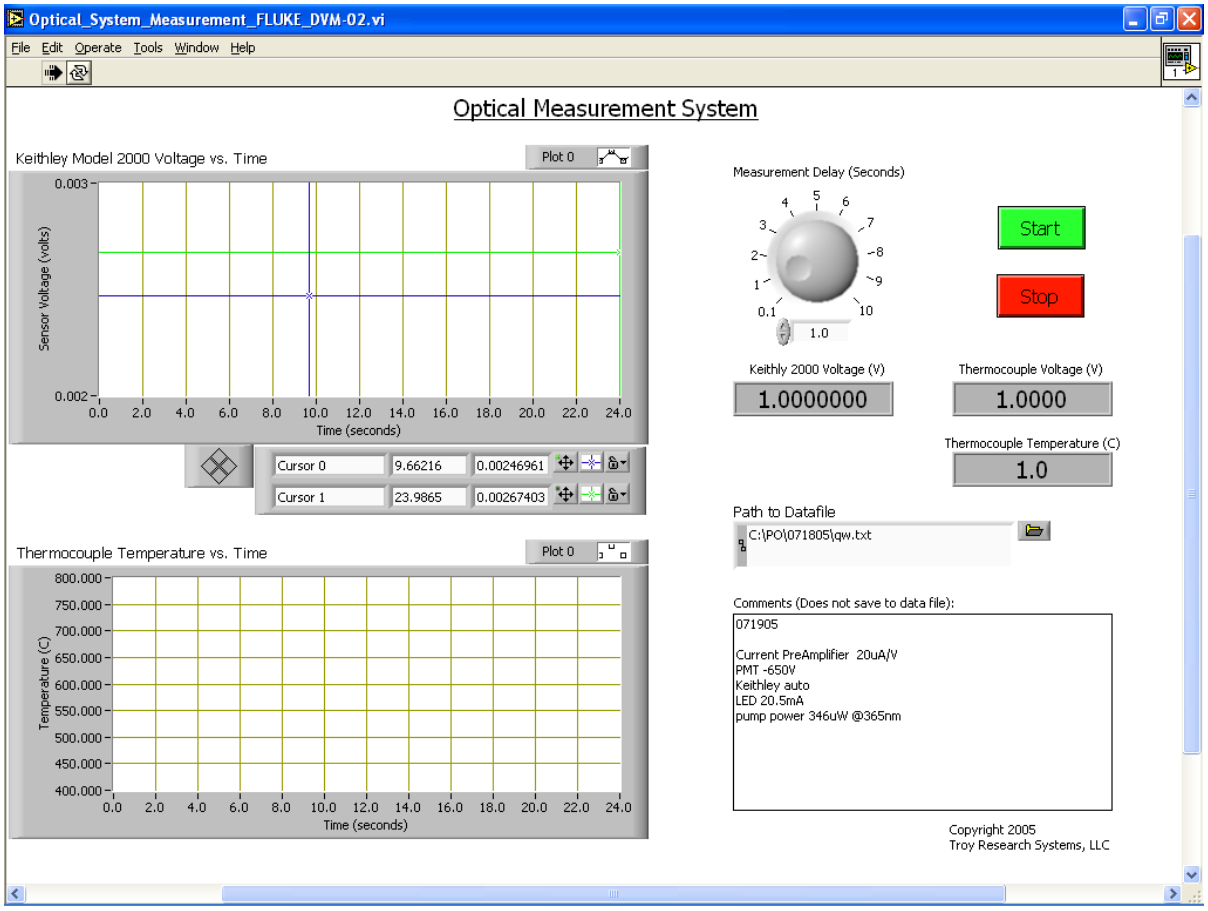

Figure 4.8. User interface of the automated optical sensor data acquisition software OMS_02.exe. Figure courtesy of N. Verhanowitz.

The data are displayed on an oscilloscope-like screen during real time measurements (see **Figure 4.8**). The user can save data to a specified data-file. The user can also record experimental condition in comments window and set a continual sampling rate by adjusting a knob on right-up window. Two plotting windows on the left display record the sensor signal and temperature, respectively. The cursors can be moved during the course of the measurement to provide real-time output of signal amplitude and time. The program generates one data file (.txt) with the output data in tab-separated columns.

4.3 RESULTS AND DISCUSSION

4.3.1 High-temperature fiber sensor measurements

Figure 4.9 shows a micrograph of one of the first successful fiber sensors, fiber **M**, prepared using a sol–gel binder to immobilize sol–gel particles embedded with $K_2Mo_6Cl_{14}$•$1H_2O$. Fiber **M** is a fiber sensor with large particles using a TEOS binder with 4×10^{18} clusters/cm^3 in the composite, which formed a ~100-μm thick hemispherical cap on the end of the fiber.

Figure 4.9. Micrograph of fiber **M**.

The sensor was characterized in the measurement setup shown in **Figure 4.2** under the following conditions. First, using a 900 μW 365 nm LED as the excitation source, we were able to obtain a net coupling efficiency of 33% by coupling 295 μW of UV power into the optical fiber. Second, the gas flow rate was maintained at ~1000 sccm. Third, the temperature of the fiber sensor was monitored continuously with a thermocouple to ±1°C. During the course of each measurement, the maximum temperature drift was ~3°C over 30 minutes.

The oxygen sensing characteristics of fiber **M** are shown in **Figures 4.10 – 4.16**. The results span the temperature range of 23°C to 100°C**.** The first goal was to determine if elevated temperatures adversely affect the sensitivity of sensor by examining the sensor output in pure nitrogen and synthetic air (21% (v/v) oxygen, balance nitrogen) which are the end points of our concentration range. **Figures 4.10 – 4.16** show the sensor response to alternating pulses of 99.999% (v/v) nitrogen and 21.1% (v/v) oxygen at 100, 81, 60, 41 and 23°C respectively. The signal intensity in nitrogen is stable over the entire temperature range, 2.8 ± 0.2 nW or a variation of ±7%. **Figure 4.15** shows that the sensor signal is relatively unaffected by a ramp up, followed by a ramp down in temperature.

The quenching ratio, or the signal in pure nitrogen divided by that in 21% (v/v) oxygen, is a measure of the sensitivity of the sensor. It was found that the quenching ratio increases from 4.4 to 6.9× from room temperature to 72°C, and then decreases slightly to 6.2× at 100°C (see **Figure 4.10**). The temperature dependence of the quenching ratio is due primarily to the temperature sensitivity of the sensor signal in oxygen. It was previously shown that the quenching ratio ($I_{oxygen}/I_{nitrogen}$) of the potassium salt in solution, following 4 hours of heating at 200°C was 13.2× and it is a reasonable to be able to reach half that value for the clusters immobilized in the matrix. The temperature dependence of the sensor a reversible process may be due to a temperature dependent permeability of oxygen in the sol–gel matrix or that the physical structure of the sol–gel binder matrix is continuing to evolve with heat cycling.

The absolute magnitude of our sensor signal is very encouraging in terms of practical implementations of our device. A ~3-nW output signal is obtained for ~300 μW of incident excitation power – 10^{-5} is very reasonable power conversion efficiency for a fiber sensor. Autofluorescence, the magnitude of the signal in our measurement bandwidth due to fluorescence from a length of fiber without any cluster on the tip, sets a lower limit on the smallest signal we can detect from our sensor. For a 15 cm long fiber sensor, there is 0.011 nW of autofluorescence, which is a factor of 40 smaller than the ~0.4 nW signal in oxygen.

Fiber **M** was thermally cycled above room temperature for a cumulative 7 hours in either nitrogen or oxygen. In addition the cluster containing sol–gel composite at the end of the fiber tip was exposed to a total of at least 15 days of 365-nm UV radiation in laboratory air. Following the series of experiments shown in **Figures 4.10 – 4.16**, we found that the bulk of the cluster containing sol–gel composite had delaminated from the fiber tip; however a thin sol–gel film still remained on the tip. As discussed in chapter 3, delamination is a result of sol–gel binder shrinkage during the curing process, so a portion of the TEOS binder was replaced with OtMOS. The results from optical and mechanical characterization of the fibers prepared with this technique are quite promising, as shown by the following data from fibers **M**, **45**, **70**, and **121**. At 60°C the cluster/sol–gel composite continues to adhere to the end of the silica fiber and the signal level in pure nitrogen is 4 nW, slightly higher than that for fiber **M**.

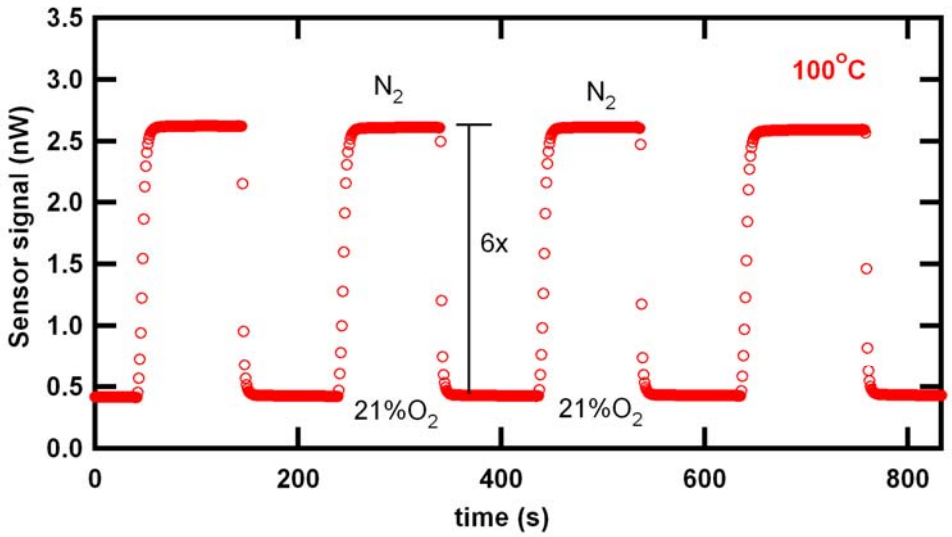

Figure 4.10. Fiber sensor measurements at 100°C demonstrating quenching by a factor of 6.1× between pure nitrogen and 21% oxygen (balance nitrogen). The sensor signal is large, in the nanowatt regime, with the signal magnitude in oxygen ~40 greater than the measured autofluorescence. The luminescent tip contains $K_2Mo_6Cl_{14}$•$1H_2O$ sol–gel particles embedded in a sol–gel binder matrix, with 4×10^{18} clusters/cm^3 (fiber **M**). The coupled excitation power is 295 W at 365 nm and the gas flow rate is 1000 sccm. Figure courtesy of R. N. Ghosh.

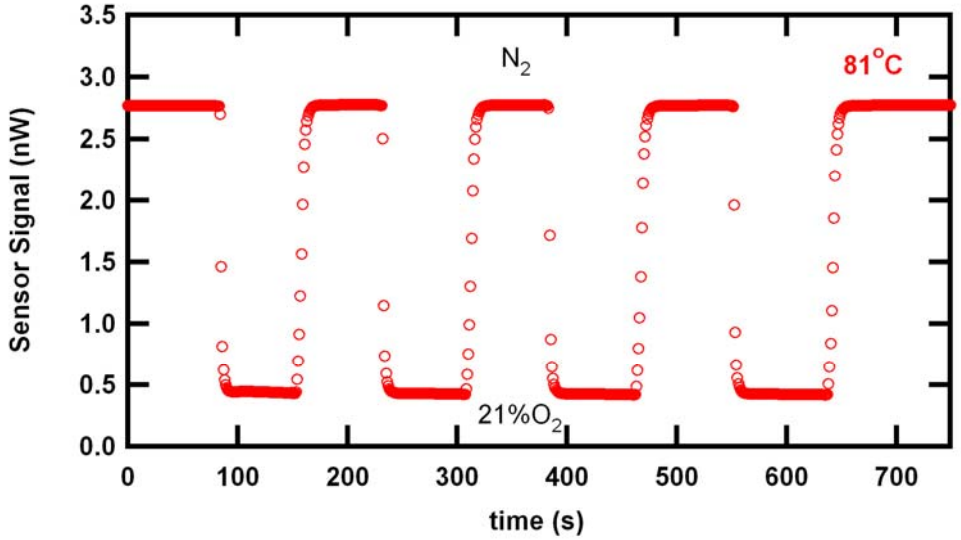

Figure 4.11. Fiber sensor measurements at 80°C demonstrating quenching by a factor of 6.4× between pure nitrogen and 21% oxygen (balance nitrogen) for fiber **M**. The measurement conditions are the same as **Figure 4.10**. Figure courtesy of R. N. Ghosh.

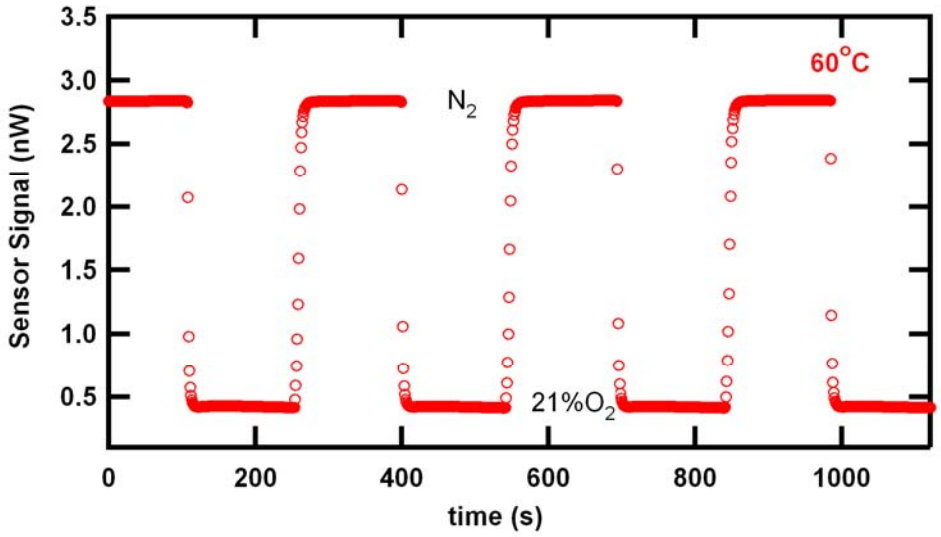

Figure 4.12. Fiber sensor measurements at 60°C demonstrating quenching by a factor of 6.8× between pure nitrogen and 21% oxygen (balance nitrogen) for fiber **M**. The measurement conditions are the same as **Figure 4.10**. Figure courtesy of R. N. Ghosh.

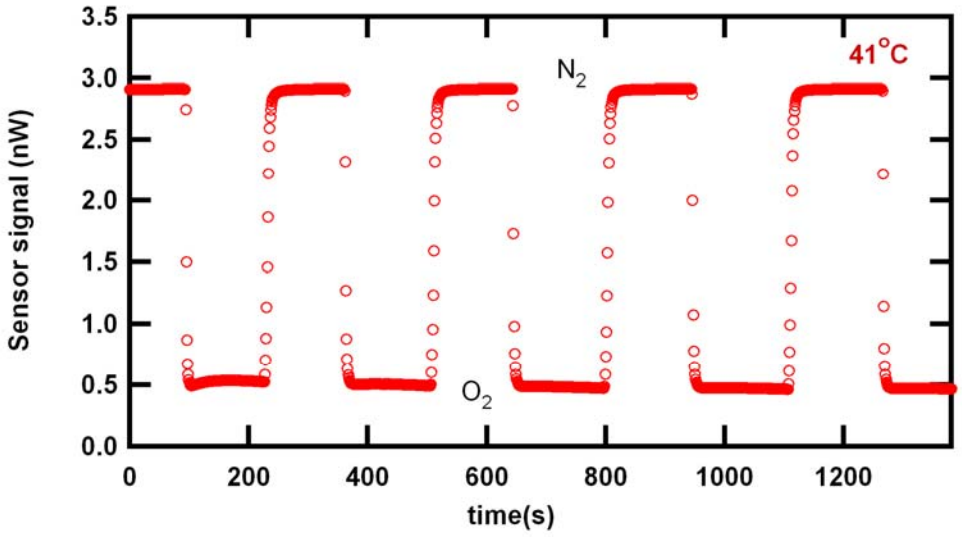

Figure 4.13. Fiber sensor measurements at 41°C demonstrating quenching by a factor of 5.9× between pure nitrogen and 21% oxygen (balance nitrogen) for fiber **M**. The measurement conditions are the same as **Figure 4.10**. Figure courtesy of R. N. Ghosh.

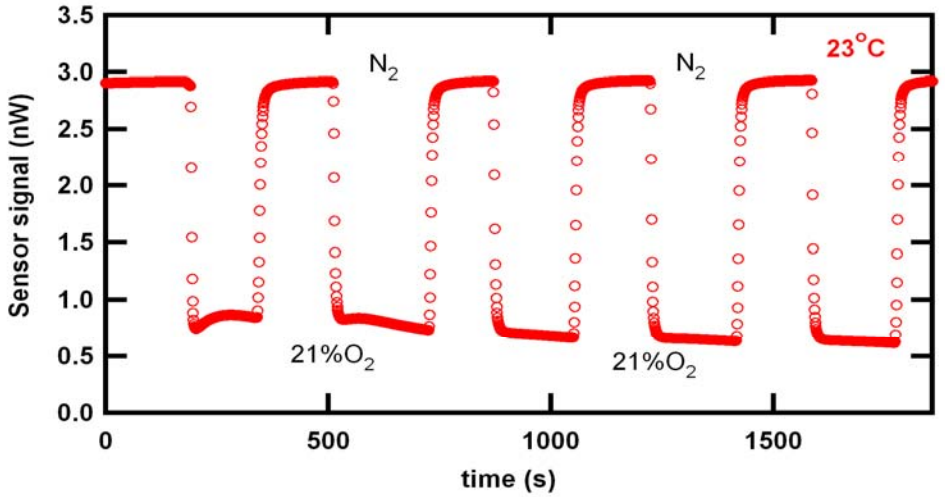

Figure 4.14. Fiber sensor measurements at room demonstrating quenching by a factor of 4.4× between pure nitrogen and 21% oxygen (balance nitrogen) for fiber **M**. The measurement conditions are the same as **Figure 4.10**. Figure courtesy of R. N. Ghosh.

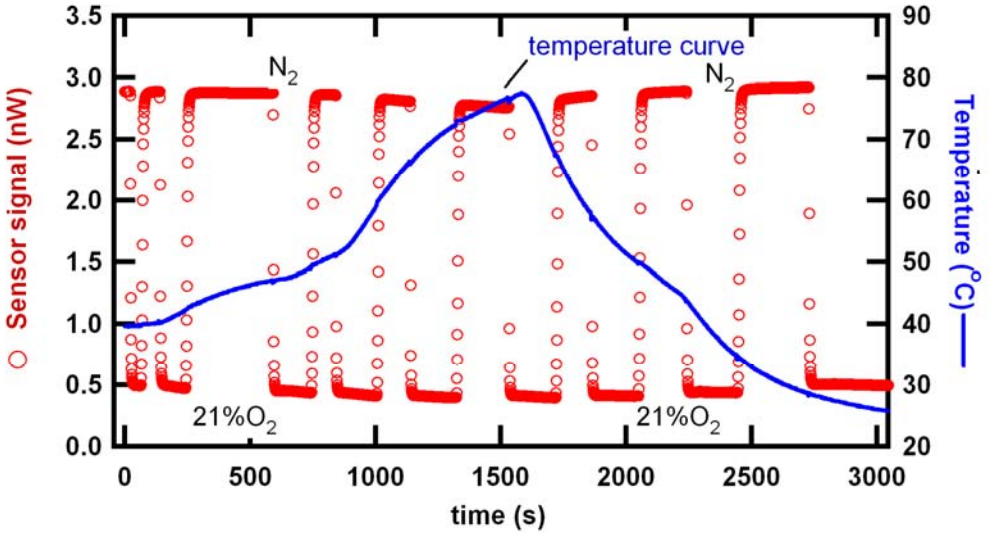

Figure 4.15. Fiber sensor measurements while scanning the temperature from 23 to 76°C and then back down to 23°C for fiber **M**. The data demonstrate that the sensor signal is relatively unaffected by the temperature ramp; the signal magnitude in nitrogen decreases by 5% from 23 to 76°C, whereas the quenching ratio varies by 25%. The measurement conditions are the same as in **Figure 4.10**. Figure courtesy of P. Zhang and R. N. Ghosh.

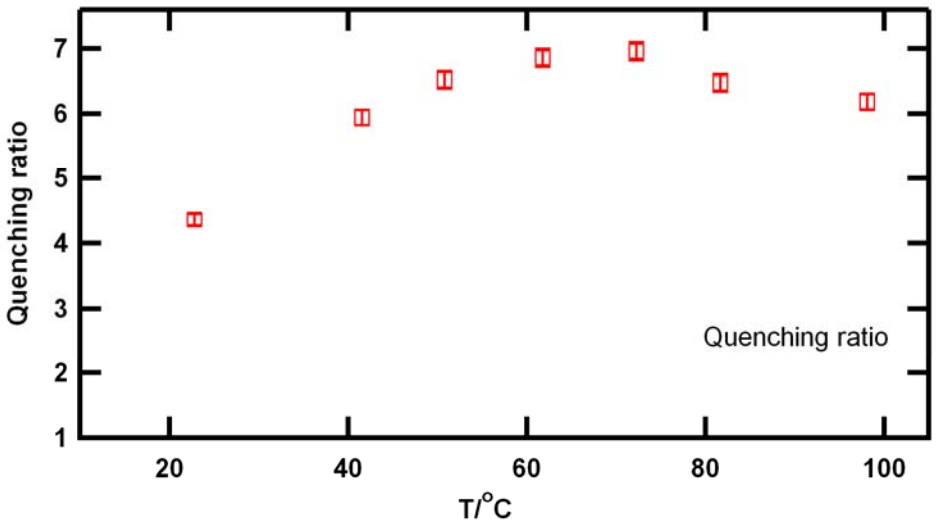

Figure 4.16. Quenching ratio (signal intensity in nitrogen vs. 21% oxygen) as a function of temperature for fiber **M**, from the data in **Figures 4.11 – 4.15**. These measurements show that in the temperature range of 50 to 100°C the quenching ratio is relatively independent of temperature, varying by ± 6%. Figure courtesy of P. Zhang and R. N. Ghosh.

4.3.2 Stern–Volmer relationship up to 100°C Fiber Sensors at Elevated Temperatures

The following sections demonstrate that the fiber sensors show promise, but do not obey the classic Stern–Volmer relationship up to 100°C. All the data are from fiber sensor **121**, see **Figure 4.17** for photographs of the as fabricated sensor and after all thermal testing. The sensor tip contains $K_2Mo_6Cl_{14}$•$1H_2O$ sol–gel particles embedded in an OtMOS/TEOS binder matrix. The sensing film was cured for 16 hours at 70°C. The tip contains roughly 8×10^{18} clusters/cm^3, after accounting for the volume contraction in forming the monolith and drying of the particle/binder composite.

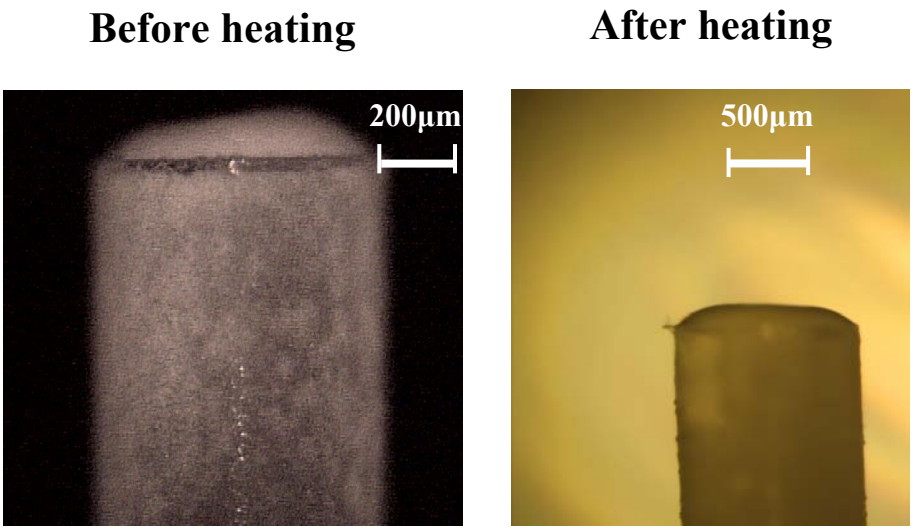

Figure 4.17. Photograph of fiber 121 as fabricated and after all thermal testing.

4.3.3 Fiber sensor 121 at 42°C

The oxygen response of fiber sensor **121** over several cycles from 2% (v/v) to 21% (v/v) O_2 at 42°C are shown in **Figure 4.18**. The device is easily able to detect changes in oxygen concentration at the percent level at this temperature. The data was taken in our flow-through system, with the sensor exposed to each gas concentration for about three minutes. The wait time in pure nitrogen was significantly longer to allow the device to equilibrate. The temperature stability of our system is quite good, over the 5.5 hours the temperature held at 41.9 ± 0.4°C.

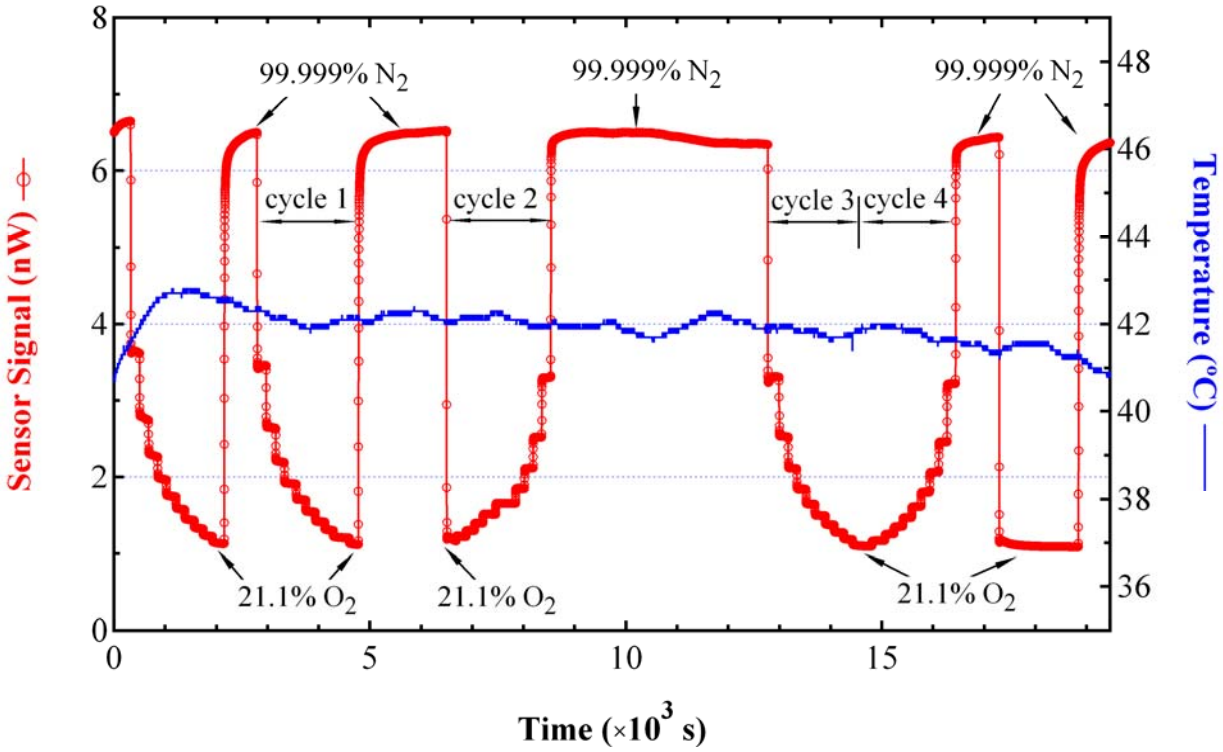

Figure 4.18. Oxygen sensitivity of fiber **121** at 42°C during several cycles of measurement. The gas composition for each cycle was: (a) <0.001, (b) 2.11, (c) 4.16, (d) 6.32, (e) 8.44, (f) 10.6, (g) 12.7, (h) 14.8, (i) 16.9, (j) 19.0, and (k) 21.1% oxygen, with the balance nitrogen. Note during the two cycles from 6,500–10,000 seconds and 14,580–17,062 seconds the gas order was reversed going from 21.1% oxygen to <0.001% oxygen. The coupled excitation power is 285 μW, the gas flow rate is 400 and 370 sccm at the input and output of the quartz chamber respectively, and the cluster concentration is ~8 × 10^{18} clusters/cm^3. Figure courtesy of P. Zhang and R. N. Ghosh.

The quenching of cluster emission by oxygen is a bimolecular dynamic (collisional) quenching process.[47] In homogeneous systems, the effect of quenching kinetics on emission intensity and lifetime are described by the classic Stern–Volmer relationship[44, 48]

$$I_0/I = 1 + K_{sv}[O_2]$$

$$K_{sv} = k_q \tau_0$$

Where I_0 and I are the emission intensities in the absence and presence of oxygen, K_{sv} is the Stern-Volmer constant, k_q is the quenching rate constant, and τ_0 is the emission lifetime in the absence of oxygen. Using a Stern-Volmer plot of I_0/I as a function of oxygen concentration allows one to examine the sensor sensitivity and create a linear calibration curve with a slope equal to K_{sv} for sensor. In heterogeneous systems where the emissive species is in multiple quenching microenvironments, the Stern-Volmer plot results in a non-linear plot with a downward curvature. Luminophores embedded in sol–gel matrices often give non-linear Stern-Volmer plots and the Demas two-site model[49-52] has proven to effectively describe the quenching kinetics in these cases. The two-site model is described by:

$$I_0/I = [f_1/(1 + K_{sv1}[O_2]) + f_2/(1 + K_{sv2}[O_2])]^{-1}$$

Where I_0 and I are the emission intensities in the absence and presence of oxygen, f_1 is the fractional contribution of the total emission from the luminophore located in microenvironment site 1 with Stern-Volmer constant K_{sv1}, and f_2 is the fractional contribution of the total emission from the lumiphore located at microenvironment site 2 with Stern-Volmer constant K_{sv2}. The following data for fiber sensor 121 are fit using the Demas two-site model.

The Stern-Volmer plot for fiber sensor 121 at 43°C is shown in **Figure 4.19**. Each measurement point in **Figure 4.19** is the average value of the normalized sensor signal from cycle 1-4 of **Figure 4.18**. The fit to the Stern–Volmer relationship using the two-site model is quite good and gives a curvilinear relationship between I_0/I and [O_2] with correlation of 0.99982. The values for f_1, f_2, K_{sv1}, and K_{sv2} are 0.68 ±0.03, 0.32 ±0.03, 4.08 ±0.48, and 0.26 ±0.02 respectively.

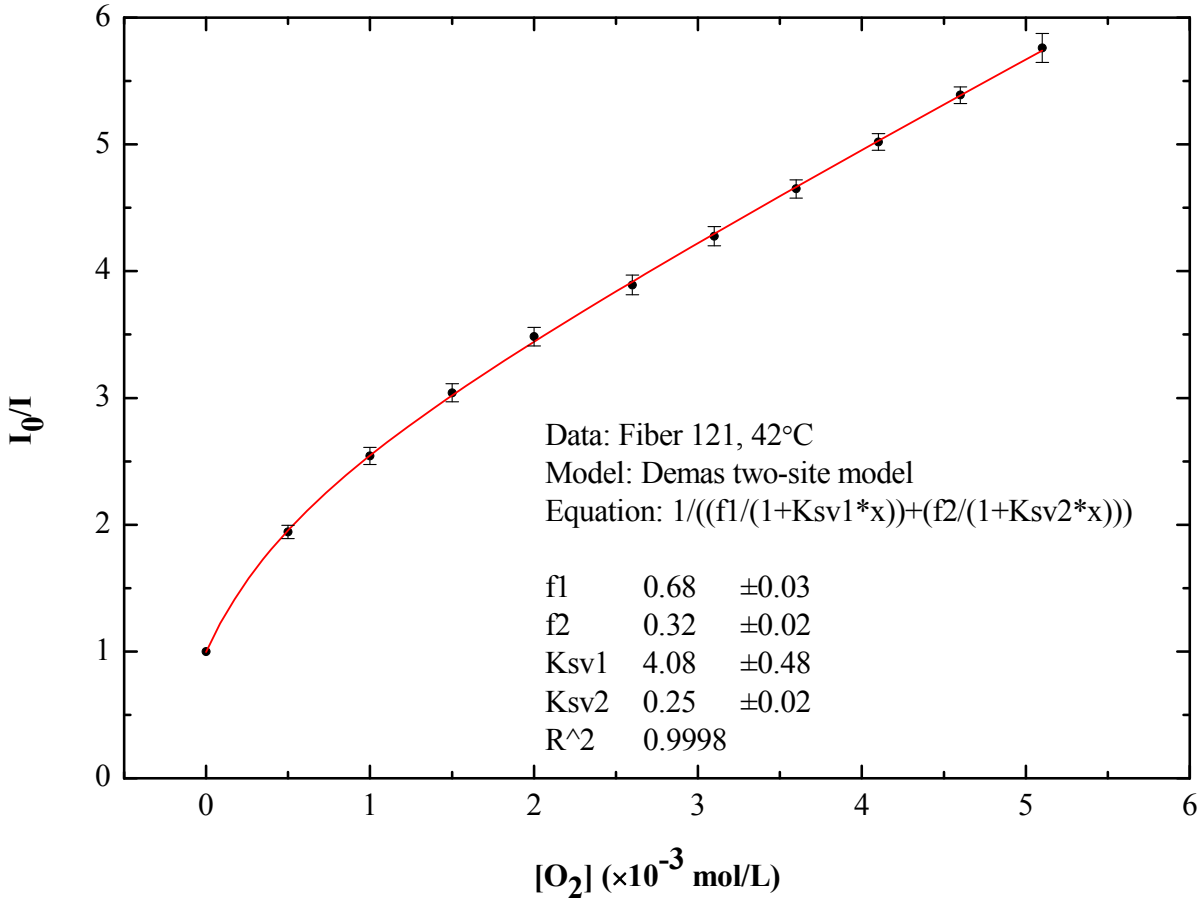

Figure 4.19. Stern–Volmer relationship, I_0/I as a function of molar oxygen concentration, at 42°C for fiber sensor **121**. The data represent the averages over the indicated four cycles in from **Figure 4.18**.

4.3.4 Fiber sensor 121 at 73°C

Shown in **Figure 4.20** is the oxygen response of the sensor at 73°C. The Stern–Volmer plot was obtained by averaging the measurements from four complete cycles between pure nitrogen and 21% (v/v) oxygen. The fit to the Stern–Volmer relationship using the two-site model is quite good and gives a curvilinear relationship between I_0/I and $[O_2]$ with correlation of 0.9998. The values for f_1, f_2, K_{sv1}, and K_{sv2} are 0.33 ±0.02, 0.67 ±0.02, 2.71 ±0.44, and 0.22 ±0.01 respectively.

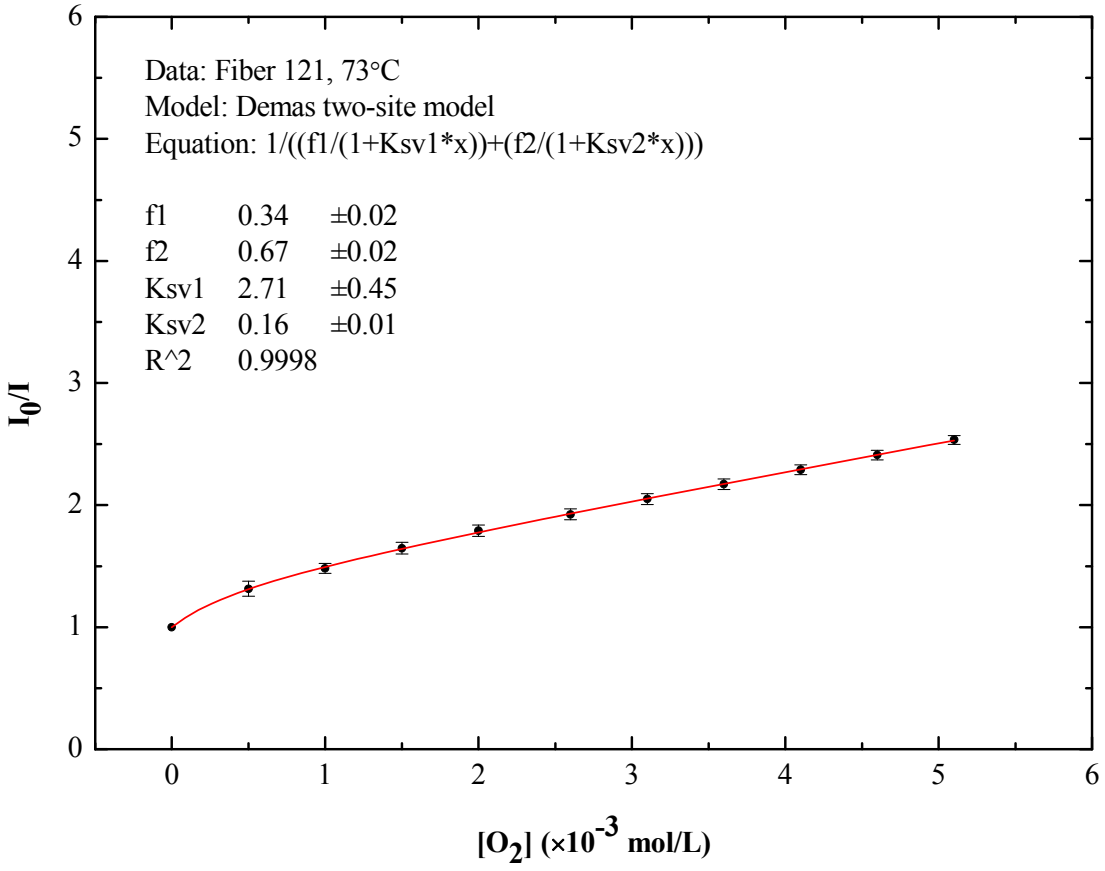

Figure 4.20. Stern–Volmer relationship, I_0/I as a function of molar O_2 concentration, at 73°C for fiber sensor **121**. Plotted is the average from four cycles of measurement. The measurement conditions are shown in **Figure 4.18**. The coupled excitation power is 285 μW, the gas flow rate is 400 and 390 sccm at the input and output of the quartz chamber respectively, and the cluster concentration is ~8×10^{18} clusters/cm^3.

4.3.5 Fiber sensor 121 at 102°C

Shown in **Figure 4.21** is the oxygen response of the sensor at 102°C. The Stern–Volmer plot was obtained by averaging the measurements from two complete cycles between pure nitrogen and 21% (v/v) oxygen. The fit to the Stern–Volmer relationship using the two-site model is quite good and gives a curvilinear relationship between I_0/I and $[O_2]$ with correlation of 0.9998. The values for f_1, f_2, K_{sv1}, and K_{sv2} are 0.25 ±0.02, 0.75 ±0.02, 1.09 ±0.15, and 0.08 ±0.01 respectively.

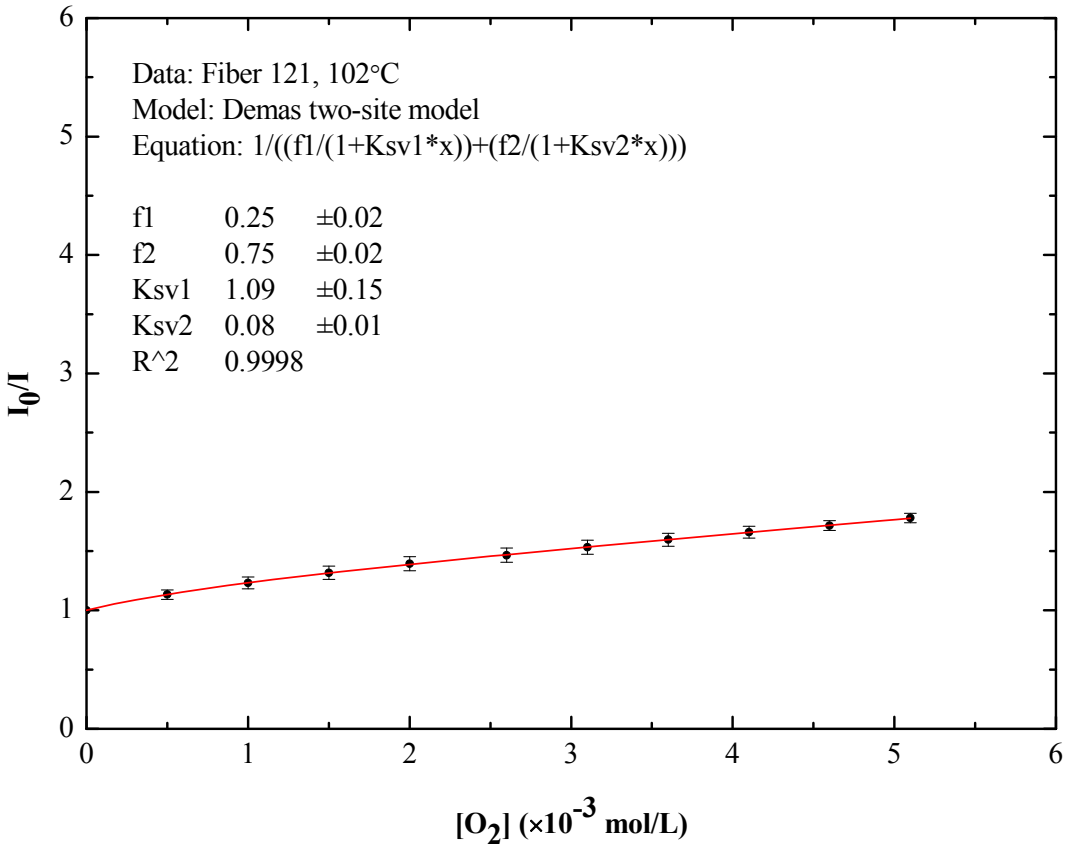

Figure 4.21. Stern–Volmer relationship, I_0/I as a function of molar O_2 concentration, at 102°C for fiber sensor **121**. Plotted is the average from two cycles of measurements. The coupled excitation power is 285 μW, the gas flow rate is 400 and 390 sccm at the input and output of the quartz chamber respectively, and the cluster concentration is ~8 × 10^{18} clusters/cm^3

The contribution of each microenvironment, $f_1/(1+K_{sv1}[O_2])$ and $f_2/(1+K_{sv2}[O_2])$, was calculated using an oxygen concentration of 1×10^{-3} and the values taken from **Figures 4.17 – 4.19**. The results are shown in **Table 4.2** and indicate that the clusters in microenvironment 2 are more accessible than the clusters in microenvironment 1 and make a larger contribution to the quenching ratio. The data also show a trend towards constant fractional contributions to the quenching after the sensor was heated. This is most likely related to the continued evolution of the sol–gel matrix and indicates the necessity of fully curing the sol–gel matrix prior to using sensors.

Table 4.2. Calculated fractional contributions of microenvironment sites 1 and 2 towards the quenching ratio at elevated temperatures for fiber sensor 121 based on the values from Figures 4.17, 4.18 and 4.19 and an oxygen concentration of 1×10^{-3}.

Sensor temperature	$f_1/(1+K_{sv1}[O_2])$	$f_2/(1+K_{sv2}[O_2])$
42°C	34%	66%
73°C	13%	87%
102°C	15%	85%

The Stern–Volmer constants provide a measure of the sensitivity of the fiber sensor towards detection of gaseous oxygen at 42°C, 73°C, and 102°C. Because the curves are non-linear, the sensitivity of the measurement is dependent on the analyte concentration and relative to the quenching site. These site-specific sensitivities are shown in **Table 4.3**. The data indicates that the sensitivity decreases with increasing temperature for both microenvironments and that the

contribution from site 2 is small. Despite the lower sensitivity, the data indicate that the sensor is able to operate up to 100°C.

Table 4.3. Fiber sensor 121 sensitivities for microenvironment sites 1 and 2 at elevated temperatures based on Stern-Volmer constants from Figures 4.17, 4.18 and 4.19.

Sensor temperature (°C)	**Site 1 Sensitivity based on K_{sv1} $[O_2]^{-1}$**	**Site 2 Sensitivity based on K_{sv2} $[O_2]^{-1}$**
42	4.08 ±0.48	0.25 ±0.02
73	2.71 ±0.45	0.16 ±0.01
102	1.09 ±0.15	0.08 ±0.01

4.3.6 Long-term performance and sensor repeatability

In this section we present the long-term performance of two fiber sensors at high temperatures, fiber sensor **45** at 58 °C and fiber sensor **70** at 71.5°C. Our goal was to determine the cycle-to-cycle stability of the oxygen measurements as well as the sensor performance over a period of many hours.

4.3.7 Fiber sensor 45 at 58°C

Fiber sensor **45** was selected for repeated nitrogen/oxygen cycling measurements and to monitor the sensor signal over a period of 24 days. This particular device was chosen due to the high initial sensor signal and the superior morphology and mechanical stability of the Mo-cluster/sol–gel compositing sensing film. The sensor tip contains $K_2Mo_6Cl_{14}$•$1H_2O$ sol–gel particles (**FJ-**

17 particles, 1–8 μm in size) embedded in an OtMOS/TEOS binder matrix. The solvent is ethanol and the fiber was hand dipped in the binder/particle solution binder, then cured for 16 hours at 70°C. The tip contains ~ 1.3×10^{18} clusters/cm^3. All the sensing measurements on fiber **45** (see **Figures 4.22 – 4.24)** were made using the first sensor characterization system prior to purchase of the commercial Horiba gas divider. A simple gas divider was constructed from a two-way switch and two flow meters, which can read from 100 to 1000 sccm, and the total gas flow was maintained at 1000 sccm. Pure nitrogen (<0.001% (v/v) O_2) was mixed with either 21.1% (v/v) or 1.0% (v/v) oxygen for gas concentrations between 2.1% (v/v) and 21.1% (v/v) oxygen or 0.1% (v/v) and 1.0 % (v/v) oxygen, respectively. Note that the residence time for the gas in the sensing chamber was not well defined in the "old" setup and was not a true flow-thorough geometry.

In **Figure 4.22** the quenching ratio (signal in nitrogen divided by the signal in oxygen) is plotted as a function of oxygen concentration from each of the six measurement cycles. The cycle-to-cycle variations over the 1 hour measurement period are used to gauge the repeatability of measurements. It was found that at 21.1% (v/v) oxygen there is a ±1% variation in the concentration, whereas at 2.1% (v/v) oxygen there is a ±15% variation in the concentration based on the intensity change. The larger variation in the measurements at low concentration is due primarily to the accuracy with which we can set the flow meter.

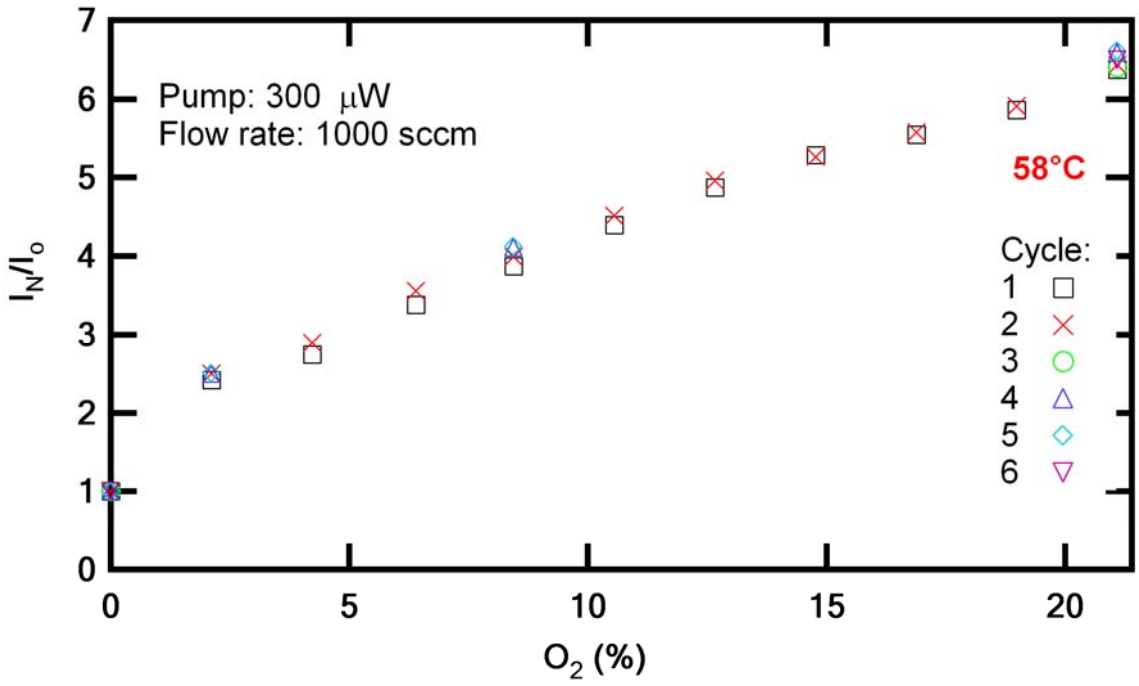

Figure 4.22. Quenching ratio (intensity in nitrogen/intensity in oxygen) for 6 nitrogen/oxygen cycles at 58°C for fiber sensor **45**. The cycle-to-cycle variations correspond to a ±1 – ± 15% uncertainty in oxygen concentration over the entire measurement range from 21.1 to 2.1% oxygen respectively. The luminescent tip contains $K_2Mo_6Cl_{14}$•$1H_2O$ sol–gel particles embedded in an OtMOS/TEOS binder matrix, with 1.3×10^{18} clusters/cm^3 (fiber **45**). The coupled excitation power is 300 nW at 365 nm and the gas flow rate is 1000 sccm. These measurements were made with the "homemade" gas switching system. Figure courtesy of P. Zhang and R. N. Ghosh.

The repeatability of the results at 58°C are encouraging, the slow upward drift in the nitrogen from the first to the sixth cycle is puzzling. This is a phenomenon that was observed during the first few days of measurement in a number of sensors. An increase in signal under nitrogen suggests that the heated dry gas flowing over the Mo-cluster/sol–gel composite removes an *in situ* quencher, possibly related to the solvent or byproducts of the sol–gel reaction. One possibility is “drying” or continuing to remove solvent from the sol–gel binder matrix. We are

investigating whether curing the sensors in vacuum at 70°C immediately after coating will improve performance.

The sensitivity of fiber **45** at low oxygen concentration from 0.1 to 1.0% (v/v) oxygen in steps of 0.1% (v/v) at 60°C presented in **Figure 4.23** shows that the sensor can clearly resolve the 0.1% (v/v) changes in absolute oxygen concentration at high temperature. The quenching ratio at 1% (v/v) oxygen is about 1.65, consistent with the data in **Figure 4.22**.

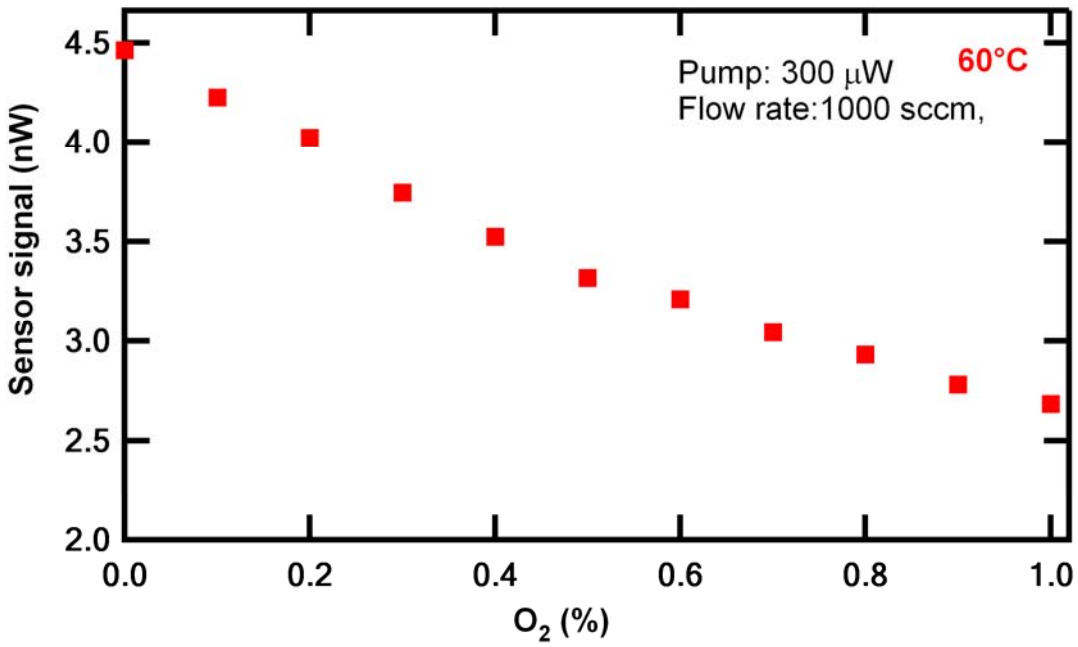

Figure 4.23. Sensor output signal from fiber **45** at 60°C as a function of oxygen concentration: 0.1, 0.2, 0.3, 0.4, 0.5, 0.6, 0.7, 0.8, 0.9, and 1% oxygen (balance is nitrogen). It shows that the sensor can resolve a 0.1% change in absolute oxygen concentration in the 0.1–1% range at 60°C. Figure courtesy of P. Zhang and R. N. Ghosh.

In order to assess the stability of fiber sensor **45** over time, the performance was tracked over a 23-day period as shown in **Figures 4.24** and **4.25**.

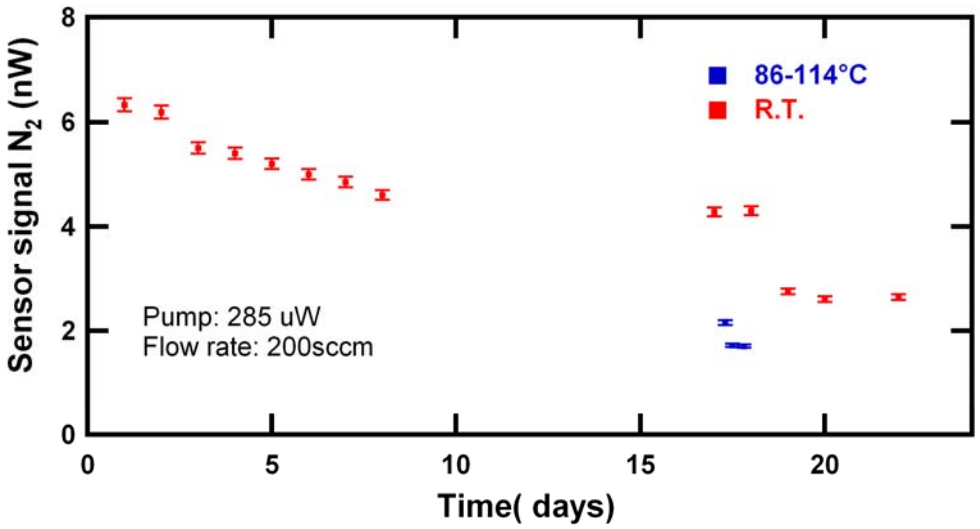

Figure 4.24. Signal from fiber **45** measured over a period of 23 days at (■) room temperature and (■) 83 and 114°C (the lower measurement is 144°C). The measurement sequence began (day 0) 3 days after the sensor was fabricated. On day 17, the sensor was measured at room temperature, 83, and 114°C, and then left at 90°C for 20.5 hours with the LED blocked. As the sensor signal at room temperature on day 18 is the same as day 17, we conclude that high-temperature excursions are not intrinsically harmful to the device. See text for explanation of the drop in signal on day 19. Note that the total UV exposure over the entire 23 days is about 22.5 hours. Figure courtesy of P. Zhang, R. Loloee, and R. N. Ghosh.

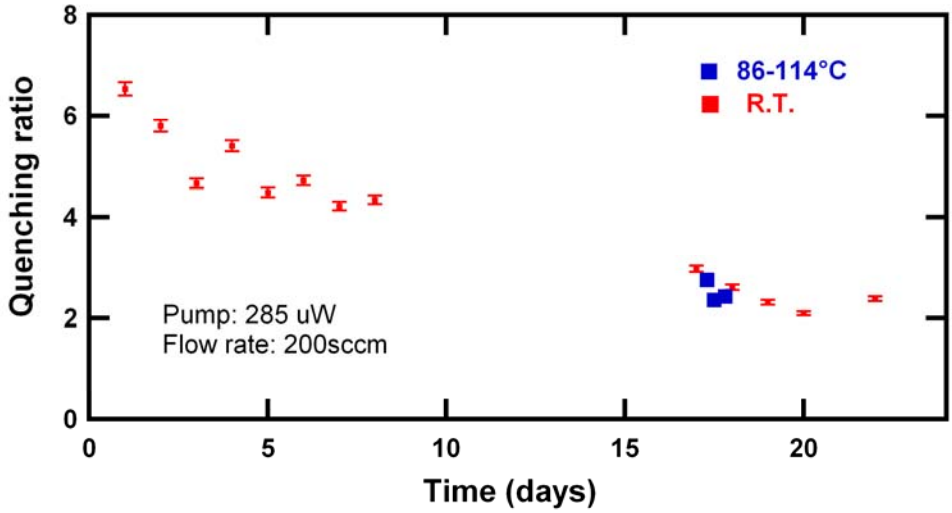

Figure 4.25. Quenching ratio (signal intensity in nitrogen/signal intensity in 21% oxygen) for the measurement sequence described in **Figure 4.22.** The data demonstrates that after about 17 days and high-temperature cycling the sensor response stabilizes. Figure courtesy of P. Zhang, R. Loloee, and R. N. Ghosh.

Day 0 of these measurement sequences began three days after sensor fabrication. The signal in nitrogen decreased slowly over the first eight days, while the quenching ratio levels off after day 5. No measurements were made from day 10 to day 16, during which time the sensor was stored in laboratory air. On day 17 the sensor was measured at room temperature, 86°C, 110°C, then held at 90°C for 20.5 hours without UV exposure in lab air. The 90°C exposure was used to show that high temperature by itself is not harmful to the sensor. On day 18, the room temperature measurement was repeated and the signal in nitrogen (4.3 nW) was the same before and after heating while the quenching ratio drops by 10%. The quenching ratio, which is the measurement that will be used for sensing, stabilizes after about 17 days and high-temperature cycling. On day 19 the signal in nitrogen drops to 2.5 nW and does not recover. Sudden loss of signal implies a catastrophic loss of clusters which cannot be easily explained by a chemical process. A mechanical failure such as delamination and loss of the sensing layer at the tip of the fiber is more plausible, but micrographs of the sensor tip taken at day 0 and day 25, see **Figure 4.26**, show no signs of delamination of the Mo-cluster/sol–gel. A possible explanation for this is that the composite delaminates from the flat surface at the tip of the fiber, but adhesion of the composite to the lateral surface of the fiber remains intact. This "internal" delamination of the composite likely affects the coupling of UV photons into the composite and the visible signal back to the detector. A better understanding of the drying process as a function of time, temperature and atmospheric pressure may provide insight into delamination, as well as conditions that result in more rapid stabilization of quenching ratios.

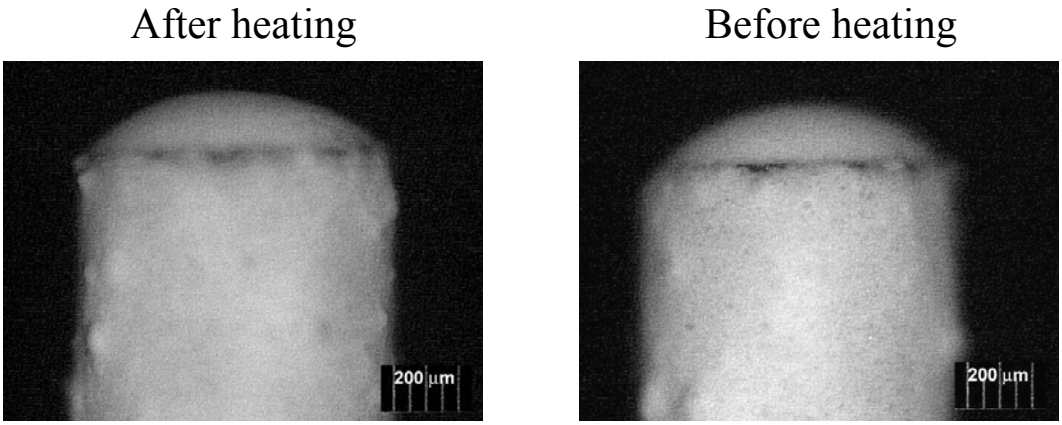

Figure 4.26. The side view of fiber **45** before (day 0) and after 23 days of room temperature measurements as well heating at high temperature up to 114°C. There are no external signs of delamination and the morphology of the Mo-cluster/sol–gel film does not change.

4.3.8 Fiber sensor 70 at 71.5°C

Following successful high-temperature sensor measurements on fiber sensor **45**, the reproducibility of the sensor fabrication technique was tested by fabricating and testing a "clone" of fiber sensor **45**. The difference in the fabrication is that fiber sensor **70** was cured for 30 minutes longer than fiber senor **45**.

Sensor measurements at 70°C for 13.8 hours of cycling between nitrogen (<0.001% (v/v) oxygen) and 21.1% (v/v) oxygen are given in **Figure 4.27**. These measurements were made using an electronic gas switching system. The sensor was 19 days old at the start of the measurements. Since we know that the input and output gas flows are the same to better than 5%, we can estimate that the gas exchange time is 10 s for a 200-sccm flow. The temperature

stability of the system is 71.5 ± 1°C. Note that the 0.4°C "jitter" in the temperature data is most likely due to digitization errors in the D/A board and could be improved upon by adjusting the voltage input range of the board. Prior to making sensing measurements we determined that the "unwanted" signal from a fiber device without any Mo-clusters, *i.e.* a fiber with sol-particles in the same binder matrix, was 0.01 nW. This is a factor of 70 larger than our lowest signal in oxygen.

The data in **Figure 4.27** are remarkably stable over time. The variation of the sensor signal in nitrogen is synchronous with the temperature fluctuations. Additionally, there is a slow drift over the 13.8 hours of measurement from 3.1 to 2.9 nW, which is not related to a drift in the optical coupling. As in the case of fiber sensor **45** this most likely reflects *in situ* curing of the sol–gel binder. The oxygen intensity decreases linearly with time from 0.8 to 0.7 nW and seems to be uncorrelated with the temperature variations. The quenching ratio varies from 3.9 to 4.1 over the measurement period. The performance of fiber **45** and fiber **70** are similar, with nitrogen signal intensities in the 3 to 4 nW range and quenching ratios between pure nitrogen and 21.1% (v/v) oxygen of 2.7 at 86°C and 3.9 and 70°C. Again, the variations between the two sensors are most likely due to evolution of the sol–gel binder with time, gas flow and temperature. These are very exciting results as they demonstrate the feasibility of using Mo-clusters to monitor oxygen at temperature in the 60 to 70°C range for a period of many hours.

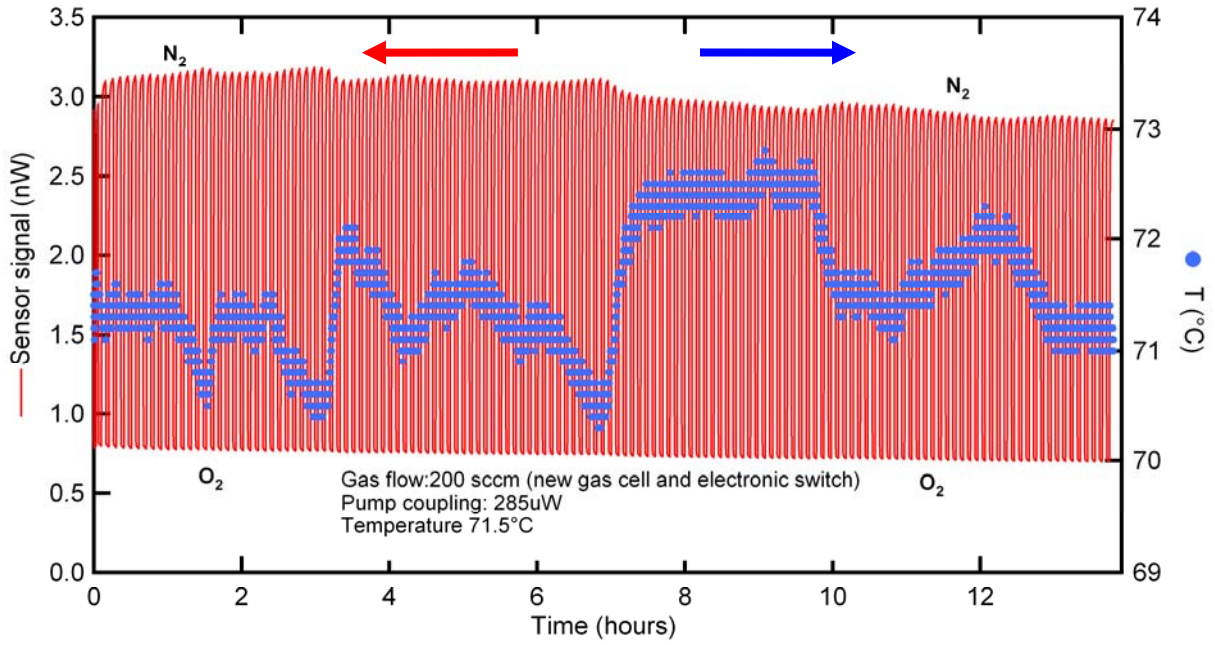

Figure 4.27. High-temperature measurements of fiber sensor **70** during 13.8 hours of cycling between nitrogen (<0.001% oxygen) and 21.1% oxygen at 70°C. These measurements were made in a quartz gas sensor cell, with temperature stability of ± 1°C for 13.8 hours. In this flow-through cell the gas exchange time is 10 s for a 200-sccm flow. The gas cycling is controlled by a solenoid switch, with 3.6 min in nitrogen and 2.3 minutes in oxygen. The variations in the envelope of the sensor signal are synchronous with the temperature fluctuation. The data demonstrates that we can achieve a quenching ratio of 4 ± 0.1 between nitrogen (<0.001% oxygen) and 21% oxygen over 13.8 hours at 71.5 ± 1°C. Figure courtesy of P. Zhang, R. Loloee, and R. N. Ghosh.

4.4 CONCLUSIONS

A fiber optic technique for detection of gas phase oxygen up to 100°C based on the $^3O_2$ quenching of the luminescence from molybdenum chloride clusters, $K_2Mo_6Cl_{14}•1H_2O$, has been achieved. The inorganic sensing film is a composite of sol–gel particles embedded in a thin,

oxygen permeable sol–gel binder. The particles are comprised of thermally stable, luminescent $K_2Mo_6Cl_{14}•1H_2O$ clusters dispersed in a fully equilibrated sol–gel matrix. From 40 to 100°C, the fiber sensor switches ~6× in intensity in response to alternating pulses of <0.001% (v/v) and 21% (v/v) oxygen between two well defined levels with a response time of 10 seconds. The sensor signal is a few nW for an input excitation power of 250 μW. The normalized sensor signal is non-linear with molar oxygen concentration and fits reasonably to the theoretical two-site Stern–Volmer relationship. Although the sensitivity decreases with temperature, sensitivity at 100°C is 160 $[O_2]^{-1}$. These parameters are well suited for *in situ*, real-time monitoring of oxygen for industrial process control applications.

A compact high-temperature fiber sensor test setup to characterize devices up to 350°C in a gas flow through system was designed and built. The setup is designed to be portable for field testing and uses an inexpensive, ~$6.00 ultraviolet (UV) light emitting diode (LED) as the excitation source. An automated data acquisition system has been developed to simultaneously record the sensor luminescence signal and sensor temperature, to ±1°C. The sensor response time can be determined to better than 10 s, as the gas exchange time in the chamber is <6 s for a 1.5 L/min flow.

The salient features of our home-built sensor characterization system are as follows. (1) The coupled excitation power into the fiber sensor from the UV light source is 300 nW–500 nW. (2) Since visible output from the UV LED in the emission bandwidth of the Mo-clusters, 600 nm–800 nm, is spectroscopically indistinguishable from the real sensor signal, it set a bound on the

smallest signal we can detect. The rejection of unwanted excitation power in the 600 nm–800 nm emission bandwidth is 10^{-5}, 0.625% of the lowest sensor signal associated with oxygen. (3) The working end of the fiber sensor is enclosed in a heated quartz chamber that allows for true flow measurements with a measured gas exchange time of ~10 seconds. (4) The gas exchange is performed either using a solenoid switch to switch back and forth between two levels or with a precision manual gas divider which allows us to mix two gases in the ratio of 1:10, 2:10… 10:10.

The optical properties of a large number of fiber sensors were tested up to 100 °C. The best results were obtained using $K_2Mo_6Cl_{14}$•$1H_2O$/sol–gel composite sensing film. Fiber **M** demonstrated quenching of 4–6× between <0.001% and 21.1% (v/v) oxygen at 23, 41, 60, 81 and 100°C respectively. The sensor switches abruptly, with a time constant of less than 10 s, between two well defined levels. From theory the quenching of the cluster luminescence by oxygen is expected to obey a Stern–Volmer relationship based on a two-site model, which was verified by measurements of fiber **121** at 41, 73, and 102°C. The cycle-cycle variations for six cycles between nitrogen and oxygen at 58°C for fiber **45** corresponds to an uncertainty of ±1% to ±15% in oxygen concentration over the entire measurement range from 21.1% (v/v) to 2.1% (v/v) oxygen respectively. The long-term performance of our devices was determined by cycling fiber **70** between <0.001% (v/v) and 21.1% (v/v) oxygen for 14 hours. The data were stable over the entire period, the variations in sensor signal were found to be synchronous with the temperature fluctuations in the flow through cell.

The magnitude of the sensor signal is very encouraging in terms of practical implementations of our device up to at least 100°C. A ~3-nW output signal is obtained for ~300 μW of incident excitation power; 1×10^{-5} is a very reasonable power conversion efficiency for a fiber sensor. Autofluorescence or the magnitude of the signal in our measurement bandwidth due to fluorescence from a length of fiber without any cluster on the tip sets a lower bound on the smallest signal we can detect from our sensor. For the current 15-cm long fiber sensor, the autofluorescence (0.011 nW) is 40× smaller than the signal (~ 0.4 nW) in 20% (v/v) oxygen.

REFERENCES

REFERENCES

[1] S. M. Grist, L. Chrostowski, K. C. Cheung, *Sensors* **2010**, *10*, 9286.

[2] O. N. Ponomareva, V. A. Arlyapov, V. A. Alferov, A. N. Reshetilov, *Applied Biochemistry and Microbiology* **2011**, *47*, 1.

[3] T. H. Tran-Thi, R. Dagnelie, S. Crunairez, L. Nicole, *Chemical Society Reviews* **2011**, *40*, 621.

[4] M. J. P. Leiner, *Analytica Chimica Acta* **1991**, *255*, 209.

[5] O. S. Wolfbeis, *Sensors and Actuators B-Chemical* **1991**, *5*, 1.

[6] D. Avnir, S. Braun, M. Ottolenghi, *ACS Symposium Series* **1992**, *499*, 384.

[7] P. N. Prasad, F. V. Bright, U. Narang, R. Wang, R. A. Dunbar, J. D. Jordan, R. Gvishi, in *Hybrid Organic-Inorganic Composites, Vol. 585*, **1995**, 317.

[8] R. Gvishi, U. Narang, G. Ruland, D. N. Kumar, P. N. Prasad, *Applied Organometallic Chemistry* **1997**, *11*, 107.

[9] R. A. Potyrailo, S. E. Hobbs, G. M. Hieftje, *Fresenius Journal of Analytical Chemistry* **1998**, *362*, 349.

[10] G. Vishnoi, M. Morisawa, S. Muto, *Optical Review* **1998**, *5*, 13.

[11] Y. Kostov, G. Rao, *Review of Scientific Instruments* **2000**, *71*, 4361.

[12] C. Sanchez, B. Lebeau, *MRS Bulletin* **2001**, *26*, 377.

[13] N. Docquier, S. Candel, *Progress in Energy and Combustion Science* **2002**, *28*, 107.

[14] M. D. Marazuela, M. C. Moreno-Bondi, *Analytical and Bioanalytical Chemistry* **2002**, *372*, 664.

[15] Y. Amao, *Microchimica Acta* **2003**, *143*, 1.

[16] C. Sanchez, B. Lebeau, F. Chaput, J. P. Boilot, *Advanced Materials* **2003**, *15*, 1969.

[17] C. P. Bacon, Y. Mattley, R. DeFrece, *Review of Scientific Instruments* **2004**, *75*, 1.

[18] O. S. Wolfbeis, *Analytical Chemistry* **2004**, *76*, 3269.

[19] A. Mills, *Chemical Society Reviews* **2005**, *34*, 1003.

[20] M. Ando, *Trac-Trends in Analytical Chemistry* **2006**, *25*, 937.

[21] P. C. A. Jeronimo, A. N. Araujo, M. Montenegro, *Talanta* **2007**, *72*, 13.

[22] G. Orellana, D. Haigh, *Current Analytical Chemistry* **2008**, *4*, 273.

[23] R. Ciriminna, M. Pagliaro, *Analyst* **2009**, *134*, 1531.

[24] M. Quaranta, S. M. Borisov, I. Klimant, *Bioanalytical Reviews* **2012**, *4*, 115.

[25] J. Hodgkinson, R. P. Tatam, *Measurement Science & Technology* **2013**, *24*.

[26] X. D. Wang, O. S. Wolfbeis, *Analytical Chemistry* **2013**, *85*, 487.

[27] J. N. Demas, B. A. Degraff, *Analytical Chemistry* **1991**, *63*, A829.

[28] J. N. Demas, B. A. Degraff, *Sensors and Actuators B-Chemical* **1993**, *11*, 35.

[29] J. N. Demas, B. A. DeGraff, *Coordination Chemistry Reviews* **2001**, *211*, 317.

[30] J. N. Demas, B. A. DeGraff, P. B. Coleman, *Analytical Chemistry* **1999**, *71*, 793A.

[31] J. N. Demas, E. W. Harris, C. M. Flynn, D. Diemente, *Journal of the American Chemical Society* **1975**, *97*, 3838.

[32] M. C. DeRosa, D. J. Hodgson, G. D. Enright, B. Dawson, C. E. B. Evans, R. J. Crutchley, *Journal of the American Chemical Society* **2004**, *126*, 10493.

[33] O. S. Wolfbeis, *Analytical Chemistry* **2002**, *74*, 2663.

[34] O. S. Wolfbels, *Analytical Chemistry* **2008**, *80*, 4269.

[35] D. B. Papkovsky, G. V. Ponomarev, W. Trettnak, P. Oleary, *Analytical Chemistry* **1995**, *67*, 4112.

[36] D. B. Papkovsky, K. S. a. G. L. S. Chandan, in *Methods in Enzymology, Vol. Volume 381*, Academic Press, **2004**, 715.

[37] C. O'Donovan, J. Hynes, D. Yashunski, D. B. Papkovsky, *Journal of Materials Chemistry* **2005**, *15*, 2946.

[38] R. I. Dmitriev, D. B. Papkovsky, *Cellular and Molecular Life Sciences* **2012**, *69*, 2025.

[39] B. D. MacCraith, C. McDonagh, *Journal of Fluorescence* **2002**, *12*, 333.

[40] C. M. McDonagh, A. M. Shields, A. K. McEvoy, B. D. Maccraith, J. F. Gouin, *Journal of Sol-Gel Science and Technology* **1998**, *13*, 207.

[41] B. D. MacCraith, C. McDonagh, A. K. McEvoy, T. Butler, G. Okeeffe, V. Murphy, *Journal of Sol-Gel Science and Technology* **1997**, *8*, 1053.

[42] E. J. Park, K. R. Reid, W. Tang, R. T. Kennedy, R. Kopelman, *Journal of Materials Chemistry* **2005**, *15*, 2913.

[43] Nichia Corporation, *NSHU5x0B (Rank3) Spectrum, STS-KSE5582_NHU5x0B Technical Information Sheet* **2005**.

[44] R. N. Ghosh, G. L. Baker, C. Ruud, D. G. Nocera, *Applied Physics Letters* **1999**, *75*, 2885.

[45] V. S. Khotimsky, M. V. Tchirkova, E. G. Litvinova, A. I. Rebrov, G. N. Bondarenko, *Journal of Polymer Science Part a-Polymer Chemistry* **2003**, *41*, 2133.

[46] A. O. Malakhov, V. G. Berezkin, E. Y. Sorokina, A. V. Volkov, V. V. Volkov, *Polymer Science Series B* **2004**, *46*, 23.

[47] J. R. Lakowicz, *Principles of Fluorescence Spectroscopy*, 3rd ed., Springer, New York, **2006**.

[48] J. A. Jackson, M. D. Newsham, C. Worsham, D. G. Nocera, *Chemistry of Materials* **1996**, *8*, 558.

[49] G. A. Baker, B. R. Wenner, A. N. Watkins, F. V. Bright, *Journal of Sol-Gel Science and Technology* **2000**, *17*, 71.

[50] E. R. Carraway, J. N. Demas, B. A. Degraff, *Analytical Chemistry* **1991**, *63*, 332.

[51] E. R. Carraway, J. N. Demas, B. A. Degraff, J. R. Bacon, *Analytical Chemistry* **1991**, *63*, 337.

[52] J. N. Demas, B. A. DeGraff, W. Xu, *Analytical Chemistry* **1995**, *67*, 1377.

Chapter 5 – Final remarks and future work

The objective of the project was to fabricate a luminescent-based fiber optic oxygen sensor for use at combustion temperatures. Based on measurements using cluster/sol–gel films, the sensor shows promise for oxygen measurements up to 200°C – far below combustion temperatures. Several sensors were fabricated and used to measure oxygen levels between 23°C and 114°C. This is roughly 50°C higher than current luminescent-based optical fiber oxygen sensing technology. Although the sensors are exciting, many of the results require further study in order to explain, many new questions arose, and several ideas for future applications came to light.

In chapter 2, we investigated the thermal-, chemical-, and photo- stability of several molybdenum clusters. It was determined that the potassium salt of the molybdenum cluster, $K_2Mo_6Cl_{14}•1H_2O$ has the requisite stability and could be incorporated into a sol–gel matrix without compromising the photophysics relevant to O_2 sensing. There were several unresolved questions, however. First, what was the precipitate formed when solutions in methanol and ethanol were made? Second, why does the absorption spectrum of the cluster in acetonitrile show an increase in absorbance at ~300 nm over time? Is it due to nanoparticulates that are not removed during the filtration of the clusters during purification or an impurity in the solvent that reacts with the clusters? Investigation of this issue using anhydrous $K_2Mo_6Cl_{14}$ in anhydrous acetonitrile points to water as the culprit and a paper detailing the results of that research is currently in preparation. Another question that remains is whether or not other alkali metal salts

are as stable or more so, for high temperature applications. It would be interesting to study selected other salts in several sol–gel matrices and compare the quenching mechanisms of each.

In chapter 3, the cluster was incorporated successfully into a sol–gel matrix. The parameters for preparing films with good adhesion were studied and dip coating fibers in a particle/sol–gel binder gave the best results. The particles were prepared by pulverizing fully cured sol–gel monoliths that contained the $K_2Mo_6Cl_{14}•H_2O$ cluster using a small ball mill. This allowed us to prepare sensors by dip coating fibers, and subsequently test their properties, but tended to be a cumbersome method of producing consistent, high quality films. One of the initial goals aimed toward commercialization of the sensor was the use of spray coating rather than dip coating to fabricate the sensor. While the particle in binder approach solved the delamination issues initially encountered, it was not amenable for use in a spray coating scheme. For spray coating, a uniform moderately viscous solution with ample cluster concentration is required, the matrix needs to contain enough void space to allow fast oxygen diffusion, and the contraction of the sol–gel must be minimal so that the shear forces do not overcome the force of adhesion. By further refining the sol–gel matrix precursor(s), reaction conditions, and processing parameters it would be possible to use the spray coating method of preparing fiber sensors.

Other possible advancements to the matrix might come from the use of a fluorinated sol–gel system, embedding the cluster in an aerogel, or a fluorinated aerogel. A fluorinated sol–gel matrix opens up the possibility for applications such as dissolved oxygen sensing and Bright et al have used a fluorinated sol–gel to achieve quenching ratios (I_0/I) of 35 with linear Stern–Volmer plots.[1]

An aerogel matrix may substantially improve the temperature range, sensor response time, and the linearity of the Stern–Volmer plot for the sensor. It has been shown that a dye molecule can be incorporated into an aerogel[2] and photoluminescent aerogels for oxygen sensing have been prepared.[3-7] The ability of an aerogel to serve as a thermal barrier[8] might extend the high temperature survivability of the molybdenum cluster while measuring oxygen and extend the range of temperatures over which the cluster photophysics remains useful. Although aerogels have very good insulating properties they lack the mechanical strength[8-10] of our sol-gel matrix. The lack of mechanical strength of the aerogel can be addressed using a protective housing[3] that does not interfere with the flow oxygen or by improving the mechanical strength thorough the incorporation of a xerogel.[9-12]

In chapter 4, the properties of several fiber-based oxygen sensors were tested and the results showed promise. The results also lead to many questions and ideas for future applications. The first question is the non-linearity of the Stern–Volmer plots. Second, why does the regressed line not cross one when the $[O_2]$ is zero. From the data it appears that the local environment affects the quenching mechanism – deviating from the simple bimolecular quenching mechanism. Using lifetime experiments, the nature of the local environment can be explored to determine how to model the system in such a way as to predict the concentration dependence accurately.

There are several improvements that could be made to the system used to collect data from the sensor. These improvements include decreasing the uncertainty of temperature measurements from $\pm 1^{\circ}C$, improving the ability to determine sensor response times to less than 10 seconds, and removal of the signal obtained from our fiber sensor system when the LED is turned on. It would also be useful to determine the time required to fully exchange gases in the cuvette and to exchange gases in the matrix. There are also useful several pieces of data that should be obtained such as intensity and quenching measurements over a period of months up to a year and evaluation of the sensor at temperatures up to $200^{\circ}C$.

As mentioned previously, the temperature range of the current sensor is not ideal for direct analysis of $[O_2]$ during combustion in power plants, but it does provide opportunities for use in other areas such as dissolved oxygen sensing in aquaculture. The sensor matrix has already been modified to monitor $[O_2]$ in water for use in aquaculture and shows promising results. Another potential application that I find very interesting involves coating a surface with an oxygen-sensitive luminescent film called a pressure sensitive paint, measuring the pressure at various points on the surface, and then mapping it out to determine the aerodynamics of a structure. Many of the current pressure sensitive paints suffer from temperature limitations or weak emission intensities. The emission intensity and increased temperature range of the molybdenum cluster/sol–gel composites should broaden the range of pressure sensitive paint applications.

REFERENCES

REFERENCES

[1] R. M. Bukowski, R. Ciriminna, M. Pagliaro, F. V. Bright, *Analytical Chemistry* **2005**, *77*, 2670.

[2] D. I. Santos, M. A. Aegerter, C. H. Brito Cruz, M. Scarparo, J. Zarzycki, *Journal of Non-Crystalline Solids* **1986**, *82*, 165.

[3] M. R. Ayers, A. J. Hunt, in *USPTO Patent Full-Text and Image Database* (Ed.: U. P. a. T. Office), The Reagents of the University of California, United States, **1999**, 14.

[4] S. P. Watton, C. M. Taylor, G. M. Kloster, S. C. Bowman, in *Progress in Inorganic Chemistry, Vol 51, Vol. 51*, **2003**, 333.

[5] N. Leventis, A. M. M. Rawashdeh, I. A. Elder, J. H. Yang, A. Dass, C. Sotiriou-Leventis, *Chemistry of Materials* **2004**, *16*, 1493.

[6] D. L. Plata, Y. J. Briones, R. L. Wolfe, M. K. Carroll, S. D. Bakrania, S. G. Mandel, A. M. Anderson, *Journal of Non-Crystalline Solids* **2004**, *350*, 326.

[7] N. Leventis, I. A. Elder, D. R. Rolison, M. L. Anderson, C. I. Merzbacher, *Chemistry of Materials* **1999**, *11*, 2837.

[8] K. E. Parmenter, F. Milstein, *Journal of Non-Crystalline Solids* **1998**, *223*, 179.

[9] M.-A. Einarsrud, E. Nilsen, *Journal of Non-Crystalline Solids* **1998**, *226*, 122.

[10] N. Leventis, C. Sotiriou-Leventis, G. H. Zhang, A. M. M. Rawashdeh, *Nano Letters* **2002**, *2*, 957.

[11] D. M. Smith, D. Stein, J. M. Anderson, W. Ackerman, *Journal of Non-Crystalline Solids* **1995**, *186*, 104.

[12] C. Alie, R. Pirard, A. J. Lecloux, J.-P. Pirard, *Journal of Non-Crystalline Solids* **1999**, *246*, 216.